

# Design and Implementation of High Performance BPSK Demodulator for Satellite Communications

By

Ehsan Tofigh

February 26, 2016

In partial fulfilment of the requirements for the degree of

**Master of Science**

in Aerospace Engineering

at Delft University of Technology

Supervisor: Ir. J. Bouwmeester, TU Delft  
Thesis Committee: Ir. B. T. C. Zandbergen, TU Delft  
Dr. Ir. S. Speretta, TU Delft  
Dr. Ir. E. J. O. Schrama, TU Delft





## Abstract

The Delfi program is a development line of small satellites comprising the successful Delfi-C3 and Delfi-n3Xt CubeSat missions. As part of an effort to involve radio amateurs from all over the world, a telemetry client is designed which allows radio amateurs to demodulate, decode and display telemetry data. This software was designed for an RF front-end connected to a sound card acting as low-end baseband sampling device. It has been discovered that there was a significant gap of 5 dB between the required Signal-to-Noise Ratio (SNR) for the software demodulator and the theoretical required link margin. This thesis presents an approach which decreases this gap while upgrading the demodulator for future use, taking advantage of emerging capabilities of Software Defined Radio (SDR) technology.

Today, SDRs have reached a high level of maturity and are slowly emerging in everyday communication systems. However, little information is available in literature on the real-world performance of SDRs for satellite communications. Furthermore, while many researchers have produced working software-defined demodulators, very little effort is spent on maximizing their performance. This gap in knowledge presents an opportunity to deliver significant contributions to the growing field of SDR communications, while simultaneously realizing the more practical goal of producing an improved telemetry client for the upcoming Delfi missions.

In this thesis, an architectural overview and analysis of a high performance software-defined implementation of Binary Phase Shift Keying (BPSK) demodulator is presented. Particular attention is given to improving the Bit-Error Rate (BER) and initial signal acquisition performance when computational time is abundant. The key to achieving this goal is identifying and tuning the critical factors that affect the performance of a BPSK demodulator. To accomplish this task in a systematic way, a link was established between the orbital parameters of the mission and the tuning parameters of the demodulator. The proposed demodulator consists of a Costas loop for carrier recovery and Gardner's algorithm for clock recovery.

The demodulator performance was measured for simulated Additive White Gaussian Noise (AWGN) channels in MATLAB and validated experimentally using real satellite transmissions from the Delfi-n3Xt mission. The measured BER for data rates from 2.4 to 9.6 kbps is compared to the theoretical limit. It is shown that the new software demodulator lowers the required SNR by 5 dB as compared to the previously implemented telemetry client and is less than 1 dB from the theoretical limit. Furthermore, consistent signal acquisition was possible at SNRs as low as -2 dB, exhibiting a 4 dB improvement over the previous demodulator.



# Contents

<b>List of Figures</b>	<b>3</b>
<b>List of Tables</b>	<b>5</b>
<b>List of Abbreviations</b>	<b>7</b>
<b>Summary</b>	<b>7</b>
<b>1 Introduction</b>	<b>9</b>
1.1 Background Information and Literature Review . . . . .	10
1.2 Problem Statement . . . . .	11
1.3 Theoretical Content and Methodology . . . . .	12
1.4 Experimental Set-up . . . . .	13
1.5 Results, Outcome and Relevance . . . . .	14
<b>2 Methodology</b>	<b>15</b>
2.1 Signal Replication . . . . .	15
2.1.1 Modulation . . . . .	15
2.1.2 BPSK Modulation . . . . .	16
2.1.3 Side-band Suppression . . . . .	17
2.1.4 AWGN Channels . . . . .	19
2.2 Carrier Recovery . . . . .	23
2.2.1 Squaring Loop . . . . .	23
2.2.2 Remodulator . . . . .	24
2.2.3 Costas Loop . . . . .	26
2.2.4 Power and Lock Detect . . . . .	28
2.2.5 Loop Tuning . . . . .	28
2.3 Clock and Data Recovery . . . . .	38
2.3.1 Early-late Gate . . . . .	40
2.3.2 Mueller and Muller . . . . .	41
2.3.3 Gardner . . . . .	41
2.3.4 Loop Tuning . . . . .	42
2.3.5 Signal Interpolation . . . . .	43
2.4 Packet Synchronization . . . . .	44
2.5 Packet Quality and Meta-Data Collection . . . . .	46
<b>3 Results</b>	<b>47</b>
3.1 Initial Signal Acquisition Performance . . . . .	47
3.2 Bit-Error Rate Analysis . . . . .	49
3.3 Packet Reception Rate Analysis . . . . .	52
3.4 Telemetry Client . . . . .	59
3.4.1 Software Architecture . . . . .	59
3.4.2 Real-time Performance . . . . .	63

<b>4</b>	<b>Conclusions</b>	<b>64</b>
<b>5</b>	<b>Discussion and Recommendations</b>	<b>67</b>
5.1	Error Correcting Codes . . . . .	67
5.1.1	Background Information . . . . .	68
5.1.2	Analysis . . . . .	69
5.2	Pulse Shaping . . . . .	71
5.2.1	Background Information . . . . .	71
5.2.2	Analysis . . . . .	72
	<b>References</b>	<b>74</b>
	<b>Appendices</b>	<b>76</b>
A	DUDe BER Analysis . . . . .	76
B	Conference Paper . . . . .	80

# List of Figures

1.1	High level diagram of a BPSK demodulator . . . . .	12
1.2	Simulation structure . . . . .	13
2.1	Carrier signal of BASK, BFSK and BPSK modulation . . . . .	16
2.2	Power spectrum diagrams of BASK and BPSK modulated signals . . . . .	17
2.3	Hilbert transform of sample binary data . . . . .	18
2.4	Power spectrum diagram of a SSBSC-BPSK modulated signal . . . . .	18
2.5	Conditional probability density function with BPSK modulation . . . . .	20
2.6	Bit error rate (BER) curve for BPSK modulation . . . . .	21
2.7	Power spectrum diagrams of BPSK modulated signals received through a simulated AWGN channel . . . . .	22
2.8	Block diagram of the Squaring loop . . . . .	24
2.9	Block diagram of the remodulator . . . . .	25
2.10	Block diagram of the Costas loop . . . . .	26
2.11	Comparison of common Costas loop discriminator responses . . . . .	27
2.12	Costas Loop with power and lock detection . . . . .	28
2.13	Digital filters . . . . .	30
2.14	Settling response of PI-controller and low-pass filter . . . . .	31
2.15	Doppler shift . . . . .	33
2.16	Frequency tracking behaviour for various integral gains . . . . .	33
2.17	Lock time for various various integral gains . . . . .	34
2.18	Estimated uncertainties of all objects in LEO in radial (U), along-track (V) and out-of-plane (W) directions [8] . . . . .	35
2.19	Doppler shift error due to TLE inaccuracies . . . . .	36
2.20	Received baseband signal and the effect of matched filter . . . . .	39
2.21	Early-late gate clock recovery . . . . .	41
2.22	Mueller and Muller clock recovery . . . . .	41
2.23	Gardner clock recovery . . . . .	42
2.24	Received baseband and the sampling instant . . . . .	43
2.25	Two consecutive sample points for various data-rates . . . . .	44
2.26	Two interpolation techniques . . . . .	44
2.27	Carrier tracking performance based on various packet synchronization techniques . . . . .	45
3.1	Initial signal acquisition under low SNR conditions . . . . .	48
3.2	BER of the new demodulator . . . . .	50
3.3	BER of the new demodulator when operating in coherent mode . . . . .	51
3.4	Ratio of measured BER to the theoretical BER . . . . .	51
3.5	BER of the new demodulator when operating at a data-rate of 9600 bps . . . . .	52
3.6	Simulated Doppler shift compared to observation . . . . .	53
3.7	Probability of successful packet reception . . . . .	56
3.8	Measured SNR during the selected Delfi-n3Xt passes . . . . .	56
3.9	Received packets vs. SNR (pass 1) . . . . .	58

3.10 Hierarchical view of the telemetry system . . . . .	59
3.11 Software architecture of the telemetry client . . . . .	59
3.12 The newly developed telemetry client . . . . .	62
5.1 BER of various coding techniques . . . . .	69
5.2 Pulse shaping . . . . .	71
5.3 Frequency spectrum of a 9600 bps BPSK modulated signal at a carrier offset of 10 kHz	73

# List of Tables

2.1	Various types of Costas discriminators . . . . .	27
2.2	Stability and accuracy of various types of oscillators . . . . .	32
2.3	Orbital parameters of the Delfi-n3Xt . . . . .	32
2.4	Acquisition time for various various integral gains . . . . .	34
3.1	Orbital conditions of 5 Delfi-n3Xt passes . . . . .	53
3.2	Packet statistics using the new demodulator . . . . .	54
3.3	Packet statistics using the DUDe demodulator . . . . .	55

# List of Abbreviations

<b>AGC</b>	Automatic Gain Control
<b>AM</b>	Amplitude Modulation
<b>AWGN</b>	Additive White Gaussian Noise
<b>BASK</b>	Binary Amplitude Shift Keying
<b>BER</b>	Bit Error Rate
<b>BFSK</b>	Binary Frequency Shift Keying
<b>BPSK</b>	Binary Phase Shift Keying
<b>CRC</b>	Cyclic Redundancy Check
<b>DLL</b>	Delay-Locked Loop
<b>DSB</b>	Double Side-Band
<b>DSBSC</b>	Double Side-Band Suppressed Carrier
<b>DSP</b>	Digital Signal Processor
<b>DUDe</b>	Delft Universal Data extractor
<b>ECC</b>	Error Correction Code
<b>ESA</b>	European Space Agency
<b>ExtIO</b>	External Input/Output
<b>FIR</b>	Finite Impulse Response
<b>FM</b>	Frequency Modulation
<b>FPGA</b>	Field Programmable Gate Array
<b>GPP</b>	General Purpose Processor
<b>IF</b>	Intermediate Frequency
<b>IIR</b>	Infinite Impulse Response
<b>ISI</b>	Intersymbol Interference
<b>LEO</b>	Low Earth Orbit
<b>LOS</b>	Line-Of-Sight
<b>MAC</b>	Multiply Accumulate
<b>NORAD</b>	North American Aerospace Defence Command
<b>NRZ</b>	Non-Return to Zero

**OBC** On-Board Computer  
**OCXO** Oven Controlled Crystal Oscillator  
**PC** Personal Computer  
**PDF** Probability Distribution Function  
**PID** Proportional-Integral-Derivative  
**PLL** Phase-Locked Loop  
**PM** Phase Modulation  
**QAM** Quadrature Amplitude Modulation  
**RMS** Root Mean Squared  
**SDR** Software-Defined Radio  
**SNR** Signal-to-Noise Ratio  
**SSB** Single Side-Band  
**SSBSC** Single Side-Band Suppressed Carrier  
**TCXO** Temperature Compensated Crystal Oscillator  
**VCO** Voltage Controlled Oscillator  
**VHF** Very High Frequency  
**XO** Crystal Oscillator

# Preface

This report represents my master's thesis and the result of 7 months of effort. It serves to fulfil the final requirement for receiving my Master of Science degree in Aerospace Engineering from Delft University of Technology. The research outlined within this study was performed at the faculties of Aerospace Engineering as well as Electrical Engineering, Mathematics and Computer Science in the city of Delft.

The field of software-defined radios, and even more broadly modern digital communication systems, has always been very intriguing and interesting to me. As such, when I became aware of an opportunity to conduct my MSc thesis on this topic, I immediately seized it. Among the many universities currently developing CubeSats, Delft University of Technology is a leading institute in the small satellite domain. With two satellites already in orbit and operational, and more to be launched soon, the university's CubeSat program is one of the most established in the world. I'm glad to have had the opportunity to give back to a program that has given me so much knowledge and experience.

In the past 7 months, I've had the pleasure of working along side many talented individuals who have helped me immensely. I'm honoured to call them friends and would like to take this opportunity to thank them all. I would like to first and foremost dedicate this work to my amazing parents. Without their tireless efforts and endless support, none of my accomplishments would have been possible. I would like to give a special thanks to my supervisor Jasper Bouwmeester for his incredible patience, guidance and invaluable advice. I sincerely couldn't have wished for a better mentor. Behzad Nourani, a talented communications engineer and my uncle, has been a lighthouse in these uncharted waters for me and for that I am very grateful. Lastly, I would like to thank Nils von Storch, an incredible colleague, who tolerated my many questions and mistakes and guided me whenever I required assistance.

Ehsan Tofigh  
February 25, 2016  
The Hague

# Chapter 1

## Introduction

In this study, the design and implementation of a software-defined Binary Phase Shift Keying (BPSK) demodulator is described. Particular attention is given to improving the Bit-Error Rate (BER) and initial signal acquisition performance. The purpose of the new demodulator is to replace the current poorly performing demodulator for the upcoming DelFFi mission. To this end, the performance of the newly implemented demodulator is fully characterized in order to assess its suitability for this mission.

Among the many universities currently developing CubeSats, Delft University of Technology (TU Delft) is a leading institute in the small satellite domain. With two satellites already in orbit and operational, and two more to be launched within a year as part of the QB50 mission, the university's CubeSat program is one of the most established in the world. The Delfi-n3Xt mission is second in the development line of CubeSats and is successor to the successful Delfi-C<sup>3</sup> mission. In order to involve radio amateurs from all over the world, Delfi-C<sup>3</sup> and Delfi-n3Xt carry a transceiver operating in the amateur satellite segment of the VHF amateur radio frequency band.

Telemetry decoding software is provided to all participating radio amateurs which allows them to demodulate, decode and display telemetry data in real-time. Secondly, the telemetry client automatically transfers the collected packets to the central Delfi ground station for further processing and archival. This system allows telemetry data to be received from various amateur and professional ground stations all over the world thus effectively increasing the per orbit downlink budget. The Software-Defined Radio (SDR) approach provides the necessary flexibility to both the ground control operators as well as radio amateurs to adapt to future missions, with differing data-rates and modulation schemes, without costly equipment overhauls.

The telemetry decoding software, Delft Universal Data extractor (DUDe) has accomplished the aforementioned task for the Delfi-n3Xt mission. However, years of operation by ground operators has shown that the performance of this demodulator is not optimum and lacking behind state-of-the-art demodulators. To quantify the performance of the current demodulator, a limited study was conducted. The details of the performance analysis for this demodulator is provided in Appendix A. Although limited in scope, the study raised a number of concerns about the performance of the DUDe telemetry client. For example, the BER of this demodulator is twice as high as the theoretical value at low SNRs. The BER becomes 75 times higher than the predicted value at a SNR of 10 dB. Throughout the experiments, a number of other issues were discovered. For example, the carrier recovery loop would consistently lose synchronization at a SNR of 2 dB and below. Below a SNR of 1 dB, carrier lock was never achieved. Furthermore, the clock and data recovery component also presented signs of trouble. When data transitions were absent for a number of consecutive bits, the clock and data recovery algorithm of DUDe failed to sample the demodulated signal at the correct instant. The latter issue caused regular bit-slips when the transmitted bit sequence contained 6 or more consecutive high/low bits.

Comparing these results to the stated performance of both software and hardware demodulators, one can see an alarming discrepancy. As such, it was concluded that there is a wide gap between the performance of the DUDe demodulator and what is predicted by the theory. Furthermore, this demodulator is also under-performing when compared to other implementations of hardware and software demodulators. Some of the aforementioned issues can be attributed to a poorly tuned carrier recovery loop and a rudimentary clock and data recovery technique. Although far from comprehensive, the study clearly illustrated that further improvement to the current implementation is vital for the success of the DelFFi mission. Furthermore, the telemetry requirements such as data-rates for the future CubeSat missions such as the upcoming DelFFi mission have become much more stringent and are beyond the capabilities of the current demodulator.

To that end, this study outlines the design and implementation of a new telemetry client to replace DUDe for the upcoming DelFFi mission. The primary focus of the research is on implementing a high performance BPSK demodulator capable of demodulating a 9600 bps telemetry link in near real-time. BER and initial-signal acquisition performance is prioritized over other design criteria. Attention is given to optimize the demodulator towards the specific requirements and constraints of satellite communications.

## 1.1 Background Information and Literature Review

Over the past decade, Digital Signal Processor (DSP) based radios, often referred to as SDRs, have an increasingly prevalent role within wireless communication systems. Unlike traditional hardware radios which use electrical circuits to implement radio transceivers, SDRs implement significant aspects of these transceivers using software algorithms running on a DSP. The extensive use of software in these systems means that SDRs are much easier to modify and upgrade than their hardware-defined counterparts [10]. As a result, researchers and developers have been steadily replacing previously hardware-defined radio systems by SDRs.

In recent years, the field of SDR has witnessed the gap between scientific research discoveries and their eventual implementation in commercial systems significantly reduced. The boost in activity as a result of commercial interest has brought SDR research right into the consumer markets. Vaneli-Corali et al. [25] has compiled a large number of research trends within the field of SDR. They showed that the evolution towards SDR systems has been driven in part because of the advancement of the enabling technologies such as the Digital Signal Processors (DSPs), General Purpose Processors (GPPs) and Field Programmable Gate Arrays (FPGAs).

Every year, numerous journal articles declare that these advances in computing power have paved the way for traditional communications systems to be completely software defined. Yet, the research is almost entirely focused on simplifying the design and improving the performance, cost, reliability and power consumption of SDRs for terrestrial applications. Ulversoy [23] discovered that this research is driven by the fact that most consumer markets still rely on hardware-defined radios and represent a huge market for SDR systems once they are able to compete in the areas of cost and power consumption.

The requirements for satellite communications, however, vary significantly compared to consumer telecommunications markets. In satellite communications it is often beneficial to trade simplicity, low cost and low power with performance and robustness. This is specially true for the ground segment of satellite communication systems. In these systems, computational power is often abundant which allows (near) real-time demodulation of low data-rate telemetry signals. Most CubeSat missions employ a telemetry links with data-rates of only few tens of kilobits per second, thus making an SDR approach highly suitable. Even when higher data-rates are required and when real-time telemetry decoding is not essential, the received RF signal can be digitized and recorded onto hard drives. The pre-recorded RF signal can then be processed "off-line" and as such computational complexity and time become irrelevant. This means that an SDR system for a ground station can focus on

achieving the best possible performance at the cost of increased computational complexity and power consumption.

Ulversoy [23] also identified a number of potential opportunities which can be exploited when using SDR approaches. For instance, Maheshwarappa et al. [16] believes that "Software Defined Radio (SDR) is a key area to realise new software implementations for adaptive and reconfigurable satellite communication systems without changing any hardware device or feature". To prove their point, using the QB50 mission as a case study, they show that using a flexible SDR approach for ground control stations would result in significant increase in gathered telemetry data and thus scientific value, by using distributed ground stations. The QB50 mission is an international network of 50 CubeSats for multi-point, in-situ measurements in the lower thermosphere and re-entry research. Each satellite is designed and manufactured by a different university which may use a different modulation scheme and data-rate. SDR technology is the only method that would enable a cost effective distributed ground control station network.

However, a number of other requirements, constraints and challenges arise from the use of SDR for ground station receivers. For instance, a problem associated with satellite communications, as researched by Mevada et al. [17], is the fact that "the relative motion between satellite and ground station will be high and accelerated in nature". As a result of the time-varying relative motion between the satellite and the ground station, the Doppler offset keeps shifting. The rate of change of the Doppler shift will significantly affect the behaviour of the receiver and has to be taken into account at the ground station to achieve the best link performance. Furthermore, even though it was previously stated that computational capabilities present in most ground stations is sufficient to support real-time demodulation of low data-rate telemetry links, care must be taken to limit the number of required processing steps and select efficient algorithms.

Maheshwarappa et al. [16] also compiled a list of state-of-the-art SDR solutions that currently exist for ground control stations. However, the performance of these solutions were not characterized in terms of BER or compared to their terrestrial counterparts. Furthermore, the provided solutions are mostly derived from the previous terrestrial solution, with little or no modifications or optimizations for space applications. Therefore, it has become clear that a study into the design and implementation of a SDR-based demodulator, optimized for the specific use for ground stations, can have many positive consequences and can fill a significant gap in this field of technology.

## 1.2 Problem Statement

Arising from the conclusions drawn in Section 1.1, is the potential for research into the challenges and opportunities of SDR techniques within the field of satellite communications. While many researchers have produced working SDR based BPSK demodulators, few have tried to maximizing their performance for this specific purpose. This gap in knowledge presents an opportunity to deliver significant contributions to the growing field of SDR communications, while simultaneously realizing the more practical goal of producing an improved telemetry client for the upcoming DeFFi mission. Furthermore, establishing a benchmark for performance, that can be employed by researchers, would hopefully accelerate future work into high performance DSP based demodulators. By taking advantage of this benchmark, the performance of the current demodulator (DUDe) can also be assessed.

The purpose of this study is to design and implement a high performance software-defined BPSK demodulator. Particular attention is given to the BER optimization as well as initial signal acquisition when computational power is abundant and power consumption constraints don't exist. All of the conflicting design parameters of an SDR, such as complexity, cost and power consumption are exchanged in favour of performance with the ultimate goal of shrinking the gap between the theoretical BER and the achievable real-world BER. To reach these goals, state-of-the-art as well as other common DSP techniques and algorithms will be analysed, tuned and optimized in

a systematic approach. The primary research question, arising from main objective of the study is: what is the highest achievable performance for a software-defined BPSK demodulator for the DelFFi mission? The main research question can be subdivided into two parts: what are the lowest achievable BER and lowest required SNR for reliable signal acquisition for this demodulator? To develop such a demodulator other questions must first be answered. These questions include: which existing SDR techniques and algorithms are required to achieve the best performance? How can the various demodulator parameters be optimized for space applications?

The result of the study is a quantifiable performance figure of the developed BPSK demodulator. Experiments, in addition to computer simulations are conducted to measure the BER and initial signal acquisition under various SNRs as well as environmental and orbital conditions. The pre-recorded RF signals obtained from the Delfi-n3Xt mission are used during the experiments in order to ensure the suitability of the implemented BPSK demodulator for the upcoming mission.

### 1.3 Theoretical Content and Methodology

In order to identify the key parameters that may impact the performance of the demodulator, mathematical models of various components of a typical BPSK demodulator will be derived. Figure 1.1 depicts the high level diagram of a typical BPSK demodulator. Special attention is given to the carrier recovery loop behaviour and clock and data recovery loop models. These two modules are the largest contributors to the BER and initial signal acquisition performance and largely define the performance of a BPSK demodulator. Identifying the equations that govern their behaviour is the key to selecting the parameters that can be tuned to achieve the optimum performance for different mission characteristics.

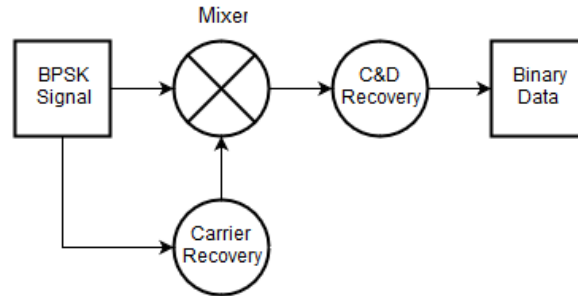


Figure 1.1: High level diagram of a BPSK demodulator

One of the contributions of this work to the body of science is to produce a method for linking the identified carrier as well as clock and data recovery loop parameters to mission and orbital parameters. This would result in a systematic approach for optimizing the demodulator for a particular mission and is achieved by combining accurate orbital simulations with demodulation simulations.

To establish a figure for the performance, it is important to study the effect of noise on the reliability of the BPSK demodulation. In particular, this study deals with the design and performance characteristics of optimum receivers for the BPSK demodulation method when the channel corrupts the transmitted signal by the addition of white Gaussian noise. The AWGN channel model is a channel whose sole effect is addition of a white Gaussian noise process to the transmitted signal. Although the AWGN channel model seems very limiting, its study is beneficial from two points of view. First, noise is the major type of corruption introduced by many channels. Therefore isolating it from other channel impairments and studying its effect results in a better understanding of its effect on all communication systems. Second, the AWGN channel, although very simple, is a good

model for studying space communication channels where, unlike most terrestrial channels, the effects of multipath, terrain blocking and interference are negligible [3].

Simulations of the orbital trajectory, channel corruption and demodulator behaviour would result in a complete performance analysis of the proposed solution and will be used as the basis to evaluate the advantages of the new demodulator with respect to the previous implementation. To prove the validity of the findings, all results will be validated experimentally using real-world collected signals (from previous satellite missions).

## 1.4 Experimental Set-up

In this section a brief outline of the experimental set-up is provided. As outlined in the previous sections, the subject of the study is the performance of the BPSK demodulator under various data-rates and orbital conditions. For this study the performance parameter is treated as the two variables, BER and SNR during initial signal acquisition. In order to evaluate these variables a two step approach is taken.

Firstly, a MATLAB script will be developed that will modulate a random binary sequence using the selected BPSK modulation parameters. The produced baseband signal is up converted to the Intermediate Frequency (IF) plus an offset frequency. The purpose of the offset frequency is to emulate the Doppler shift and any inherent clock drift between the transmitter and receiver. This offset is independently generated based on an orbital simulation using the mission parameters. Finally, the IF signal is fed through a simulated AWGN channel. The reconstructed signal is directly passed to the developed demodulator in order to assess the performance. The demodulated signal is compared to the transmitted signal to evaluate the BER. Furthermore, the carrier loop lock signal is used to measure the initial signal acquisition performance. This quick and simple method provides the necessary flexibility and convenience to evaluate and optimize a large number demodulator parameters in a short time. The simulation structure is depicted in Figure 1.2.

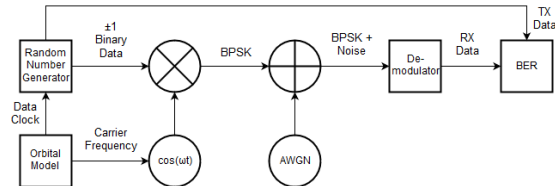


Figure 1.2: Simulation structure

Care is taken to ensure that as many sources of noise and RF distortion are accounted for in these simulations. For instance, the simulated signal at the IF frequency, is outputted using a Digital-to-Analogue Converter (DAC) output and a simple audio cable loops the signal back to the receiver input to be processed by the telemetry client. The purpose of this approach is to account for the effects of digitization error (as a result of the limited resolution of the ADC) on the performance of the demodulator. Furthermore, this experiment provides the means to verify the operation of the telemetry client as a complete system.

Other effects such as the signal distortion by the power amplifiers as well as ionospheric and atmospheric distortions cannot be simulated reliably and can only be characterized with the actual transmitter in the loop. So to further prove the validity of the simulations and to account for the signal distortions caused by the transmitter as well as the communication channel, a final experiment is conducted on the actual pre-recorded signals that were received from previous missions. However, since the actual transmitted data is not known, a BER figure cannot be calculated directly. Since the data packets are encoded with checksums, some statistical data on the BER can be obtained using this experiment. Furthermore, the initial signal acquisition time can still be measured even if the

transmitted data is unknown. This experiment is used to validate the results of the simulations and since it incorporates the complete transmission-reception chain, it is one of the most comprehensive test set-ups possible within the means of this study.

## 1.5 Results, Outcome and Relevance

With the experimentation set-up established, it is time to focus on the study itself. As previously stated, the goal of the research is to design and implement a high performance software-defined BPSK demodulator that minimizes the BER when computation power is abundant. For this study the demodulator performance parameter is based upon the two variables, BER and initial signal acquisition performance. As mentioned previously, in order to evaluate these variables, MATLAB scripts will convert a random sequence of data into a sequence of digital signal samples that are fed into the developed demodulator. The aim is to make this signal match or closely resemble the signal that the demodulator would receive from an actual satellite in orbit. Apart from the generated signal replica, pre-recorded signal samples from previous missions are also processed by the demodulator.

To optimize the various parameters of the demodulator, the equations governing behaviour of the demodulator must be analysed. The most influential parameters are the damping factor and loop bandwidth of the carrier recovery loop and the integral and proportional gains of the clock and data recovery loop. As previously mentioned, the novelty of the study is to devise a method of optimizing these parameters based on the particular mission parameters. Variables such as the eccentricity, orbital altitude and ground control station location play an important role in optimizing these parameters.

The expected result of the study is the development of a systematic method for optimizing the demodulator parameters based on the mission parameters. The optimally tuned BPSK demodulator would display a BER figure lower than the state-of-the-art demodulators. Furthermore, initial signal acquisition should be improved under various SNRs as well as orbital conditions. The study will also ensure the suitability of the implemented BPSK demodulator for the upcoming mission. The final result of the research is a telemetry client software (implementing the newly developed high performance BPSK demodulator) that can be used by the ground control operators for the Delfi mission.

One of the contributions of this study towards the betterment of the scientific body is the establishment of a baseline for performance of BPSK demodulators in satellite communications, which allows future researchers to have a reference to quantify their improvements, optimizations and advancements. To achieve this, the results of this study will be published within a journal or conference article. Furthermore, it will hopefully accelerate the level of research conducted in the area of high performance demodulators for space communications. In order to be able to optimize the BER and initial signal acquisition of the developed demodulator, all key parameters of such a system are analysed individually. As a result, key areas where the highest gains can be acquired are identified which will help direct the path of future research.

Apart from the scientific significance of this study, the newly developed BPSK demodulator will help the Delfi ground control team to receive telemetry at a higher data-rate and more reliably than the previous missions. Furthermore, the higher performance of this demodulator will enable hundreds of radio amateurs around the world to listen to the Delfi and other satellites (employing BPSK modulation scheme) using cheap hardware equipment and low gain antennas and will ultimately help attract more individuals towards the scientific and engineering fields.

# Chapter 2

## Methodology

In this chapter the design and implementation of the new high performance demodulator is outlined. First, a brief overview of the BPSK signal and transmission channel is provided in Section 2.1. The implementation and tuning of the carrier recovery as well as data and clock recovery components of the demodulator are described in Sections 2.2 and 2.3 respectively. Finally, the topic of packet synchronization is discussed in Section 2.4.

### 2.1 Signal Replication

In order to effectively design and implement a demodulation solution, it helps to fully understand the process of modulation. In this section a detailed layout of the Single Side-Band Suppressed Carrier BPSK (SSBSC-BPSK) modulation technique as used by the Delfi missions is provided. The mathematical and digital aspects of this modulation technique are fully analysed as well.

#### 2.1.1 Modulation

Modern communication systems are pass band communication systems in which the information is modulated over a carrier signal to transmit this signal over long distances. Modulation is necessary for a number of reasons such as: maximizing the usage of bandwidth available from the analogue channels, decreasing the antenna size and simultaneously using the channel by multiple transmitters [2]. The information to be transmitted can either be a digital or an analogue signal often referred to as the baseband signal. Digital data is composed of finite number of symbols whereas analogue signals have a continuous value within the available range. In both cases the baseband signal can be used to modulate the carrier signal in three ways: amplitude  $A$ , frequency  $f_c$  and phase  $\phi$ .

$$S(t) = A \cdot \cos(2\pi f_c t + \phi) \tag{2.1}$$

In the analogue domain these modulations are known as Amplitude Modulation (AM), Frequency Modulation (FM) and Phase Modulation (PM). Their corresponding counterparts in the digital domain are Amplitude Shift Keying (ASK), Frequency Shift Keying (FSK) and Phase Shift Keying (PSK). The latter can be seen in Figure 2.1.

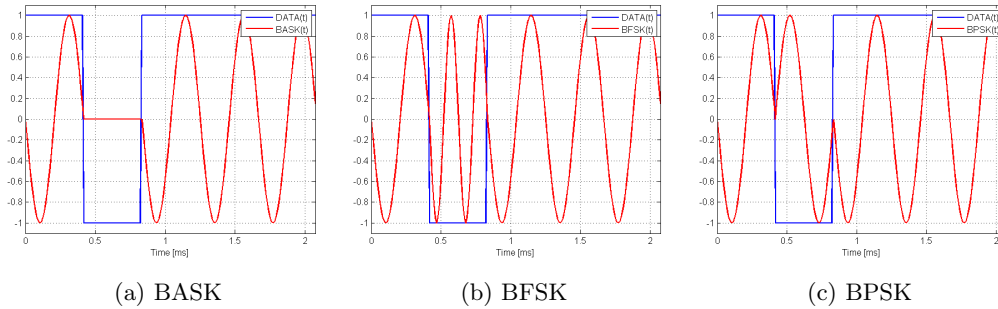


Figure 2.1: Carrier signal of BASK, BFSK and BPSK modulation

### 2.1.2 BPSK Modulation

BPSK has excellent BER performance, strong anti-interference performance, fast transfer rates, low complexity, as well as other prominent features. These are some of the contributing factors that make BPSK one of the main modulation modes of satellite communication systems. The main disadvantage of this modulation scheme is its low spectral efficiency (compared to QPSK and MSK) and production of significant adjacent channel interference. Conventionally, digital modulation and demodulation are done using a dedicated chip. So its flexibility has been greatly restricted. With the rapid rise of processing capabilities of microprocessors and development of SDR technologies, it has become possible to realize the building blocks of BPSK demodulators in software and to achieve a fully software-defined BPSK demodulator.

In a BPSK modulation scheme, the phase of the carrier is shifted  $180^\circ$  for one data symbol and not shifted for the other. This is commonly referred to as 'antipodal' phase shift modulation [15]. The mathematical equation for this process is:

$$BPSK_N(t) = \cos(2\pi f_c t + (1 - DATA_N(t)) \cdot \pi) \quad (2.2)$$

Where  $DATA_N = 0, 1$  and  $N$  is advanced at the bit-rate and is generally much lower than the frequency of the carrier (the cosine function) [7]. The bandwidth of the primary lobe of a BPSK modulated signal is  $2/T$ , where  $T$  is the symbol period. Since BPSK transmits one bit per symbol and the bit-rate is  $1/T$ , the required bandwidth for a BPSK modulated signal is given as:

$$f_w = \frac{2}{T} = 2 \cdot \text{bit-rate} \quad (2.3)$$

If the binary signal represented by the 0,1 square wave is converted into a  $\pm 1$  or polar waveform, the modulated signal will show phase reversals as the signal changes level.

$$BPSK_N(t) = \cos(2\pi f_c t + DATA_N(t) \cdot \frac{\pi}{2}) \quad (2.4)$$

The mathematical representation for this process is given in Equation 2.4, where  $DATA_N$  is restricted to  $\pm 1$ . Since, shifting the phase of a carrier (a sinusoid) by  $180^\circ$  is mathematically equivalent to reversing the magnitude of the carrier, the following amplitude modulation process can be substituted, interchangeably:

$$BPSK_N(t) = DATA_N(t) \cdot \cos(2\pi f_c t) \quad (2.5)$$

The modulation techniques in Equations 2.4 and 2.5 are referred to as BPSK and Double Side-Band Suppressed Carrier BPSK (DSBSC-BPSK) respectively, and when the phase shift is restricted to

$180^\circ$  between opposing symbols, there is no difference between the two equations [7]. Keen observers will realize that even though Equation 2.5 represents a PSK modulation scheme, its form is identical to ASK. In fact looking at Figure 2.2 which represents the power spectrum diagrams of these signals, one can observe a clear resemblance.

The only difference is that  $DATA_N$  is restricted to  $\pm 1$  in the case of a BPSK modulated signal. That means the signal now has a mean value of zero (zero DC level) and the carrier will not be present in the spectrum of the modulated signal. The spectrum will be that of a DSBSC signal (See Figure 2.2b). It is well known that transmission of the carrier is a waste of power (2/3 of the power is contained in the carrier) since the information is carried by the side-bands [15]. Figure 2.2b does an excellent job at illustrating the suppressed carrier in the BPSK spectrum. Furthermore, a 6 dB loss (as compared to BPSK) can be observed in the BASK spectrum, coinciding with the 66% of power being wasted in the carrier.

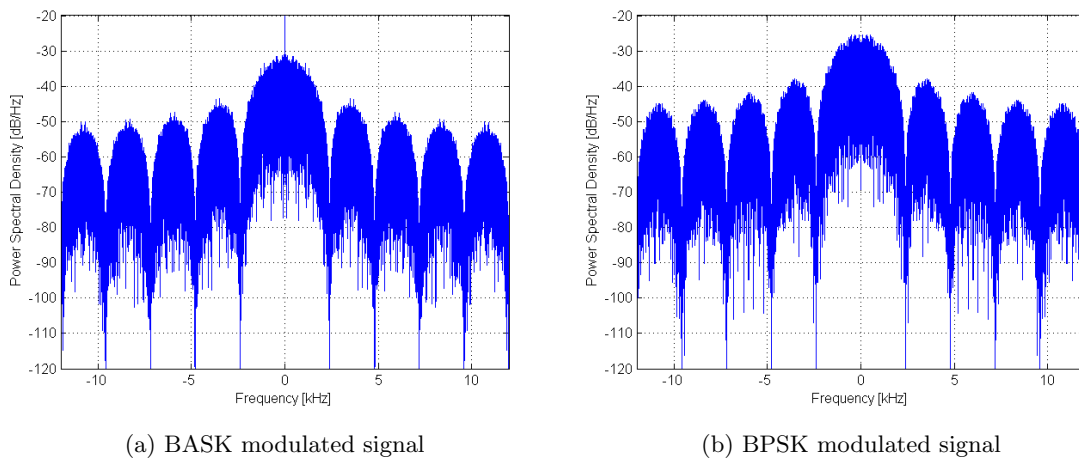


Figure 2.2: Power spectrum diagrams of BASK and BPSK modulated signals

### 2.1.3 Side-band Suppression

In order to reduce the required transmitter power and use the available bandwidth more efficiently, Single Side-Band modulation (SSB) or Single-Side-Band Suppressed-Carrier (SSBSC) can be used. Normal AM modulation produces a signal that occupies twice the bandwidth of the original baseband signal. SSB modulation avoids this bandwidth doubling at the cost of increased device complexity and more difficult tuning at the receiver.

In this section, the carrier frequency is used to refer to the RF frequency. The RF frequency is the frequency used by the transmitter at the up-conversion stage to produce the signal at the final transmission frequency (VHF in this case). In the case of DSBSC-BPSK, the resultant RF spectrum is simply the baseband spectrum mirrored at the carrier frequency. The upper side-band (the half of the BPSK spectrum that exists above the carrier frequency) is identical to that of the modulating signal, except shifted up to where the RF frequency was the DC point in the spectrum of the original signal. The lower side-band (similarly, the part of the modulated signal that exists below the carrier) contains identical information to the upper side-band, except its spectrum is a mirror image of the carrier.

From Equation 2.6, it can be seen that SSBSC-BPSK has the same mathematical form as Quadrature Amplitude Modulation (QAM). However in this case, the quadrature part of the signal is not driven by an independent symbol stream and instead depends on the in-phase baseband signal [7]:

$$SSBSC\text{-}BPSK_N(t) = DATA_N(t) \cdot \cos(2\pi f_c t) - \overline{DATA_N}(t) \cdot \sin(2\pi f_c t) \quad (2.6)$$

Where,  $\overline{DATA_N}$  is the Hilbert transform of  $DATA_N$  as illustrated in Figure 2.3. The spectrum of the signal expressed in Equation 2.6 is illustrated in Figure 2.4. It is important to note, that Equation 2.6 denotes the mathematical model of the SSBSC-BPSK modulation. In practical applications, side-band suppressed signals are generated by passing a double side-band signal through an analogue or digital filter to block the unwanted parts of the spectrum.

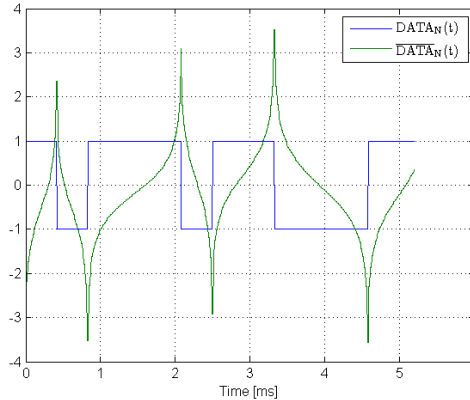


Figure 2.3: Hilbert transform of sample binary data

Side-band suppression however does come at a cost. Since the lower and upper side-bands of a DSB-BPSK modulated signal are mirror images, they will "fold" onto each other when multiplied with the carrier wave. This means that the two side-bands of the signal will coherently add while the Additive White Gaussian Noise (AWGN) will randomly add. Thus, the Gaussian noise increases according to a Root Mean Squared (RMS) relationship, which results in an inherent Signal-to-Noise Ratio (SNR) advantage, or "processing gain" of 3 dB above that of the SSB-BPSK signal. However, assuming a constant transmission power, the transmission of a DSB signal exhibits a 3 dB loss (when compared to SSB) because the available power is used to amplify twice the bandwidth. Thus the net effect is zero in case of power limited transmission systems.

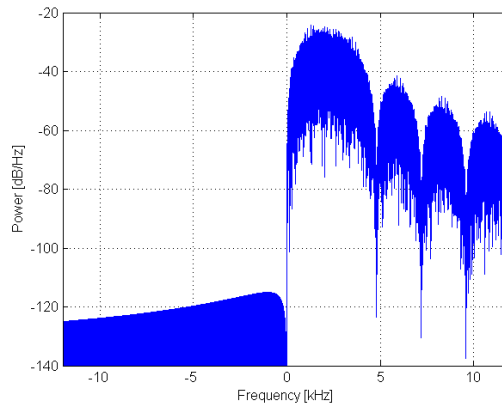


Figure 2.4: Power spectrum diagram of a SSBSC-BPSK modulated signal

### 2.1.4 AWGN Channels

The purpose of the modulator in a transmitter is to produce a signal waveform based on the bit-stream of the message. The resulting signal is then transmitted to the receiver over a communication channel which will inevitably distort the original signal. Communication channels can suffer from a variety of impairments that contribute to errors. These impairments include noise, attenuation, distortion, fading, and interference. Characteristics of a communication channel determine which impairments apply to that particular channel and which are the determining factors in the performance of the channel. Noise is present in all communication channels and is the major impairment in many communication systems.

In this section the effect of the addition of white Gaussian noise on the transmitted signal is described and simulated. The AWGN channel model is a type of communication channel whose sole effect is addition of a white Gaussian noise process to the transmitted signal [19]. The mathematical representation of an AWGN channel is described by the following equation:

$$r(t) = s(t) + n \quad (2.7)$$

where  $s(t)$  is the transmitted signal which,  $n(t)$  is the noise and  $r(t)$  is the received waveform. The receiver observes the received signal  $r(t)$  and, based on this observation, makes the optimal decision about which message symbol was transmitted. An optimal decision refers to a decision rule which results in minimum error probability.

Although the AWGN channel model seems very limiting, its study is beneficial from two points of view. First, noise is the major type of corruption introduced by many channels. Therefore isolating it from other channel impairments and studying its effect results in better understanding of its effect on all communication systems. Secondly, the AWGN channel, although very simple, is a good model for studying space communication channels where, unlike most terrestrial channels, the effects of multipath, terrain blocking and interference is negligible [19].

The noise in Equation 2.7 follows the Gaussian probability distribution function:

$$p(x) = \frac{1}{\sqrt{2\pi\sigma^2}} e^{-\frac{(x-\mu)^2}{2\sigma^2}} \quad (2.8)$$

Where the mean  $\mu$  is zero and the power spectral density of the noise is given as  $\sigma^2 = N_0/2$ .

In the case of BPSK modulation, the received signal given in Equations 2.9 and 2.10 corresponds to a transmission of a 0 and 1 bit respectively.

$$r = s_0 + n \quad (2.9)$$

$$r = s_1 + n \quad (2.10)$$

The conditional probability distribution (PDF) of  $r$  for the two cases is (see Figure 2.5):

$$p(r|s_0) = \frac{1}{\sqrt{\pi N_0}} e^{-\frac{(r+\sqrt{E_b})^2}{N_0}} \quad (2.11)$$

$$p(r|s_1) = \frac{1}{\sqrt{\pi N_0}} e^{-\frac{(r-\sqrt{E_b})^2}{N_0}} \quad (2.12)$$

Assuming that  $s_0$  and  $s_1$  are equally probable (i.e.  $p(s_0) = p(s_1) = 1/2$ ), the threshold zero forms the optimal decision boundary. If the received signal  $r$  is less than or equal to zero, then the receiver assumes  $s_0$  was transmitted. Similarly, a received signal larger than zero, is assumed to be  $s_1$ .

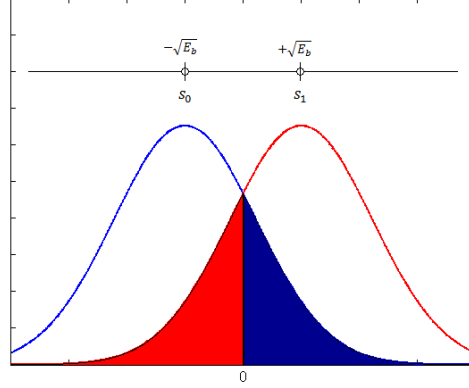


Figure 2.5: Conditional probability density function with BPSK modulation

With zero as the optimal decision boundary, the probability of error when  $s_0$  is transmitted (the blue area in Figure 2.5) can be calculated as:

$$p(e|s_0) = \frac{1}{\sqrt{\pi N_0}} \int_0^{\infty} e^{-\frac{(r+\sqrt{E_b})^2}{N_0}} dr = \frac{1}{\sqrt{\pi}} \int_{\sqrt{\frac{E_b}{N_0}}}^{\infty} e^{-z^2} dz = \frac{1}{2} \operatorname{erfc} \left( \sqrt{\frac{E_b}{N_0}} \right) \quad (2.13)$$

Where  $\operatorname{erfc}(x) = \frac{2}{\sqrt{\pi}} \int_x^{\infty} e^{-x^2} dx$ , is the complementary error function.

Similarly, the probability of error when  $s_1$  is transmitted (the red area in Figure 2.5) is given by:

$$p(e|s_1) = \frac{1}{\sqrt{\pi N_0}} \int_{-\infty}^0 e^{-\frac{(r-\sqrt{E_b})^2}{N_0}} dr = \frac{1}{\sqrt{\pi}} \int_{-\infty}^{-\sqrt{\frac{E_b}{N_0}}} e^{-z^2} dz = \frac{1}{2} \operatorname{erfc} \left( \sqrt{\frac{E_b}{N_0}} \right) \quad (2.14)$$

From Equations 2.13 and 2.14 the bit error probability can be obtained:

$$P_b = p(s_0)p(e|s_0) + p(s_1)p(e|s_1) = \frac{1}{2} \operatorname{erfc} \left( \sqrt{\frac{E_b}{N_0}} \right) \quad (2.15)$$

Figure 2.6 illustrates the Bit Error Rate (BER) for BPSK modulation achieved by an optimum receiver. This curve can be used as a guide for evaluating the performance of real receivers.

The relative power of noise (as compared to the signal power) in an AWGN channel is typically described by quantities such as:

- Signal-to-Noise Ratio (SNR) per sample
- Ratio of bit energy to noise power spectral density ( $E_b/N_o$ )
- Ratio of symbol energy to noise power spectral density ( $E_s/N_o$ )

The relationship between  $E_b/N_o$  and  $E_s/N_o$ , both expressed in dB, is as follows:

$$E_s/N_o \text{ (dB)} = E_b/N_o \text{ (dB)} + 10 \log_{10} k \quad (2.16)$$

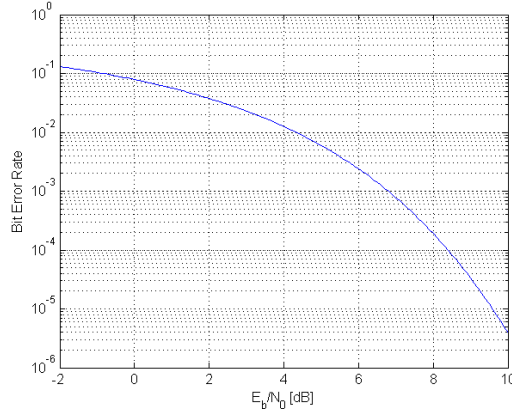


Figure 2.6: Bit error rate (BER) curve for BPSK modulation

Where  $k$  is the number of information bits per symbol. In the case of BPSK,  $k = 1$  resulting in the collapse of Equation 2.16 into Equation 2.17, and thus proving that the bit energy is equal to the symbol energy for a BPSK signal.

$$E_s/N_o \text{ (dB)} = E_b/N_o \text{ (dB)} \quad (2.17)$$

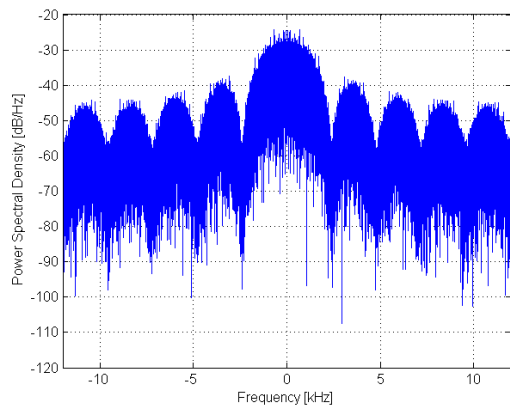
Similarly, the relationship between  $E_s/N_o$  and SNR, both expressed in dB, is as follows:

$$E_s/N_o \text{ (dB)} = 10 \log_{10} (T_{sym}/T_{samp}) + SNR \text{ (dB)} \text{ For complex signals} \quad (2.18)$$

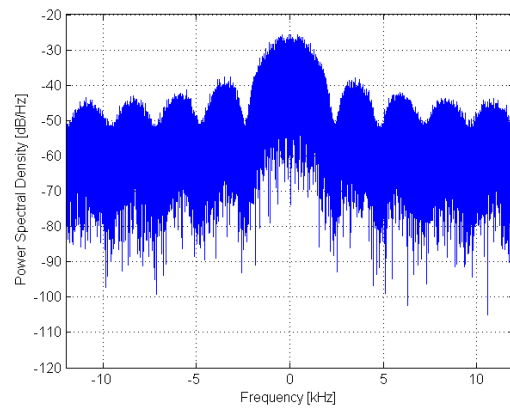
$$E_s/N_o \text{ (dB)} = 10 \log_{10} (0.5T_{sym}/T_{samp}) + SNR \text{ (dB)} \text{ For real signals} \quad (2.19)$$

Where  $T_{sym}$  is the signal's symbol period and  $T_{samp}$  is the signal's sampling period.

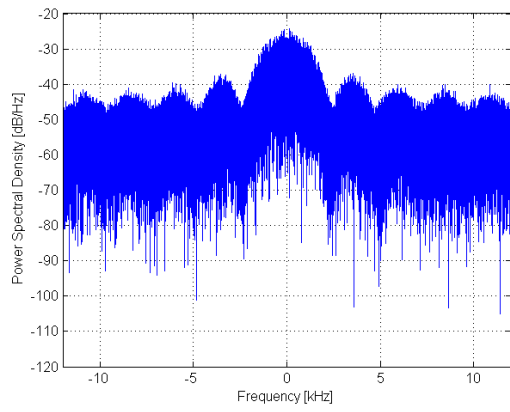
Figure 2.7 illustrates the spectrum of a 2400 bps BPSK modulated signal at 4 different  $E_b/N_0$ . Since, in this study only digital modulation is discussed, to improve the legibility, SNR and  $E_b/N_0$  are used interchangeably.



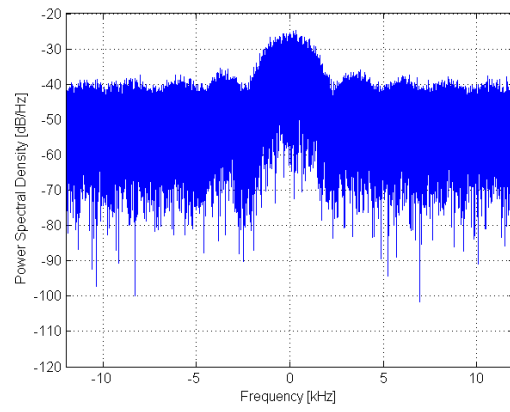
(a)  $E_b/N_o = 20$  dB



(b)  $E_b/N_o = 15$  dB



(c)  $E_b/N_o = 10$  dB



(d)  $E_b/N_o = 5$  dB

Figure 2.7: Power spectrum diagrams of BPSK modulated signals received through a simulated AWGN channel

## 2.2 Carrier Recovery

For optimum reception of the transmitted data in a BPSK modulated signal, both the carrier as well as data clock signals must be available at the receiver. The extraction or regeneration of these signals from the noisy digitally modulated received waveform, is the task of the carrier recovery and clock and data recovery systems. This section focuses on the operating principles of the former.

As previously discussed, to improve the power efficiency of the transmitter, most modern modulation techniques choose to fully suppress the carrier in the transmitted signal. This has the added benefit that now all the transmitted energy resides in the information carrying side-bands. Unfortunately, without the presence of a carrier, ordinary Phase Locked Loops (PLL) cannot be used for carrier recovery. This means that complex carrier recovery techniques are required. Many factors have to be considered during the selection and development of a carrier recovery system. Here, only the basic operating principles of these systems are surveyed. For the sake of simplicity, only BPSK modulation is considered.

The task of carrier recovery in most telecommunication applications can be accomplished by one of the following three types of carrier recovery methods: multiplication loop (such as a squaring loop for BPSK), remodulator loop and Costas loop. Other types of carrier recovery schemes are extensions or modifications of these techniques [12].

### 2.2.1 Squaring Loop

In the case of a squaring loop, carrier recovery is performed by a frequency doubler (mixer) circuit. The output of the frequency doubler is given by:

$$[DATA_N(t) \cdot \cos(2\pi f_c t + \phi)]^2 = \frac{1}{2} DATA_N(t)^2 \cdot [\cos(4\pi f_c t + 2\phi)] \quad (2.20)$$

Where,  $\phi$  is the phase offset.

This technique relies on the fact that, since the BPSK modulation causes  $\pm 180^\circ$  phase transitions, its second harmonic will be phase-modulated by an ambiguous  $\pm 360^\circ$ , meaning that the second harmonic is an unmodulated carrier at twice the frequency of the original carrier. This can be seen from Equation 2.20. Since,  $DATA_N(t) = \pm 1$  then  $DATA_N(t)^2 = 1$  and the output of the frequency doubler is unmodulated.

Since the second harmonic is also phase coherent to the original carrier, dividing this signal by two will result in the regeneration of the exact modulating carrier signal. One of the benefits of the squaring loop carrier recovery technique is its simplicity. It is therefore very simple to analyse and understand. However, as evident from Figure 2.8, the regenerated carrier takes a different signal path compared to the modulated signal. This means that the modulated signal needs to be delayed before being demodulated by the recovered carrier signal. If the delay is not properly maintained, the resulting phase-error can significantly reduce the BER performance. In practice, controlling the phase offset (due to the presence of various filters in the signal path) will be somewhat complicated and application dependent. [9]. Figure 2.8 illustrates a simplified overview of this carrier recovery technique.

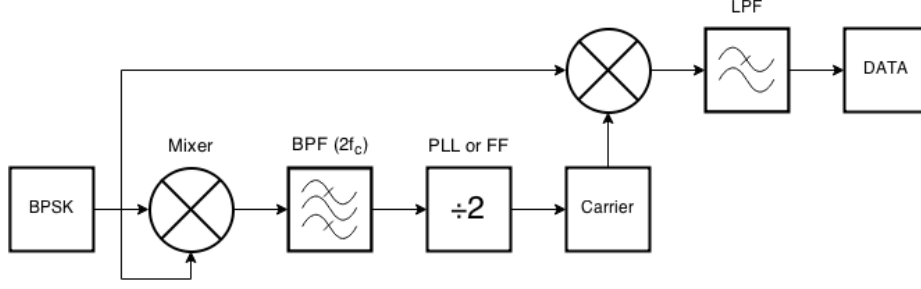


Figure 2.8: Block diagram of the Squaring loop

### 2.2.2 Remodulator

The block diagram of a remodulator (sometimes referred to as decision feedback loop) contains both a demodulator and a modulator [20] (see Figure 2.9). Assuming that the PLL has achieved phase-locked condition, the output of the VCO is given by:

$$2\cos(4\pi f_c t + \phi_0) \quad (2.21)$$

Then the output of the demodulator is:

$$DATA_N(t - t_d) \cdot \cos(\phi_i - \phi_i) \quad (2.22)$$

Where  $t_d$  represents the time delay of the low-pass filter involved in the demodulator and  $(\phi_i - \phi_i)$  denotes the phase error of the PLL. This demodulated signal modulates the recovered carrier in the modulator to produce:

$$2 \cdot DATA_N(t - t_d) \cdot \cos(\phi_i - \phi_i) \cdot \cos(4\pi f_c t + \phi_0) \quad (2.23)$$

Equation 2.23 is multiplied in the phase detector by the delayed input signal  $DATA_N(t - t_d) \cdot \sin(2\pi f_c t + \phi_i)$ . The input signal has to be delayed in order to cancel the effect of the delay in the demodulator. Neglecting the sum frequency component, the phase detector output is obtained as:

$$DATA_N^2(t - t_d) \cdot \cos(\phi_i - \phi_0) \cdot \sin(\phi_i - \phi_0) \approx \sin(2\phi_e) \quad (2.24)$$

It is now obvious that the overall strategy of the remodulation loop carrier recovery scheme is to mix the received signal with a regenerated signal. The main disadvantage of this technique is that the delay of the receiver lies inside the feedback loop. It is well known that any delay can have severe consequences in any control loop. By comparison, the squaring loop instantly compares its VCO signal to the receiver input and adapts the phase and frequency. A fast acting loop can adjust to a phase disturbance in less than a symbol period, thereby avoiding a bit error during that interval. Furthermore, the computational burden of this technique is rather high due to its complexity.

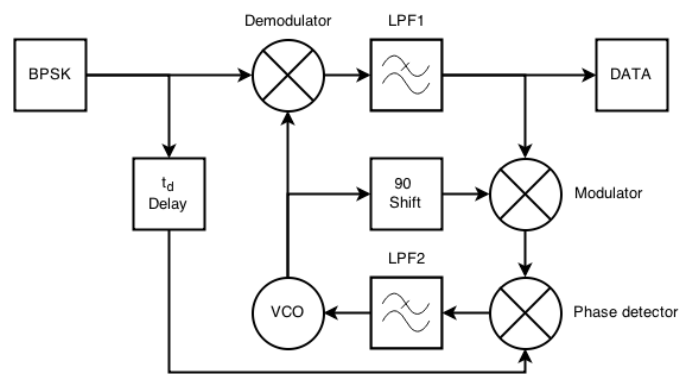


Figure 2.9: Block diagram of the remodulator

### 2.2.3 Costas Loop

Another feedback algorithm (similar to the remodulator loop) is the Costas loop. Feedback carrier recovery techniques offer higher noise rejection properties compared to feed-forward techniques (such as squaring loop) but suffer from longer loop settling times. However, unlike the remodulator loop, the Costas loop instantaneously feeds back the baseband signals  $I(t)$  and  $Q(t)$  to a phase detector which produces an error signal that drives the VCO. As such, there is no detection delay in the loop. Furthermore, the Costas loop can recover the carrier and demodulate the received signal simultaneously. This makes it highly computationally efficient. These advantages are the reason for selecting the Costas loop as the carrier recovery technique for the new high performance demodulator.

The operating principle of the Costas loop carrier recovery is "to iterate its internally generated carrier, the VCO, into the correct phase and frequency based on the principle of coherency and orthogonality" [4].

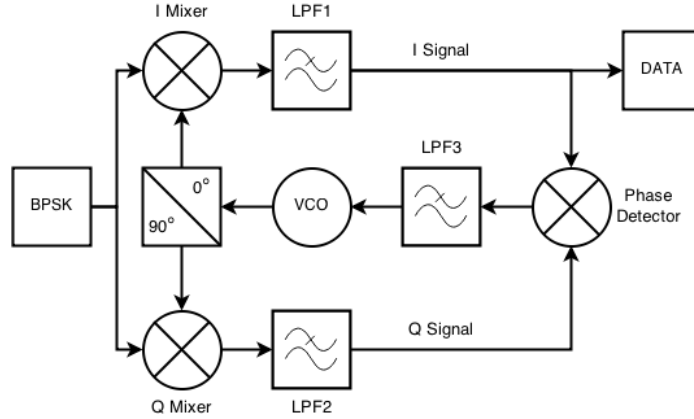


Figure 2.10: Block diagram of the Costas loop

The Costas loop in Figure 2.10 contains two multiplications. The received signal is multiplied by both the locally generated carrier signal as well as a  $90^\circ$  phase-shifted version of it. The objective of the Costas loop is to maximise and minimize the energy in the  $I$  (in-phase) and  $Q$  (quadrature) arms respectively. This is accomplished with a feedback mechanism driving the oscillator. The multiplication in the  $I$  arm yields the following sum:

$$DATA_N(t) \cdot \cos(2\pi f_c t) \cdot \cos(2\pi f_c t + \phi) = \frac{1}{2} DATA_N(t) \cdot \cos(\phi) + \frac{1}{2} DATA_N(t) \cdot \cos(4\pi f_c t + \phi) \quad (2.25)$$

Where  $\phi$  is the phase difference between the phase of the input signal and that of the local replica of the carrier phase. Similarly, the multiplication in the quadrature arm gives the following results:

$$DATA_N(t) \cdot \cos(2\pi f_c t) \cdot \sin(2\pi f_c t + \phi) = \frac{1}{2} DATA_N(t) \cdot \sin(\phi) + \frac{1}{2} DATA_N(t) \cdot \sin(4\pi f_c t + \phi) \quad (2.26)$$

By low-pass filtering the resulting signals, the double frequency terms can be removed which leaves the following signals intact:

$$I_N = \frac{1}{2} DATA_N(t) \cdot \cos(\phi) \quad (2.27)$$

$$Q_N = \frac{1}{2} DATA_N(t) \cdot \sin(\phi) \quad (2.28)$$

The phase error of the local carrier replica can be found in Equation 2.29 and is used as the feedback term to the carrier oscillator.

$$\frac{I_N}{Q_N} = \frac{\frac{1}{2} DATA_N(t) \cdot \cos(\phi)}{\frac{1}{2} DATA_N(t) \cdot \sin(\phi)} = \tan(\phi) \quad (2.29)$$

$$\phi = \tan^{-1} \left( \frac{Q_N}{I_N} \right) \quad (2.30)$$

From Equation 2.30, it can be seen that the phase error is minimized when the correlation in the quadrature-phase arm is zero and the correlation value in the in-phase arm is maximum. The arctan phase detector (also referred to as discriminator) in Equation 2.30 is the most precise of the Costas discriminators. There are alternative discriminators that require substantially less processing power and computational time at the cost of reduced precision. These discriminators are described in Table 2.1 and are generally used for real-time demodulation applications. However for this application, the arctan discriminator is used. The latest generation of GPPs contain built-in hardware that can calculate trigonometry functions very efficiently.

Discriminator	Description
$D = \text{sign}(I_N) \cdot Q_N$	The discriminator output is proportional to $\sin(\phi)$
$D = I_N \cdot Q_N$	The discriminator output is proportional to $\sin(2\phi)$
$D = \tan^{-1} \left( \frac{Q_N}{I_N} \right)$	The discriminator output is the phase error

Table 2.1: Various types of Costas discriminators

Figure 2.11 depicts the response of 3 types of Costas loop discriminators. These phase discriminator outputs are calculated using the equations within Table 2.1.

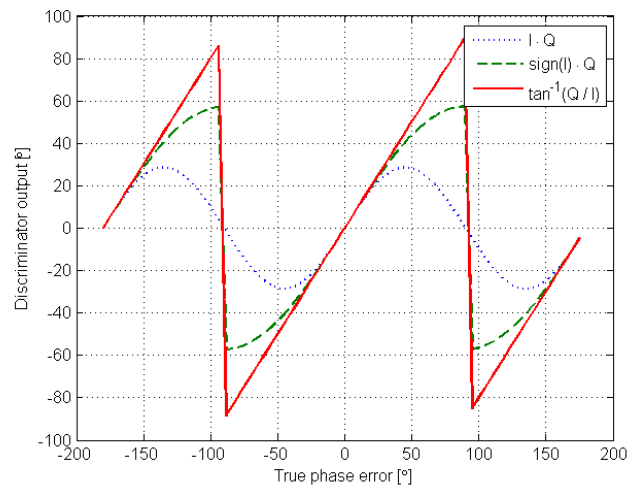


Figure 2.11: Comparison of common Costas loop discriminator responses

### 2.2.4 Power and Lock Detect

One of the other advantages of the Costas loop is the fact the loop produces various signals that may serve other beneficial purposes. For instance, it can be observed that the in-phase mixed signal is equal to:

$$I(t)|_{\phi_e=0} = A \cdot DATA(t) \quad (2.31)$$

This shows that when the loop is locked ( $\phi_e = 0$ ), the in-phase arm produces an output proportional to the input data. Hence the data can be demodulated directly within the Costas loop after phase lock occurs.

As it can be observed from Equation 2.32, squaring, low-pass filtering and subtracting the arm signals produces an output that indicates phase lock ( $\cos(2\phi_e)$  approaches 1 as  $\phi_e$  approaches 0) and can therefore be used as a lock detector. Furthermore, when  $\phi_e = 0$ , this generates an output proportional to the average signal power, which may be used as the input of an Automatic Gain Control (AGC) system.

$$I^2(t) - Q^2(t) = A^2 DATA^2(t) \cos(2\phi_e) \quad (2.32)$$

Lastly, when the power from both arms are added, a measurement of the total RF input power is obtained and can therefore be used for RF power control.

$$I^2(t) + Q^2(t) = A^2 DATA^2(t) + n_s^2 + n_c^2 = \text{Total power} \quad (2.33)$$

Where,  $n_s$  and  $n_c$  are signal and carrier noise. The modified Costas Loop is shown in Figure 2.12.

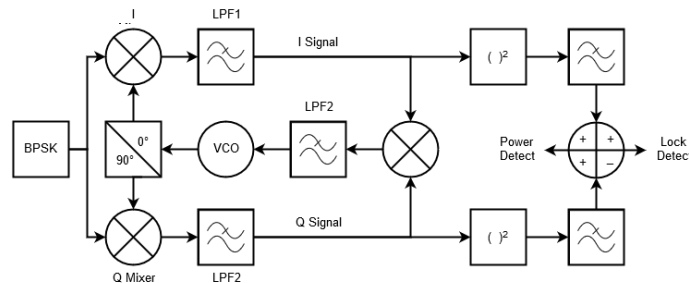


Figure 2.12: Costas Loop with power and lock detection

### 2.2.5 Loop Tuning

At it can be seen from Figure 2.12, there are a number of filters that govern the behaviour and performance of the Costas loop. In order to be able to optimally tune these filters, it is vital to understand how they affect the overall response of the loop. This section attempts to provide an insight into this matter.

#### Arm Filters

The in-phase and quadrature arm filters (LPF1 and LPF2) are low-pass filters used to eliminate the double frequency component generated by the multiplier. Knowing that no filter is ideal, a residual of the sum term always exists, but generally it's sufficiently attenuated. Both arm filters

must be completely identical in terms of characteristics. As a result of component variations and manufacturing tolerances, creating identical analogue filters is extremely difficult if not impossible. For this reason, Costas loop implementations are much more prevalent in digital receivers where realizing identical filter responses is a trivial task.

Similar to analogue filters, a digital filter is used to suppress or enhance certain frequencies of a signal. However, in a digital filter, this is accomplished using mathematical operations on a sampled, discrete-time signal instead of using electronic components that operate on continuous-time signals. There are a number of different methods for analysing the behaviour of a particular digital filter. These methods are also often used to design and specify the various characteristics of the filters.

The most commonly used method is to compute the response of a filter to a known input, for instance an impulse. This is known as the impulse response (denoted as  $h_k$ ) and is a measurement of how a filter will respond to the Kronecker delta function. Digital filters can be separated into 2 classes: Infinite Impulse Response (IIR) and Finite Impulse Response (FIR). The impulse response of FIR filters can be obtained by convolving the input samples with the sequence of filter coefficients:

$$y_n = \sum_{k=0}^{n-1} b_k x_{n-k} \quad (2.34)$$

Unlike FIR filters, IIR filters are recursive. This means that the impulse response of these filters is dependant on the input samples as well as the previously calculated outputs:

$$\sum_{m=0}^{M-1} a_m y_{n-m} = \sum_{k=0}^{n-1} b_k x_{n-k} \quad (2.35)$$

Because the bandpass filter, incorporated into the analogue front-end, removes a large portion of the noise, the arm filter requirements are significantly reduced. In such a case, the most important requirement of the arm filter is to be wide enough to pass the data modulation without causing any distortions. In an ideal world, the implemented filter exhibits no signal distortion (at the relevant frequencies) and thus eliminates Inter-Symbol Interference (ISI). However in a practical design, computational complexity can grow boundlessly if no SNR degradation is allowed. An optimization of the arm filter means that its bandwidth must be wide enough to minimize ISI, while narrow enough to minimize noise.

Both types of filters have their own advantages and disadvantages. Overall, though, the advantages of FIR filters outweigh the disadvantages, so they are used much more than IIRs. Compared to IIR filters, FIR filters offer the following advantages:

- They can easily be designed to be "linear phase". Linear-phase filters delay the input signal without distorting its phase.
- They are simple to implement. As most microprocessors have a Multiply-Accumulate (MAC) instruction, the FIR calculation can be done by repeating a single instruction.
- They can achieve decimation (reducing the sampling rate) and interpolation (increasing the sampling rate) while filtering a signal.
- They are numerically stable. When implemented on an actual processor, finite-precision arithmetic must be used for all calculations. In IIR filters, the numerical error of each operation is accumulated (due to feedback) which can cause a number of problems.

The main advantage of IIR filters as compared to FIR filters, is that they require a lower order ( $n$  in Equations 2.34 and 2.35) implementation to achieve a similar specification. Thus in theory, IIR filters require fewer number of calculations to reach the same passband, stop-band, ripple and roll-off requirements. However, due to the reasons explained above, fewer number of calculations does not

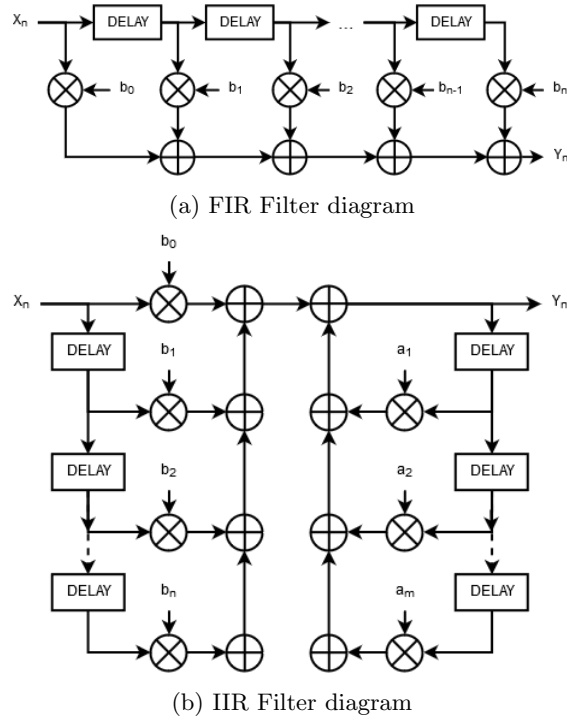


Figure 2.13: Digital filters

always equate to fewer number of operations on an actual processor. Furthermore, for this application computational time is abundant, the advantages of FIR filters outweigh their disadvantage and are thus used.

### Loop Filter

The output of the loop filter (depicted as LPF3 in Figure 2.10), is used to adjust the phase and frequency of the of the local carrier generated by the VCO (or NCO in a digital system). In most analogue systems, a simple low-pass filter fulfils this role. However, in digital implementations, this task is generally given to Proportional-Integral (PI) controllers.

PI controllers are a simplified form of Proportional-Integral-Derivative (PID) controllers. As a result of their solid performance in a wide variety of applications and operating conditions, this type of control algorithm has become very popular in all segments of the industry. Furthermore, their simplistic design has allowed the researcher and engineers to understand, analyse and develop creative models for tuning the controller parameters.

As evident from the name of this algorithm, PID controllers use three different parameters to calculate the optimum response to an input: proportional, integral and derivative. The output of the controller is given by:

$$u(t) = K_p e(t) + K_i \int_0^t e(\tau) d\tau + K_d \frac{de(t)}{dt} \quad (2.36)$$

Where,  $K_p$ ,  $K_i$  and  $K_d$  denote the coefficients for the proportional, integral and derivative terms. Some applications may require using only one or two terms to provide the appropriate system control. For the Costas Loop filter, the simpler PI controller is used (the derivative coefficient can be considered zero). Since the derivative term is highly sensitive to measurement noise, whereas the

absence of an integral term can prevent the system from reaching its target value, PI controllers have become very common.

In order to understand why a PI controller, as compared to a low-pass filter, can improve the performance of the Costas Loop, the relationship between the instantaneous phase and frequency must be first described. This relationship is represented in Equation 2.37.

$$f(t) = \frac{1}{2\pi} \frac{d\phi}{dt}(t) = \frac{\omega(t)}{2\pi} \quad (2.37)$$

The above equation illustrates that the integral of the Costas discriminator output (which is proportional to the phase error) is itself proportional to the instantaneous frequency error. Hence, the two outputs of the PI controller combined with the fact that the frequency and phase of an NCO can be independently adjusted, results in significantly improved loop settling time. Figure 2.14 clearly illustrates this advantage. The response of both loop filter approaches corresponding to a 10 Hz initial frequency offset is depicted in this figure. The oscillations in the frequency response of the low-pass filter are caused by the fact that the loop must compensate for the phase error by changing the frequency. This oscillation can never be fully eliminated by tuning the low-pass filter parameters.

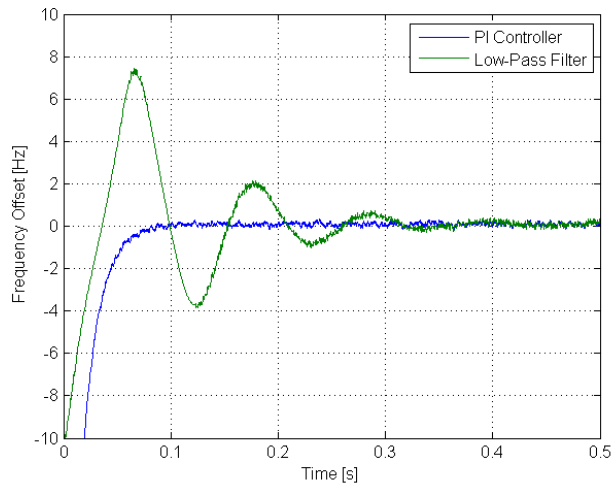


Figure 2.14: Settling response of PI-controller and low-pass filter

A PI controller relies only on the measured process variable, not on knowledge of the underlying process making the task of tuning somewhat challenging. The performance of a controller is often described in terms of the responsiveness of the controller to an error, the amount of overshoot when targeting the set-point and damping behaviour of the oscillations. It is important to note that the use of the PI or PID algorithms for control does not necessarily guarantee optimal control of the system or system stability. It is upto the designer to select the appropriate gains.

In the case of the Costas loop filter, the proportional gain determines the responsiveness of the loop to phase offsets (proportional to phase error). If the gain is too small, the loop will be unable keep pace with the phase drift and carrier lock is lost or never achieved. However, if the gain is too large, the controller over compensates for the phase offset resulting in phase oscillations and ultimately lower performance. Furthermore, a large gain makes the loop highly susceptible to noise which further degrades the performance. Similarly, the integral gain establishes the responsiveness of the loop to frequency offsets. The gain must be large enough to allow the loop to track fast frequency shifts that may occur throughout the mission lifetime. Again, increasing the gain too much results in lower noise rejection and potential frequency oscillations.

Type	Accuracy	Ageing (per year)	Temperature Stability ( $-55^{\circ}\text{C}$ to $85^{\circ}\text{C}$ )
XO	$5 \cdot 10^{-5}$	$3 \cdot 10^{-6}$	$1 \cdot 10^{-5}$
TCXO	$2 \cdot 10^{-6}$	$5 \cdot 10^{-7}$	$5 \cdot 10^{-7}$
OCXO	$1 \cdot 10^{-8}$	$5 \cdot 10^{-9}$	$1 \cdot 10^{-9}$
Rubidium	$5 \cdot 10^{-10}$	$2 \cdot 10^{-10}$	$3 \cdot 10^{-10}$

Table 2.2: Stability and accuracy of various types of oscillators

From the above paragraph, it is clearly evident that the lowest BER is achieved when the gains are as small as possible while still satisfying the minimum gain requirement. Both the proportional and integral gains can be determined by the worst case phase drift and frequency shift rate respectively. The primary contributor to the frequency shift is the Doppler shift. The Doppler shift is the change in frequency of a wave for an observer moving relative to its source and is described by Equation 2.38. Other effects such as clock drifts as a result of temperature variations and ageing also contribute to this shift. Without knowing the precise components used within the transmitter and receiver, it is impossible accurately calculate these effects. However, rough figures can be used to gain an understanding of the magnitude of these effects. Table 2.2 illustrates the typical values of these effects for a number of commonly used oscillators.

$$\Delta f = \frac{\Delta v}{c} f_0 \quad (2.38)$$

Where,  $\Delta f$  is the change in frequency,  $\Delta v$  is the velocity of the receiver relative to the source,  $c$  is the speed of light and  $f_0$  is the transmitted frequency.

It can be seen that the low performance crystal oscillators (XO) have a temperature stability of 10 Parts Per Million (PPM). This translates into a frequency shift of 1440 Hz (for a transmission frequency of 144 MHz) between the temperature range of  $-55^{\circ}\text{C}$  to  $85^{\circ}\text{C}$ . The DelfFi as well as the ground control station transceivers are equipped with temperature compensated crystal oscillators (TCXO) and as such display a two orders of magnitude improvement with regards to temperature stability. The frequency shift for these transceivers due to temperature effects (within the same range) is approximately 72 Hz. However, even in the orbital environment, the oscillators never experience such a wide temperature variations in a short amount of time. Hence, this effect is orders of magnitude less than the Doppler effect and is often neglected for most applications.

It is important to note that the initial accuracy of the oscillators plays no role in selecting the controller gains as this frequency offset is non-changing and constant. Furthermore, the frequency shift due to ageing of the oscillators are measured in spans of years and can safely be ignored. However, it is important to note that the initial frequency accuracy does increase the search space (in frequency domain) during the initial signal acquisition phase. However, since this offset is constant, it can be accounted for during initial testing of the transmitter.

Perigee	Apogee	Inclination	RAAN	Eccentricity	Period
593 km	780 km	$97.787^{\circ}$	$66.326^{\circ}$	0.01323	98.48 min

Table 2.3: Orbital parameters of the Delfi-n3Xt

In order to obtain a measure of the worst case Doppler shift, a simplified simulation of the Delfi-n3Xt orbit was created. The highest Doppler shifts are observed when the satellite's elevation is nearest to  $90^{\circ}$  and the perigee is precisely above the ground control station (Delfi-n3Xt's orbital parameters can be found in Table 2.3). Figure 2.15a illustrates the satellites velocity in the direction of the

ground station (left axis) and as a result the experienced Doppler shift (right axis). The satellite crosses over the ground station at precisely half way through the pass. The time derivative of this graph represents the rate of change of the Doppler shift and is depicted in Figure 2.15b. From this figure it can be observed that as the satellite pass over the ground control station, the Doppler shift changes at a rate of 35 Hz per second (a transmission frequency of 144 MHz was assumed).

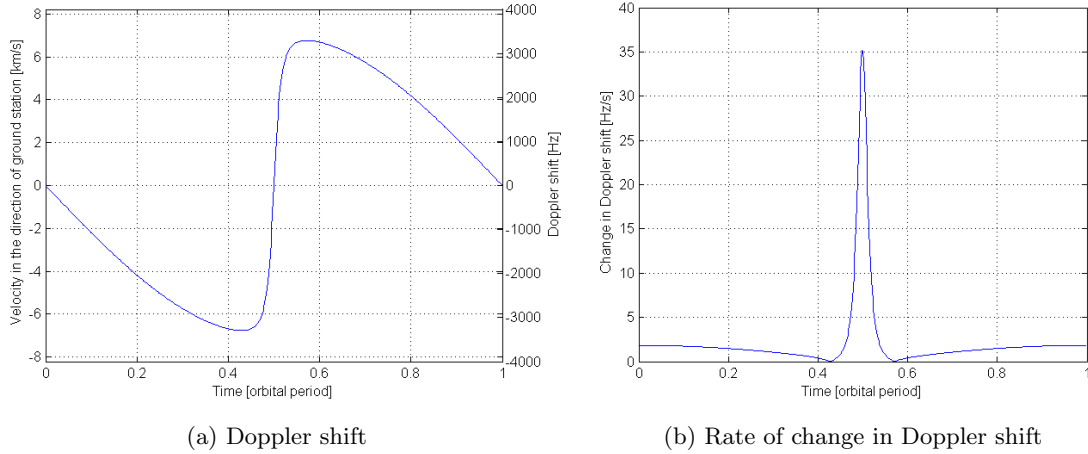


Figure 2.15: Doppler shift

This value is the determining factor in selecting the optimum integral gain. As long as, the gain is large enough to allow the loop to reliably track frequency shifts of 35 Hz per second, the highest noise rejection, lowest oscillation and thus best performance is achieved. It is important to note that such an approach for finding the best gain is not suitable for all applications. For instance, a very low gain also reduces the responsiveness of the loop and increases the time required to reach a steady state. In the case of satellite communications, a lock time of several seconds is generally deemed acceptable. Furthermore, loss of lock occurs very infrequently due to lack of obstructions. However, most terrestrial applications require very fast lock times to receive short and infrequent packets and to handle loss of lock and synchronizations.

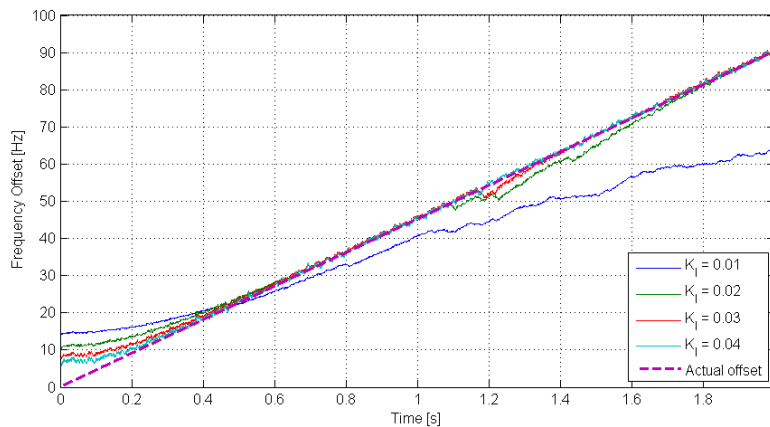


Figure 2.16: Frequency tracking behaviour for various integral gains

Figure 2.16 depicts the tracking behaviour of the Costas loop for different integral gains. A Doppler shift rate of 35 Hz per second is used in order to accurately simulate the conditions of the DelFFi mission. The figure shows that a minimum gain of 0.04 is required to be able to reliability track

Gain	0.04	0.06	0.1	0.4	0.8
Acquisition Time [s]	340	220	130	35	20

Table 2.4: Acquisition time for various various integral gains

frequency shifts of this magnitude. As previously stated, this gain would also result in a slow response to large frequency offsets. From Figure 2.17, it can be observed that it would take the Costas loop 17 seconds to lock onto a signal with a 200 Hz initial offset.

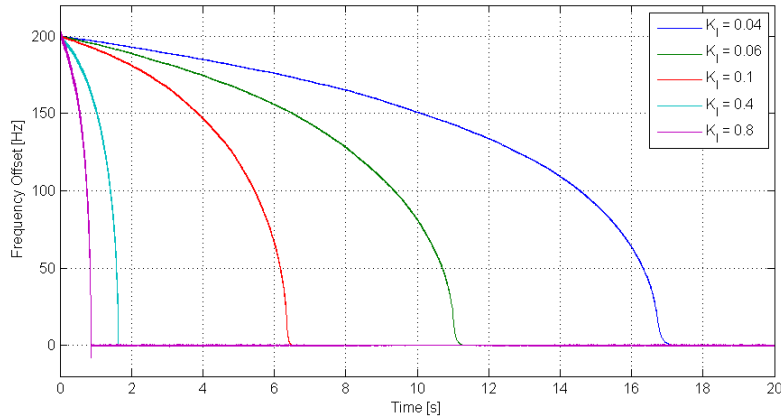


Figure 2.17: Lock time for various various integral gains

If no a priori knowledge of the satellite’s orbit is known, then the receiver has to search the entire range of possible frequency shifts (also known as search space). This is generally referred to as the unaided acquisition time and can be approximated as:

$$t_{Acquire} = \frac{\Delta f}{f_{bw}} \cdot t_{lock} \quad (2.39)$$

Where,  $\Delta f$  is the range of possible Doppler shifts,  $f_{bw}$  is the Costas loop bandwidth and  $t_{lock}$  is the lock time.

Table 2.4 contains the acquisition time for various integral gains. It can be seen that using the optimum gain (in terms of BER performance) of 0.04, the receiver could spend more than 5 minutes searching for a signal. Since, the contact time for LEO satellites is typically between 5 and 15 minutes, such a long acquisition time becomes problematic. To overcome this challenge, a two step variable gain is used. During the acquisition phase, the receiver would use a higher gain to reduce the acquisition time. Once carrier lock is achieved, a low gain is used to improve tracking performance and reduce the BER.

It is important to note that the acquisition time can also be significantly improved with the aid of accurate orbital parameters and orbital propagation algorithms to estimate the current Doppler shift of the satellite. Since orbital prediction software is already required for antenna tracking, this method is almost always employed. The rough estimate of this offset is generally calculated using the Two Line Element (TLE) sets which are made available on-line once the satellite is in its final orbit. This data is subsequently updated intermittently by North American Aerospace Defence Command (NORAD) [14]. Unfortunately, the TLE sets are not always very accurate.

The accuracy of the TLE sets is dependent upon a large number of factors. Some of these factors include: the type of sensors used for measuring the TLEs, the number of observations, the orbital

parameters as well as the conditions of the space environment. Sadly, all of these factors differ for each element set so the accuracy of the TLEs have to be determined on a case by case basis. To overcome these challenges, NORAD has been experimenting with various methods for incorporating TLE quality figures into the TLE sets themselves. Unfortunately, these methods have not been very successful and the figures are rarely available.

Instead of assessing the accuracy of the TLE sets, their consistency can be evaluated. By analysing the degree to which a TLE set agrees with the prior and subsequent sets, an estimate of the consistency can be obtained. Assuming that the errors in each TLE set is statistically unbiased (random), the average difference (in magnitude) between the TLE sets can provide a good estimate of the general accuracy of the data.

A study performed by the European Space Agency (ESA) on the TLE orbit errors of a large number of satellites can be found in [8]. This study assessed and categorized the estimated uncertainty of these objects. Figure 2.18 illustrates these values for Low Earth Orbiting (LEO) satellites. As it can be seen, the magnitude of the position error for most LEO objects is in the order of 1 km at epoch.

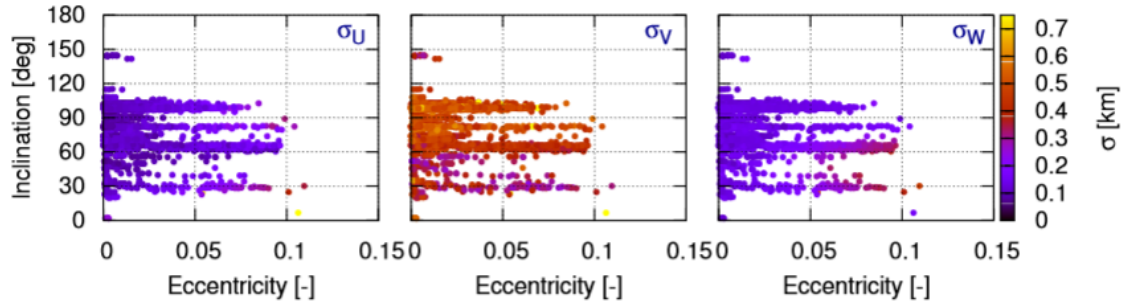


Figure 2.18: Estimated uncertainties of all objects in LEO in radial (U), along-track (V) and out-of-plane (W) directions [8]

The accuracy of the predicted position is also high dependent on the age of the TLE set. NORAD typically updates the TLE sets based on an "as-needed basis" rather than according to pre-determined schedule [14]. Some of the determining factors in the update frequency of the TLE sets are: the orbital parameters (specially the orbital altitude) and the manoeuvring capabilities of the satellite. For instance, a satellite in LEO, would display an unpredictable orbital trajectory due to the atmospheric drag (which is very difficult to model). As such, most satellites in LEO receive daily TLE updates. A satellite in a higher orbit which doesn't manoeuvre might only need updates once or twice a week.

An examination of the TLE sets for the Delfi-n3Xt reveals that on average a new set was made available every 30 hours. The study also showed that the positional error grows at a rate of 1 to 2 km per day [8]. This means that the Delfi-n3Xt's positional error can be in the order of  $\pm 3$  km right before the TLE sets are updated. Figure 2.19 shows the Doppler shift error as a result of a 3 km positional error. It can be seen that with the aid of orbital prediction software, the search space can be reduced to a 32 Hz window. This is referred to as aided signal acquisition and can greatly reduce acquisition time. However, the models used in this analysis are very crude and in reality this window is in the order of a few 100 Hz. This also confirmed in Figure 3.6a.

The selection of the proportional gain directly follows the selection of the integral gain. As previously stated in Equation 2.37, the change in phase between two sinusoidal waves is proportional to the difference between their frequencies multiplied by the elapsed time. For instance, if the frequency offset between two phase aligned waves is 0.1 Hz, the phase difference between them would be  $36^\circ$  after 1 second. After selecting the integral gain, the frequency variations and error after lock (as a

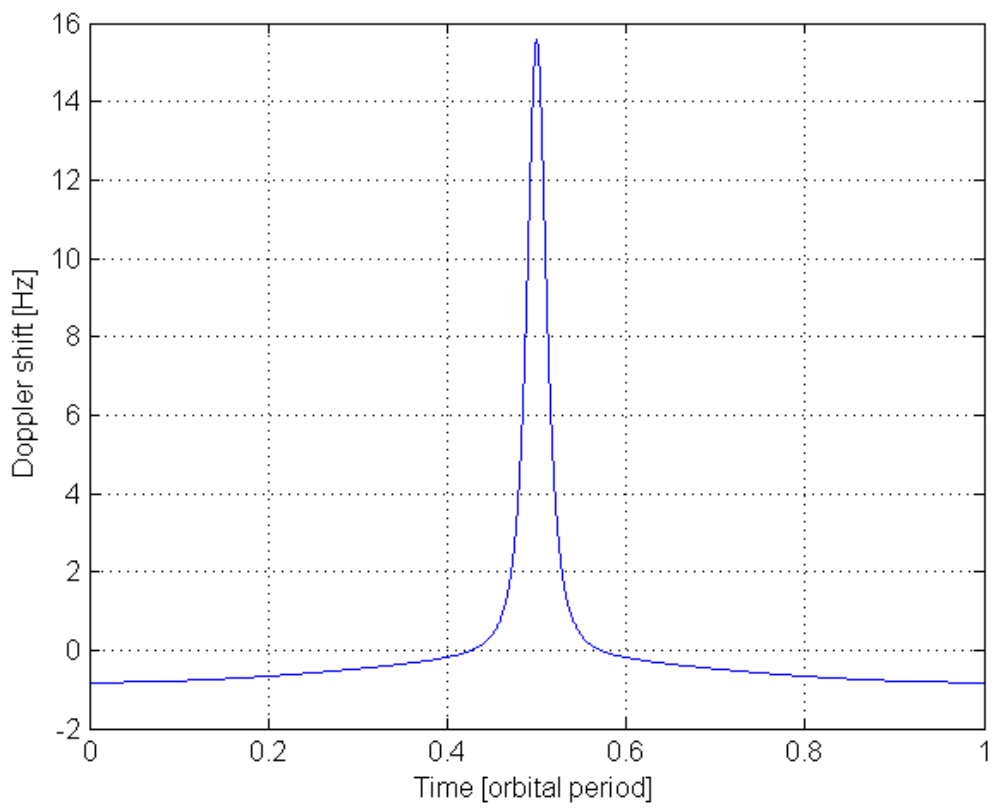


Figure 2.19: Doppler shift error due to TLE inaccuracies

## 2.2. CARRIER RECOVERY

---

result of noise) can be measured. This provides a figure upon which the proportional gain can be based.

## 2.3 Clock and Data Recovery

In order to maximise the BER performance, the demodulator of a digital communications system must be able to sample the baseband signal at the precise sampling time instant:

$$t_m = mT + \tau \quad (2.40)$$

Where,  $T$  is the symbol interval and  $\tau$  represents the time delay that occurs as a result of the propagation time of the signal from the transmitter to the receiver. In most communication systems, the symbol interval  $T$  (inversely proportional to the data-rate) is constant and known by both the receiver and the transmitter. The task of the Clock and Data recovery (sometimes referred to as symbol synchronization) is to determine the propagation delay  $\tau$  and use this knowledge to sample the baseband signal at the optimum instant.

Clock and data recovery is perhaps one of the most important functions that is performed by the receiver of a synchronous digital communication system and can greatly influence the final performance of the receiver [19]. This task is even more difficult in a satellite communications system. For instance, even though the data-rate of the transmitter is known, the received data-rate is affected by both the Doppler shift of the carrier as well as any inherent drift between two oscillators. As such the receiver must continuously calculate the most optimum sampling instant within the each symbol interval.

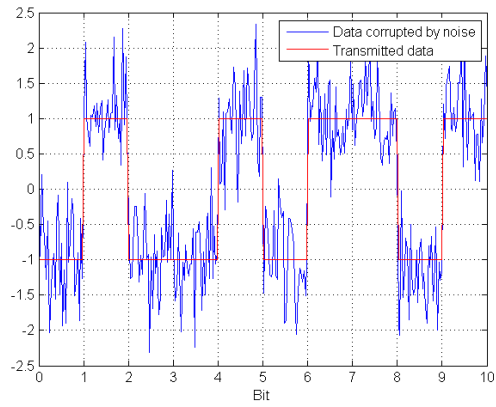
Similar to carrier recovery, clock and data recovery can be achieved using several different methods. Some communication systems choose to employ the same clock source (a master oscillator) on both the transmitter and the receiver. As such the receiver and the transmitter always remain synchronized and the task of clock and data recovery becomes trivial. For obvious reasons this method is not possible for satellite communications systems that are separated by a large distance. The transmitter can however transmit a copy of its clock signal along with the information signal. The receiver can then selectively extract the clock signal using a narrowband band-pass filter. This is perhaps the most simple form of clock and data recovery that can be used by satellite communication systems. However, this simplicity comes at the cost of increased transmission power (to transmit the extra clock signal) as well as increased bandwidth requirements.

These disadvantages have lead researchers to find another method for clock recovery. It is important to note that the clock signal of the transmitter can be directly inferred from the received baseband signal. This is referred to as self-synchronization which can be achieved using a number of methods. However, before that, a very important pre-processing step must be performed.

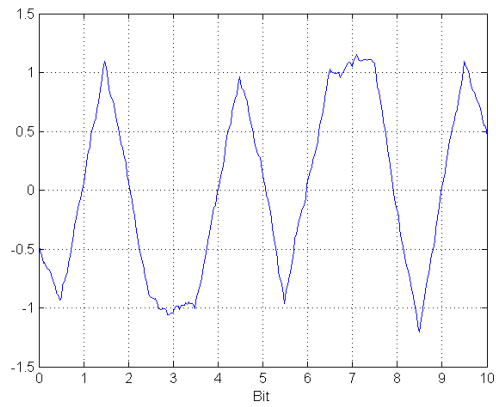
As previously explained, the in-phase arm of the Costas loop directly represents the received baseband signal after carrier synchronization is achieved. However this signal is corrupted with noise as a result of the AWGN channel effects. Figure 2.20a shows the received baseband signal for a SNR of 20 dB. A quick look at this signal does not reveal the originally transmitted sequence. If the receiver were to sample this signal, even at the perfect sampling instant, the resulting binary sequence would contain many bit errors. The situation would be far more severe than illustrated in Figure 2.20a if the SNR was closer to the typical value of 10 to 15 dB.

To reduce the probability of bit errors, the received signal is passed through a matched filter. In signal processing, "a matched filter is obtained by correlating a known signal, or template, with an unknown signal to detect the presence of the template in the unknown signal" [6]. In other words, a matched filter is equivalent to convolving the received signal with a conjugated time-reversed version of the symbol waveform. The matched filter is the optimal filter for maximizing the SNR in the presence of AWGN.

In the case of the transmitters used by the Delfi satellites, the filter should be matched to an Non-Return-to-Zero (NRZ) pulse waveform (equivalent to a "1" coded in NRZ code). This means that the impulse response of the ideal matched filter, assuming white (uncorrelated) noise should be an



(a) Received baseband signal



(b) Matched filter output

Figure 2.20: Received baseband signal and the effect of matched filter

averaged, scaled version of the signal. The width and scaling factor of filter coefficient array is dependant on the data-rate and sampling rate as shown in Equations 2.41 and 2.42.

$$\text{Width} = \frac{F_{\text{sampling}}}{\text{data rate}} \quad (2.41)$$

$$\text{Scaling factor} = \frac{\text{data rate}}{F_{\text{sampling}}} \quad (2.42)$$

For these equation it becomes obvious that in this case, a matched filter behaves as a weighted moving average filter which is also known as an integrate-and-dump filter. This is not always the case. For instance if pulse shaping is used by the transmitter to reduce Inter-Symbol Interference (ISI), the appropriate matched filter must also be used in the receiver. The principle and advantages of pulse shaping is discussed in Chapter 5. After convolving with the correct matched filter, the resulting signal,  $m_{\text{filtered}}(t)$  is:

$$m_{\text{filtered}}(t) = m(t) \star h(t) \quad (2.43)$$

Where,  $h(t)$  is the filter coefficient array and  $\star$  denotes the convolution operation. The resulting signal is depicted in Figure 2.20b. This figure shows that the filtered signal can now be accurately and correctly sampled using a comparator. Furthermore, it shows that the optimum sampling instant is at the middle of a bit period (peak of the signal).

### 2.3.1 Early-late Gate

Early-late gate clock and data recovery technique is one of the simplest methods and is often used in digital communication systems. As show in Figure 2.21, this technique involves taking 3 samples spaced by a sampling duration  $T_s$ . All 3 samples must be within a single symbol period, meaning that  $T_s$  must be equal or smaller than  $T/3$ . If the middle sample coincides with the optimum sampling instant, the early and late sampled at  $nTT_s$  and  $nT + T_s$ , respectively. The timing error can then be calculated as the difference between the late and early samples. The calculated timing error pushes the next sampling instant forward or backward until the timing error approaches zero. The timing error is computed as follows:

$$e = \{y[nT + T_s] - y[nT - T_s]\} y[nT] \quad (2.44)$$

The characteristics of this algorithm are:

- Generates error by using samples that are early and late compared to the ideal sampling point.
- Requires atleast three samples per symbol. Thus, it is impractical for high data rate systems

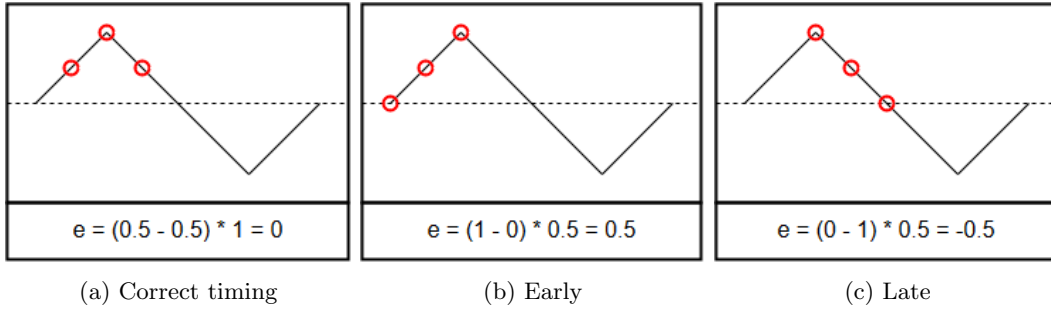


Figure 2.21: Early-late gate clock recovery

### 2.3.2 Mueller and Muller

Unlike the Early-Late gate algorithm, the Mueller-Muller clock and data recovery technique requires only a single sample per symbol but also the knowledge of the previous symbol decision in order to estimate the timing error [18]. Based on the timing error, the sampling frequency is increased or decreased until the timing error is minimized, as show in Figure 2.22. Timing error is computed as follows:

$$e = y[nT] \cdot \hat{y}[(n - 1)T] - \hat{y}[nT] \cdot y[(n - 1)T] \quad (2.45)$$

Where,  $\hat{y}$  is the decision outcome.

The characteristics of this algorithm are:

- Generates error based on previous and current samples and their decision outputs.
- Sensitive to carrier offsets. Carrier recovery must achieve lock prior to the clock recovery algorithm.
- Similar to PLL used in carrier recovery, adjusts the sampling instant by varying the sampling interval.
- Requires only one sample per symbol. Thus, it is often used for very high data rate systems

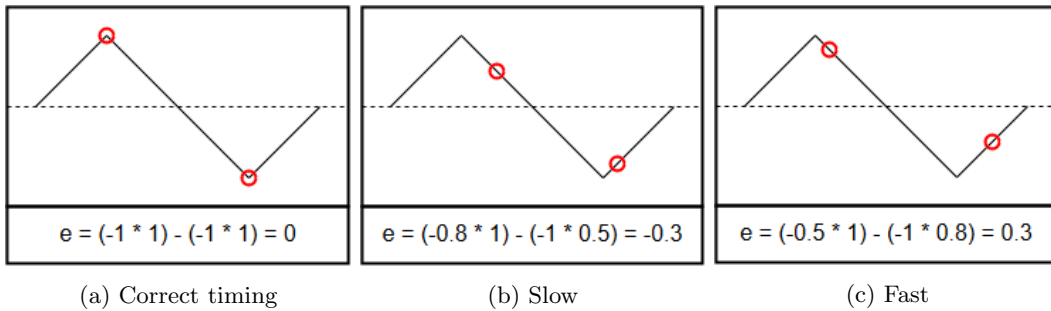


Figure 2.22: Mueller and Muller clock recovery

### 2.3.3 Gardner

The final clock and data recovery technique that is considered in this study, is the Gardner algorithm. This algorithm is somewhat similar to the Early-Late gate algorithm in the way the timing error is calculated. However, the Gardner algorithm requires only two samples per symbol and unlike the

Early-Late gate algorithm, the sampling interval is not constant and instead relies on the knowledge of the previous symbol timing to estimate the timing error for current symbol as shown in Figure 2.23. Timing error is computed as follows:

$$e = \{y[nT] - y[(n - 1)T]\} y[nT - T/2] \quad (2.46)$$

The characteristics of this algorithm are:

- Very widespread use.
- Insensitive to carrier offsets. The clock and data recovery loop can lock before the carrier recovery loop, which can often ease the task of carrier recovery.
- Requires two samples per symbol. Thus, it can be used for medium to high data rate systems

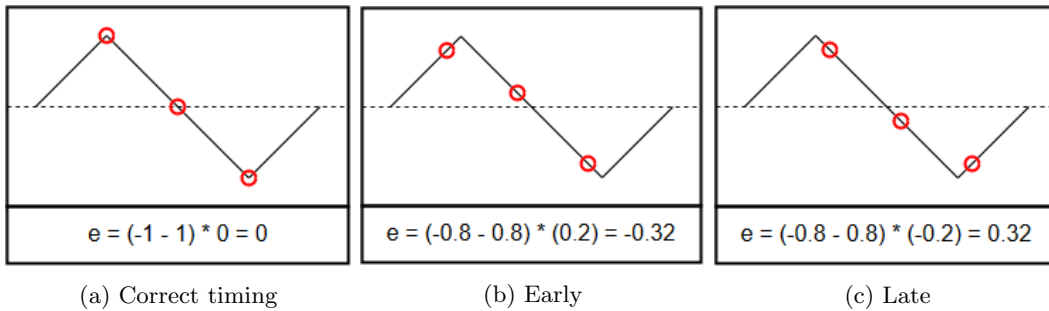


Figure 2.23: Gardner clock recovery

### 2.3.4 Loop Tuning

Based on the previously discussed characteristics and the specific requirements of the desired demodulator (high performance), the Gardner’s algorithm presents the best solution. This is because of the fact that this algorithm is highly insensitive to carrier offsets and variations which makes it robust in low SNR conditions.

To complete the demodulator implementation, one more tuning parameter must be analysed. The error generated by the clock and symbol timing recovery algorithm must be low-pass filtered to remove high frequency noise and then fed back into the sampler to advance or delay the sampling instant. The cut-off frequency of this low-pass filter will determine the responsiveness of the loop to clock drifts and its robustness against noise.

In most communication systems, a single master clock is used (in combination with PLLs) to derive the various clock frequency that are required. This ensures that all clock domains remain synchronized at all times. This means that the data and carrier clocks are derived from the same reference clock. As such the data clock drift is directly proportional to the Doppler shift and only scaled by the ratio of the RF frequency (144 MHz) and the data clock frequency (2.4 or 9.6 kHz). This means that the data clock only drifts by less than 0.1 Hz. The loop gain in this case is also derived by scaling down the loop gain of the carrier recovery loop by the same amount.

Figure 2.24 illustrates the received baseband signal after carrier synchronization. It can be seen that in this case, the sampler is also synchronized to the bit-stream and is sampling the signal at the optimum instant.

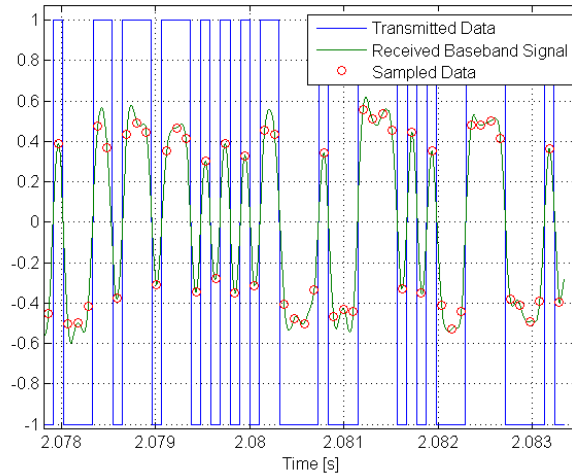


Figure 2.24: Received baseband and the sampling instant

### 2.3.5 Signal Interpolation

One of the key requirements of the new demodulator is the ability to demodulate high data-rate signals even at very low sampling rates. As a result of this requirement, an additional processing step is added to the clock and data recovery process to improve the results. To be able to fully appreciate the need for this additional step, it is best to first analyse the problem.

Traditionally, most hardware-based receivers use the error signal generated by the clock and data recovery algorithm to advance or retard the sampling instant by adjusting the sampling clock phase. Since SDRs are decoupled from the sampling hardware, they are generally incapable of directly controlling the sampling clock phase. As such, most SDR implementations simply use the closest sample (to the ideal sampling instant as indicated by the clock and data recovery algorithm) for the decision criteria. This approach works relatively well for very high sampling-rates or low data-rates. However, as this ratio becomes smaller, the nearest sample can no longer accurately represent the ideal sample.

$$\text{Samples per symbol} = \frac{\text{Sample Rate}}{\text{Data Rate}} \quad (2.47)$$

Equation 2.47 is used to calculate the number of samples available per symbol. It can be seen that for a sampling rate of 44100 Hz, 2400 and 9600 bps signals contain 18.4 and 4.6 samples per symbol respectively. Figure 2.25 depicts a sequence of 6 transmitted symbols at two different data-rates. The green line represents the received baseband signal after matched filtering and the red circles indicate two consecutive samples. Most SDR demodulators (including DUDe) select one of these two points (based on the fractional part of the error signal) as the sampled data. This figure clearly shows that in the case of a 9600 bps data-rate, the sampled point can differ by as much as 40% from the ideal sample point. This will negatively impact the BER. In comparison, a 2400 bps signal can only differ by as much as 10%.

To solve this problem, interpolation can be used. The simplest form of interpolation is linear interpolation. Linear interpolation is performed by assuming that a straight line joins each waveform sample. This is a very simple, but naive method that provides limited results. The blue graph in Figure 2.26 shows the interpolated signal between 4 samples points of a single symbol. The vertical black line indicates the ideal sampling instant at precisely the center of the symbol period. As it can

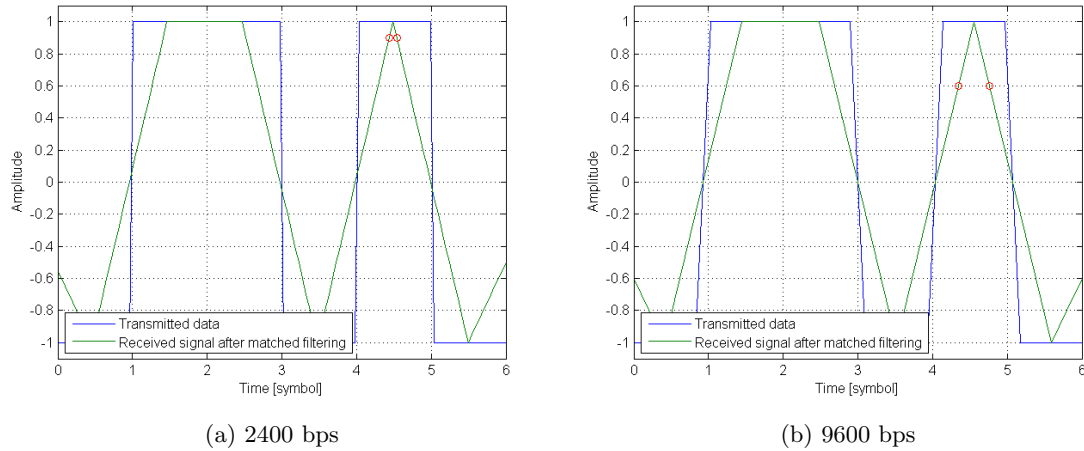


Figure 2.25: Two consecutive sample points for various data-rates

be seen, even using linear interpolation, there is hardly any observable improvement over choosing the nearest sample point.

A superior approach in this case would be triangular window interpolation. This technique can essentially be viewed as convolution of an up-sampled triangular window with the sampled data. The triangular window is formed by generating a triangle that has a height of 1.0 and a width that is twice the sample period. As the window slides to the right, interpolated points are found by calculating the sum of the values of the window multiplied by the value of actual samples at the times where the window and the sample points intersect. The ideal interpolated sample is located at the apex of the window (center point). Figure 2.26 clearly illustrates that when using triangular window interpolation, the sampled point only deviates from the ideal sample by less than 5% for a 9600 bps signal. This is an improvement, even over the 2400 bps data-rate.

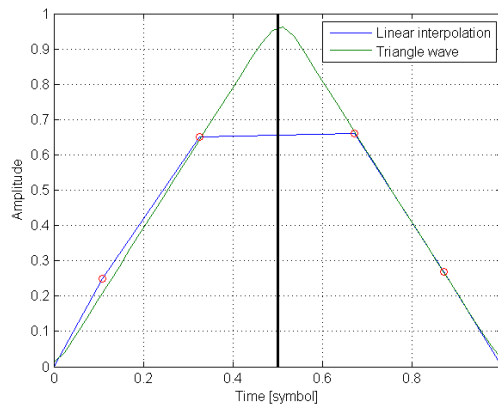


Figure 2.26: Two interpolation techniques

## 2.4 Packet Synchronization

The carrier and clock synchronization algorithms, as described above, are vital for the operation of the BPSK demodulator. Another commonly used (but not necessary) technique for improving the performance of the receiver under certain conditions is packet synchronization, sometimes referred

to as frame synchronization. In telecommunication, packet synchronization or framing is the process by which, while receiving a stream of framed data, incoming packet alignment is identified. This step is generally uncoupled from the demodulator as it is independent of the modulation scheme used in the transmission channel.

Packet synchronization is only used when data is sent intermittently as opposed to in a solid stream. In the case of the Delfi-n3Xt, a data packet is sent once every second. Since each packet has a length of 1792 bits, the transmission only lasts for approximately 0.75 seconds and is thus not continuous. The most widely used method for providing frame synchronization in a binary signalling scheme is to insert a fixed binary pattern or packet header periodically into the data stream. In the case of the Delfi-n3Xt and DelFFi satellites, the AX.25 packet header (01111110) is used. On the assumption that clock and symbol synchronization has already been obtained, the receiver can mark the start of each packets (achieve packet synchronization) by locating the position of the packet header in the received data stream.

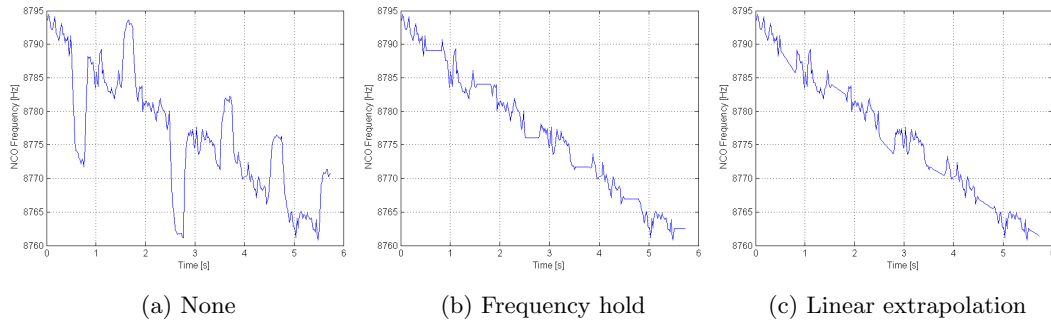


Figure 2.27: Carrier tracking performance based on various packet synchronization techniques

The benefits of packet synchronization is evident by looking at Figure 2.27a. The graph is aligned to the start of the packet ( $T = 0$  corresponds to the start of the transmission of the first packet) and shows the frequency of the NCO during the reception of six consecutive packets. After the complete transmission of a packet, the transmitter stops transmitting any information until the next packet. During this period, the frequency of the NCO can significantly drift due to noise. The demodulator is essentially locked onto white Gaussian noise instead of the actual signal.

Figure 2.27a illustrates that frequency drifts of upto 20 Hz can occur in the short time between two consecutive packets. Without frame synchronzation, the integral and proportional gains of the Costas loop (as described in section 2.2) must be selected in such a way to allow the NCO to lock onto the signal again after the observed frequency drift. However, with prior knowledge of the packet transmission interval, the frequency of the NCO can be locked to prevent its drift. The frequency of the NCO is then unlocked prior to the reception of the incoming packet and frequency control is given back to the Costas loop. Figure 2.27b illustrates the effectiveness of this technique at eliminating the frequency drift.

The general downward slope of the NCO frequency observed in these figures, is caused by the Doppler shift. As the time interval between two consecutive packets increases, the difference between the starting frequency of the packets can become significant. In this case, simply locking the frequency of the NCO may not be sufficient. Linear extrapolation of the frequency, based on the measured Doppler shift can improve the performance under these conditions. Figure 2.27c shows the NCO frequency response using this implementation. In the case of DelFFi and Delfi-n3Xt, the packet interval of 1 second is small enough that frequency extrapolation is not necessary.

## 2.5 Packet Quality and Meta-Data Collection

Aside from improving the performance of the demodulator, a number of new features are added to the new telemetry client. These features are mainly intended for the university researchers as well as analysts and are of little use to most radio amateurs. The first feature is providing the capability to detect and collect corrupted packets for further analysis. As mentioned in the previous section, each frame is confined between two AX.25 frame headers. Furthermore, a 16-bit Cyclic Redundancy Check (CRC) is appended to the packets to detect any bit-errors.

As with most telemetry clients, DUDe simply discards corrupted packets that fail the CRC. However, since its unknown how many bit-errors are present in the packet, useful information can still be extracted from these packets. The new telemetry client implements a simple threshold for designating the incoming decoded bit-stream as a potential packet. Any packet containing correct frame header and footer as well as the correct packet length is marked as a potential packet. However, the rate of false positives (marking random noise as a potential packet) would be too high under this criteria. Hence, the packet quality is measured and recorded for all potential packets.

The packet quality is measured based on the number of bit-errors in a known bit-sequence that repeats in every packet. The known bit-sequence is 8 bytes long and identifies the transmitter (Delfi-n3Xt) and recipient (Delfi ground station). The packet quality is calculated according to:

$$Q_{packet} = \frac{64 - n_{error} + n_{CRC}}{65} \quad (2.48)$$

In Equation 2.48,  $Q_{packet}$  represents the packet quality and is a number between 0 and 1.  $n_{error}$  is the number of bit-errors detected in the 64 bit long sequence. Finally,  $n_{CRC}$  is an integer that equals 0 or 1 when the CRC has failed or passed. Thus, when a correct packet arrives,  $n_{error} = 0$  and  $n_{CRC} = 1$  and the packet quality becomes 1. The packet quality decreases as more and more bit-errors are detected. Note that the above equation is designed so that when the CRC has failed (even if no bit-errors are detected in the 64 bit sequence), the packet quality cannot reach 1. By providing a measure for the packet quality, instead of a more straightforward packet/potential-packet/no-packet classification, flexibility is granted to the researchers to filter the collected telemetry data based on their particular requirements.

The new telemetry client is also capable of collecting various meta-data for each received packet. For instance Measured SNR and Doppler shift at the time of packet reception could be used for gathering statistical data on the performance of the demodulator. This information could also be potentially used for various other scientific goals.

# Chapter 3

## Results

With the design, implementation and tuning of the demodulator now complete, its performance can now be characterized. As described in Section 2.1, a MATLAB script was developed to produce a BPSK modulated signal and simulate the effects of the AWGN channel. Additionally, section 2.2 described a method for simulating the Doppler shift of the signal using the orbital parameters of the satellite. The resulting signal is then sampled at a rate of 44100 Hz which corresponds to the sampling rate of most PC sound cards which is expected to be used in the final system.

### 3.1 Initial Signal Acquisition Performance

Before the sampled BPSK signal can be demodulated, a precise phase and frequency coherent replica of the carrier signal must be generated. This process is referred to as initial signal acquisition and is described in Section 2.2. As stated in that section, a two step approach was taken for carrier recovery. Meaning that two separate sets of tuning parameters are used during the signal acquisition phase and signal tracking. For the initial signal acquisition analysis performed in this section, the former tuning parameters are used.

Figure 3.1 illustrates the NCO frequency over time during the signal acquisition phase. The SNR was reduced after each test to find the lowest possible SNR, where reliable acquisition was achievable. An initial offset of 100 Hz was used for all cases. This is roughly the expected initial frequency offset when Doppler estimation is used. As evident from this figure, consistent signal acquisition was possible at SNRs as low as -2 dB. At a SNR of -3 dB and below, successful signal acquisition was possible given enough time. From the figure, it may appear that signal demodulation would be impossible due to the large variations in the frequency (in the order of 10s of Hz). However, once the NCO frequency reaches the correct value, the demodulator can significantly lower the frequency and phase noise by switching to the second set of tuning parameters used for signal tracking.

In comparison, the DUDe demodulator is only capable of acquiring signals with a SNR of 1 dB or higher. This is the reason that the BER figures depicted in the following section start at this value. From these results it can be concluded that the new demodulator displays an improvement of 3 to 4 dB over the previous demodulator when it comes to initial signal acquisition. However, it is known that even using an ideal demodulator, the BER is simply too high for reliable communications under these SNR conditions. So one might argue that improving the initial signal acquisition performance is wasted effort. The counter argument is that using various modern Error Correction Code (ECC) techniques, it is possible to realize reliable transmission links within a fraction of dB above Shannon's limit. However, no amount of error correction can improve the link quality if signal acquisition hasn't occurred yet. The benefits of ECC are explained in more detail in Chapter 5.

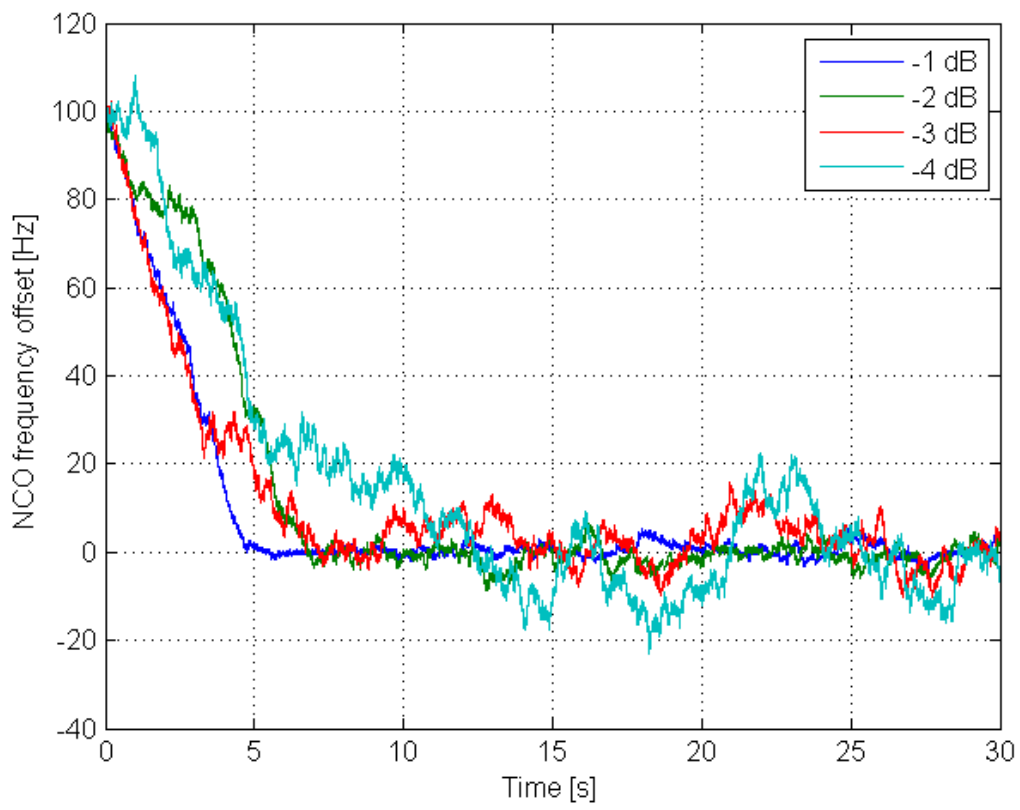


Figure 3.1: Initial signal acquisition under low SNR conditions

## 3.2 Bit-Error Rate Analysis

Perhaps the most important performance characteristics of a demodulator is the BER. In this section the BER analysis is presented. In order to accomplish this, the sampled signal replica is passed to the newly developed demodulator as well as the DUDe demodulator for comparison. It is important to mention that, random number generators are used throughout the script for simulating the random behaviour of the noise as well as generating a random sequence of bits for transmission.

According to the theory (Figure 3.2), the BER at a SNR of 10 dB is approximately  $4 \cdot 10^{-6}$ . This means, to have a 50% chance of observing even a single bit error at such a high SNR,  $1.3 \cdot 10^5$  bits must be transmitted. However, to be able to measure the BER with some degree of confidence, the transmitted sequence must be orders of magnitude longer than the previously stated value. At a data-rate of 2400 bps, such a transmission would take hours to complete if processed in real-time. Furthermore, the storage requirements of the necessary variables would be in the Giga-bytes range which severely reduces the system performance (due to caching to disk). Hence, even though producing accurate BER measures at high SNRs is difficult, by providing the same set of randomly generated signals to both demodulators, an accurate comparison between them can still be obtained.

Figure 3.2 illustrates the resulting BER of the new demodulator in comparison to the theoretical BER and what was previously achievable using the DUDe demodulator. In this section, it is assumed that signal acquisition has already occurred and thus the tuning parameters for signal tracking are used for obtaining the BER. Furthermore, the BER was measured from a continuous stream of bits therefore eliminating the effects of packet synchronization. This should provide the closest comparison to the theoretical BER achievable using BPSK modulation.

At first glance, Figure 3.2 shows that the BER performance of the developed demodulator at a data-rate of 2400 bps, is only a fraction of dB lower than the theoretically achievable value. It is important to note that the theoretical BER corresponds to an ideal receiver. In an ideal receiver, the receiver has perfect knowledge of the carrier and data clock (both phase and frequency). In this case, only the effects of Gaussian noise contribute to the BER. Hence for a non-ideal demodulator to achieve a BER performance approaching that of a coherent demodulator is impressive.

Remember that in a simulation, a properly designed ideal BPSK demodulator should achieve a BER that matches the theory precisely. After all the theoretical BER is calculated using the Gaussian probability distribution function which is also used to generate the simulated noise. Hence, to verify that the performance of the new demodulator does indeed match that of an ideal demodulator, the exact carrier and data clock signals can be directly fed into the mixer, thus effectively bypassing the Costas and Gardner loops. This essentially turns the developed demodulator into a ideal demodulator. Figure 3.3 illustrates that the BER performance of the new demodulator, when operating in this mode, is essentially equal to the predicted value. The almost imperceptible difference (in the order of 1%) is attributed to numerical precision used in the simulation as well as a finite test sequence.

Having proven that the new demodulator is performing as predicted, it can be concluded that the small difference in BER, observed in Figure 3.2, is the result of an imperfect replication of the carrier signal using the noisy data and proves that the demodulator is performing nearly as well as an ideal demodulator.

An interesting observation can be made by looking at the ratio of the measured BER to the theoretical BER. This ratio is illustrated in Figure 3.4. It can be seen that for a data-rate of 2400 bps, the BER is approximately 10% higher than the theoretical value for SNRs lower than 6 dB. The difference grows to a factor of two (twice as many bit errors) at higher SNRs. This phenomena is another indication that the difference in BER performance is caused by an imperfect knowledge of the carrier signal. Since at lower SNRs, the contribution of Gaussian noise is far greater than carrier phase noise and offset, the resulting BER is fundamentally determined by the effects of Gaussian noise. At higher SNRs where the Gaussian noise is sufficiently low, the effects of carrier phase noise

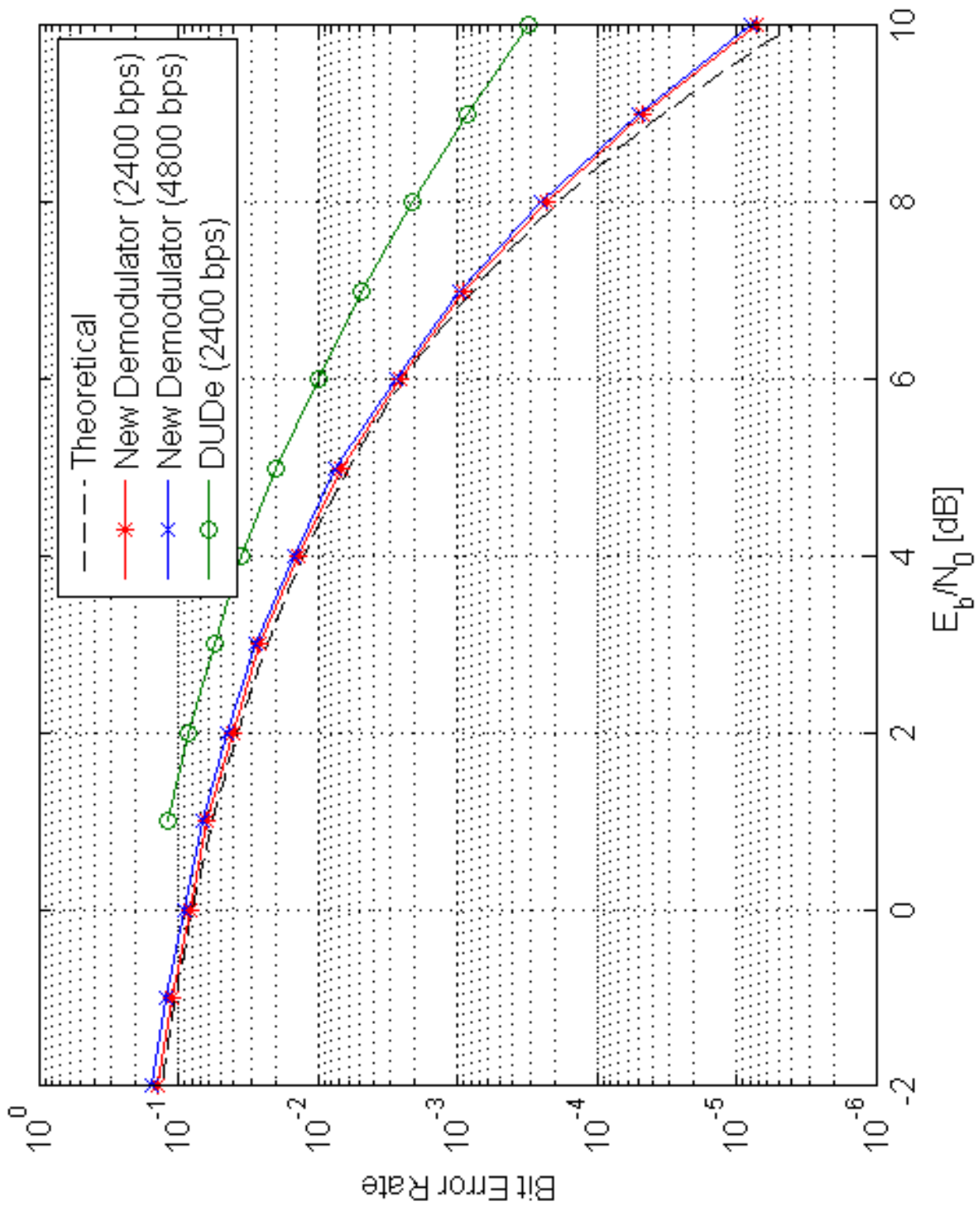


Figure 3.2: BER of the new demodulator

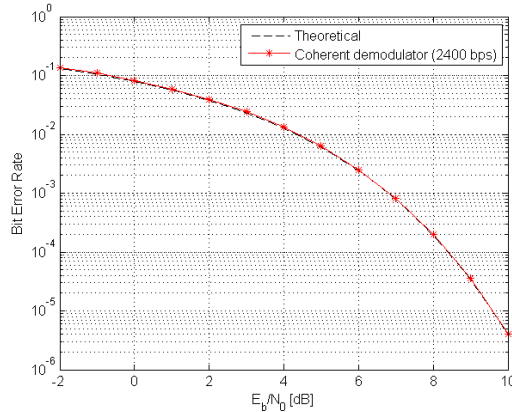


Figure 3.3: BER of the new demodulator when operating in coherent mode

and offset become more apparent and the primary contributor to the resulting BER. The resulting BER of the new demodulator at a data-rate of 4800 bps remains nearly identical to the BER performance achieved with a data-rate of 2400.

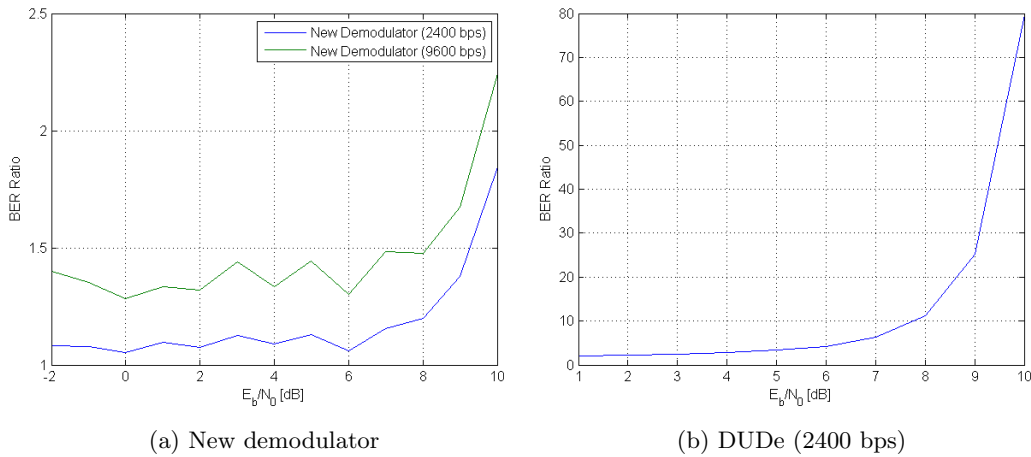


Figure 3.4: Ratio of measured BER to the theoretical BER

However, when increasing the data-rate to 9600 bps (as required for the DelFFi mission), the resulting BER performance is slightly lower and can be found in Figure 3.5. This figure illustrates the BER of the demodulator for both cases where no interpolation and a triangular waveform interpolation is used. As stated in Equation 2.3, the required bandwidth for a BPSK modulated signal is twice the data-rate. The selected sampling rate of 44100 Hz is just above the Nyquist frequency of the signal at 38400 Hz. Since the sampling rate is so close to the Nyquist frequency, one expects the BER performance to have slightly degraded with respect to the 2400 and 4800 bps data-rates.

However, it can be seen from Figure 3.5 that the negative impact of the higher data-rate on the BER is largely mitigated by the use of sample interpolation. In fact using this technique with a 9600 bps data-rate, acceptable BER performance was achieved with sampling rate as low as the Nyquist frequency (38400 Hz). Furthermore, it can be observed that under all data-rate and SNRs, the new demodulator out performs the previously used demodulator. The difference in performance can be upto 40 times with higher SNRs. The BER performance at these SNRs (between 8 to 10 dB) is extremely important for the robustness of the telemetry link of the Delfi-n3Xt and DelFFi satellites, more so than the lower SNRs. The reason for this is explained in the following section.

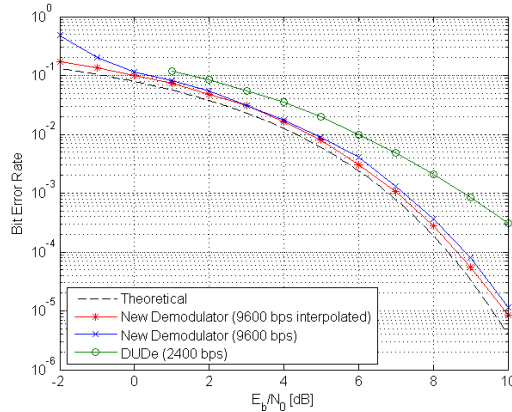


Figure 3.5: BER of the new demodulator when operating at a data-rate of 9600 bps

### 3.3 Packet Reception Rate Analysis

Even though the BER analysis, using simulated signals, performed in the previous section is a crucial step in characterizing the performance of the developed demodulator, it is perhaps more essential to understand the behaviour of the demodulator under real-world conditions. Of course the best method for testing the demodulator under real-world conditions is to utilize actual signals transmitted by the satellites. In this section, the pre-recorded signals of the Delfi-n3Xt satellite are used to characterize the behaviour and measure the performance of the new demodulator.

One of the other benefits of using actual signals, is that the accuracy and validity of the previous simulations can be verified. For instance, Figure 3.6a depicts the Doppler shift of the telemetry signal of Delfi-n3Xt during its pass on 12th of January 2014. This data was obtained by recording the NCO frequency of the demodulator during signal tracking. From this figure, it can be seen that the simulated Doppler shift using the orbital parameters of Delfi-n3Xt, closely matches the measured Doppler shift. However, larger maximum Doppler shift was observed in the recorded data. The small discrepancy between the two curves could be explained by the inaccuracies of the TLE sets.

It is important to note that the rate of change of the Doppler shift was the determining factor in selecting the loop parameters. This is plotted in Figure 3.6b and confirms that the simulated results match the experimentally obtained data. This means that the loop tuning parameters (based on the simulations) remain valid and proves that a simplified orbital model is sufficient for this task.

To be able to accurately characterise the performance of the demodulator under a wide range of real-world conditions, 5 Delfi-n3Xt passes were selected. These particular passes were chosen based on the fact that raw signal recordings were available. The orbital parameters for these passes can be found in Table 3.1. As it can be seen, the maximum elevation angles were purposefully chosen to range from very high to very low. This was done to observe the behaviour of the demodulator under various SNR conditions.

The distance between the satellite and the ground station (slant range) is also a very important measure for estimating the SNR. As such, the slant range (at closest approach) is also included in the table for each pass. An interesting observation is that the slant range for pass 2 is slightly smaller compared to pass 1 even though the elevation angle is lower. Finally, the pass duration can also be found in Table 3.1. The pass duration is calculated as the time between the rise of the satellite above  $5^\circ$  elevation, until its fall below  $5^\circ$  elevation. From this table it can be concluded that the pass duration is inversely proportional to the maximum elevation angle as to be expected. Since the transmitting antennas on the Delfi-n3Xt are omni-directional, the pass duration and contact time

### 3.3. PACKET RECEPTION RATE ANALYSIS

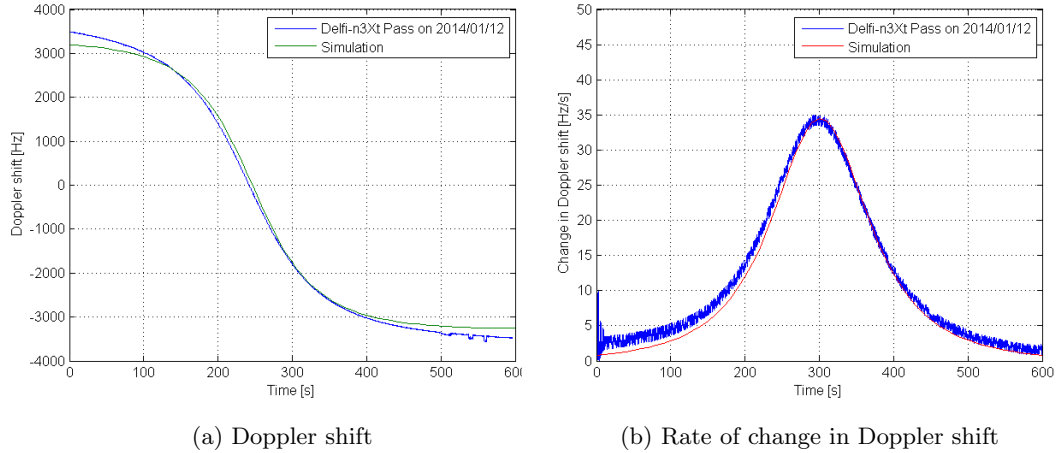


Figure 3.6: Simulated Doppler shift compared to observation

are equivalent and will be used interchangeably in this section.

The choice of  $5^\circ$  elevation angle as the start and end point of the contact time is not arbitrary. Direct Line-Of-Sight (LOS) contact becomes problematic at lower elevation angles due to terrestrial obstructions. Perhaps more importantly, performance impairments occur on satellite communication links because of severe tropospheric fading effects and ground reflection interference when the elevation angle of the satellite is very low. Experimental data shows that deep fading of satellite communications signals because of severe tropospheric absorption can be as much as 27 dB. As such, an elevation angle higher than  $5^\circ$  is generally required for reliable communications.

Pass #	Date	Elevation [°]	Azimuth [°]	Range [km]	Pass duration [s]
1	2014-01-17	84.9	107.3	738	717
2	2014-01-02	69.2	287.4	702	660
3	2014-01-01	54.8	100.6	786	654
4	2014-01-03	35.4	96.9	1060	635
5	2014-01-20	14.6	306.2	1944	514

Table 3.1: Orbital conditions of 5 Delfi-n3Xt passes

After passing the sampled RF data for these passes to the demodulator, a number of key results were recorded. Traditionally, a BER analysis is performed using experimental data to characterize the performance of a demodulator. In this case however, as the transmitted bit sequence is unknown, it is impossible to directly measure the BER. To circumvent this issue a packet reception rate analysis was performed.

The Delfi-n3Xt transmits a 1792 bit long packet every second. These packets contain a 16-bit CRC checksum used for detecting bit errors. The error detection rate for a 16-bit CRC algorithm is given by Equation 3.1.

$$\text{Error detection rate} = \frac{2^{16} - 1}{2^{16}} = 99.9999847\% \quad (3.1)$$

Since, the probability of a false positive (declaring a faulty packet as good) is only 1 in 65536, the probability of a false positive during even the longest pass (pass 1) becomes:

### 3.3. PACKET RECEPTION RATE ANALYSIS

---

$$\frac{1}{2^{16}} * 717 = 1.094\% \quad (3.2)$$

As such from this point forward, it is assumed that when a packet is declared correct (using the CRC checksum) it contains no bit errors.

Table 3.2 lists the number of correctly received packets (by the new demodulator) for each of the 5 selected passes. Each transmitted packet contains a frame counter represented by an integer that counts the number of transmitted packets. For each pass, the frame counter for the first and last received packets are recorded in the columns "First packet received" and "Last packet received" respectively. By looking at the pass dates (in Table 3.1) and the frame counters, it can be seen the frame counter does indeed increase over time from pass 3 to pass 2 and eventually pass 4. Keen observers will realize that the frame counter has reduced in value for passes 1 and 5, even though they occurred several days later. This is caused by an integer overflow of the frame counter variable within the satellite's On-Board Computer (OBC).

Unlike the previous demodulator DUDe, the new demodulator is capable of recording corrupted packets for further analysis and potential data extraction. Corrupted packets can be packets that contain atleast a single bit error or even sampled random noise that passed the acceptance criteria. This capability is described in section 2.5. To be able to provide direct comparison to the DUDe demodulator the number of corrupted packets are not used in the following analysis.

The column "Transmitted packets" contains the difference between the frame counters of the last and first received packets and represent the number of packets that were transmitted between the first and last successful contact. The last column in Table 3.2 denotes the ratio of correct packets received to the total number of transmitted packets. As a comparison, Table 3.3 contains the same information (except for number of corrupted packets received) for the DUDe demodulator.

Pass #	First packet received	Last packet received	Correct packets received	Corrupted packets received	Transmitted packets	Percentage received packets
1	18078	18809	612	78	731	83.7%
2	17437	18174	631	72	737	85.6%
3	9140	9851	535	94	711	75.2%
4	34742	35363	479	104	621	77.1%
5	8821	9169	270	118	348	77.6%

Table 3.2: Packet statistics using the new demodulator

The difference in performance when comparing the two demodulators is very clear when looking at the recorded data. Firstly, the number of correctly received packets is higher using the new demodulator for all 5 passes. In fact at low SNR conditions that occurs at low elevation angles (as experienced during pass 5), the new demodulator receives 6 times as many packets. The ratio shrinks to a factor of 2 for the higher elevation angle passes. This means that even in the worst-case scenario, the new demodulator can more than double the amount of gathered telemetry for the current and future CubeSat missions.

Furthermore, the first packet reception occurs sooner using the new demodulator as compared to DUDe for all passes. For instance, during pass 2, 3 and 4, the new demodulator received the first packet more than 2 minutes earlier. Similarly, using the new demodulator, the last packet reception occurred nearly 40 seconds after the DUDe demodulator stopped receiving any packets. During the first and final few minutes of each pass, the satellite is still at fairly low elevation angles and thus BER performance becomes very important for successful packet reception. An interesting

Pass #	First packet received	Last packet received	Correct packets received	Transmitted packets	Percentage received packets
1	18123	18748	343	625	54.9%
2	17578	18125	317	547	58.0%
3	9285	9781	311	496	62.7%
4	34880	35335	192	455	42.2%
5	8867	9151	45	284	15.8%

Table 3.3: Packet statistics using the DUDe demodulator

observation can be made for pass 1 by comparing the number of transmitted packets with the pass duration in Tables 3.2 and 3.1 respectively. Since, one packet is transmitted every second, one expects to receive a maximum number of 717 packets during pass 1. However, the number of packets transmitted between the first and last point of contact was 731. This shows that the new demodulator is occasionally capable of receiving packets at elevation angles lower than  $5^\circ$ .

Equation 3.3 can be used to understand the relationship between the BER and probability of successful packet reception. This probability is given by the probability of successful transmission of a single bit (which equals 1 minus BER), raised to the power of total number of bits within a single packet.

$$P_{\text{successful packet reception}} = (1 - BER)^{\text{Packet length}} = (1 - BER)^{1792} \quad (3.3)$$

Figure 3.7 illustrates the probability of successful packet reception for an ideal demodulator, the newly developed demodulator and DUDe. This figure shows that even when using a coherent (ideal) demodulator, successful packet reception is virtually impossible at a SNR below 6 dB (assuming 1792 bit packets). To have a 50% chance of receiving a packet, a SNR of approximately 7.5 dB is required. The figure also shows that the performance of the new demodulator is very close to theoretical curve. Of course this is to be expected since it was already shown that the BER performance of the demodulator approaches that of an ideal demodulator. The performance of the DUDe demodulator is however significantly lower. It is important to note that the curves for the both demodulators were interpolated between the actual BER measurements.

The measured SNR as a function of time, for the selected 5 passes, are plotted in Figure 3.8. The vertical blue and red lines indicate the first and last contact when using the new demodulator and DUDe, respectively. The measured SNR curves are not smooth curves and have various random features that make analysis difficult. The irregular shapes of the SNR plots are caused by various effects such as interference and antenna tracking errors. For instance, the sharp falls at the center of the SNR plots observed during passes 1, 2 and 5, are caused by the antenna tracking mechanism. When the satellite passes directly over the ground station, the antenna must rotate  $180^\circ$  which temporarily disrupts the LOS and reduces the SNR.

However, the overall shape of the curves are consistent. The SNR at the start of the pass is small, due to the low elevation angle and large slant range. The SNR rises to a maximum value at the point of closest approach and then falls back down. Following the blue vertical lines, showing the first and last point of contact of the new demodulator, one can observed that the first and last packets are consistently received when the SNR reaches approximately 7 dB. According to Figure 3.7, there should be a 20% chance of correctly receiving a packet at this SNR. The red lines, indicating the first and last contact point for the DUDe demodulator, intersect the SNR curve at approximately

3.3. PACKET RECEPTION RATE ANALYSIS

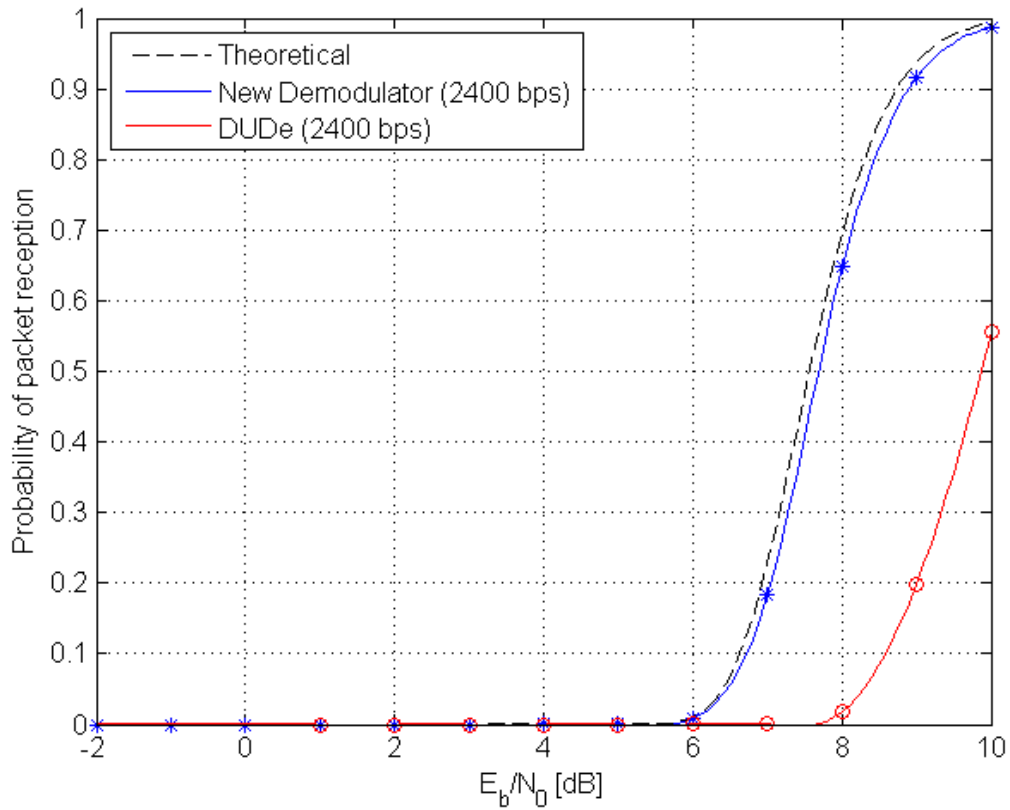
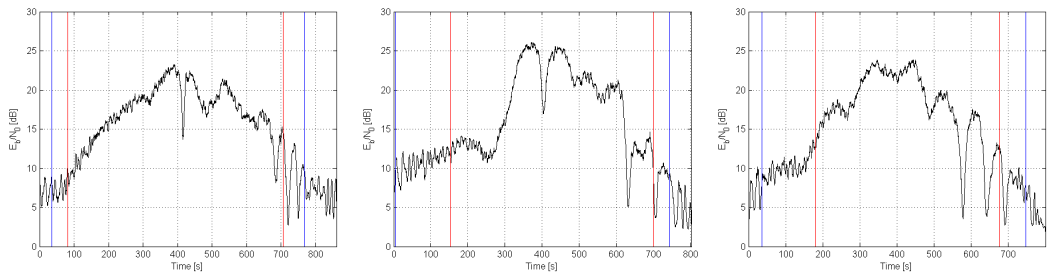
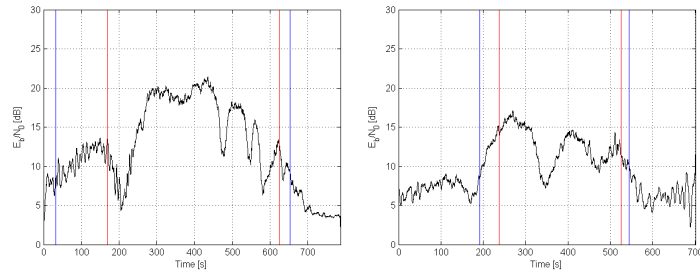


Figure 3.7: Probability of successful packet reception



(a) Measured SNR during pass 1 (b) Measured SNR during pass 2 (c) Measured SNR during pass 3



(d) Measured SNR during pass 4 (e) Measured SNR during pass 5

Figure 3.8: Measured SNR during the selected Delfi-n3Xt passes

### 3.3. PACKET RECEPTION RATE ANALYSIS

---

the 12 dB threshold. This shows that the new demodulator can start receiving packets at a SNR of 5 dB below what is required by the previous demodulator.

In the case of the new demodulator, it was observed that the first and last packets were received at a SNR that provided a 20% chance of successful reception. The DUDe demodulator has a 20% chance of successful reception at a SNR of 9 dB. However, Figure 3.8 shows that a SNR of 12 dB was required. This means that the DUDe demodulator performs worse under real-world conditions than what is predicted by the BER analysis. This is contributed to the effects that are not considered in the BER analysis, such as packet synchronization and non-Gaussian noise sources and channel effects.

Figure 3.9 illustrates the measured SNR during pass 1. The blue background color of the plot depicts the areas where packets were successfully received. As it can be seen from this figure, virtually every time the SNR peaks above 10 dB, packets are received. Remember that Figure 3.7 shows that probability of successful packet reception is approximately 98.7% at 10 dB. During pass 1, 618 packets were transmitted when the measured SNR was above 10 dB and only 16 of these packets were not successfully received. This means that 97% of the packets were successfully received when the SNR was 10 dB or higher. This confirms that the performance of the new demodulator under real-world conditions is as predicted by the simulations and the BER analysis.

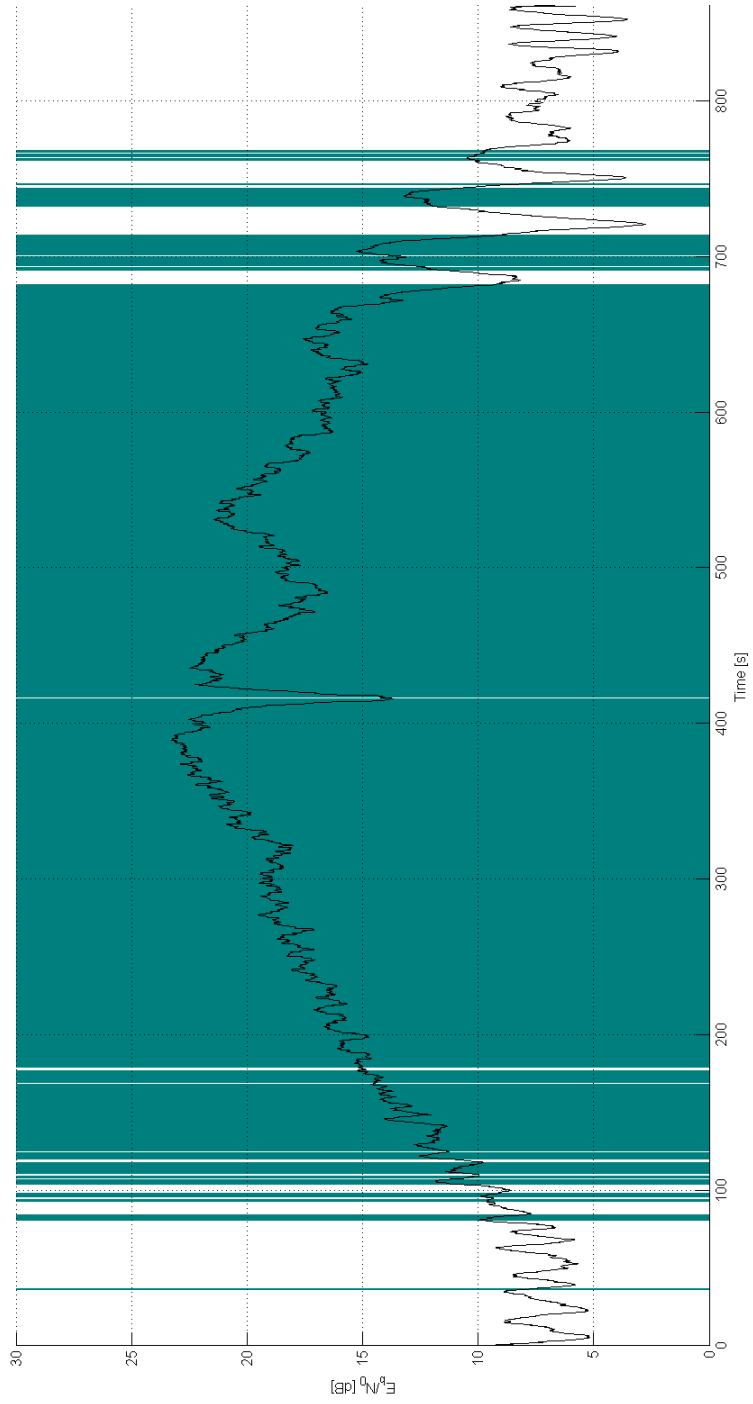


Figure 3.9: Received packets vs. SNR (pass 1)

### 3.4 Telemetry Client

As stated in Chapter 1, one of the more practical goals of this research is to produce the software tools to facilitate telemetry reception for the upcoming DelFFi mission. Among other improvements, the new telemetry client will be using the developed BPSK demodulator to achieve greater performance. The Delft Universal Data extractor (DUDE) is the software fulfilling the task of telemetry data client for the current missions. It is designed to be used by the ground control station operators as well as radio amateurs for demodulating, processing of raw data and providing a graphical representation of the processed data. The collected packets are then sent to a central database for further processing and archival. This system allows telemetry data to be received from various amateur and professional ground stations all over the world thus effectively increasing the per orbit downlink budget. Due to the success of the design, the same system is replicated for the new telemetry client. The hierarchy of this system is illustrated in Figure 3.10.

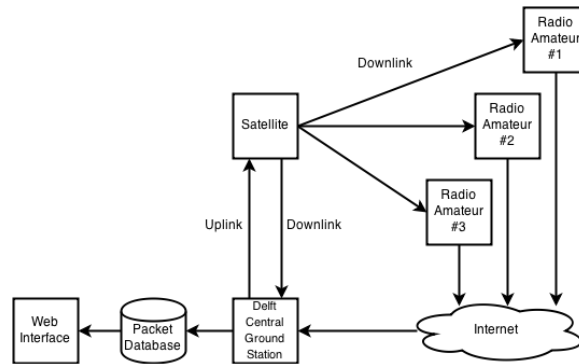


Figure 3.10: Hierarchical view of the telemetry system

#### 3.4.1 Software Architecture

The section provides a brief overview of the software architecture of the newly developed telemetry client. Although, designed specifically for the DelFFi mission, flexibility and modularity were key criteria when designing the telemetry client. This due to the fact that the Delfi CubeSat roadmap is still variable and modulation and data-rate requirements of future missions are prone to change depending on the situation. As such, four primary modules were designed to operate completely independently of each other. These modules are illustrated in Figure 3.11. As long as the programmer adheres to the specified input/output interfaces, new modules can be developed which can easily enhance or replace current modules in order to significantly change the behaviour of the telemetry client.

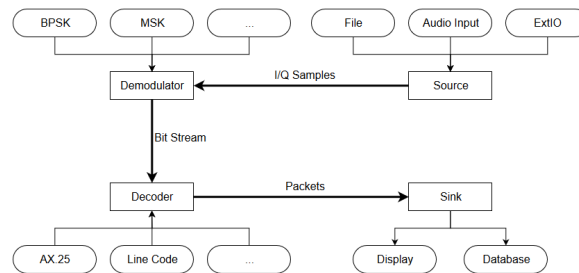


Figure 3.11: Software architecture of the telemetry client

#### Source

Following the signal path, the first module is the source. This module is responsible for providing scaled in-phase and quadrature samples of the RF spectrum to the following modules. According to the requirements of the project, 3 different source modules were implemented. A file source is used to read and process pre-recorded samples from standardized WAV files. The current ground station is configured to record the raw RF samples of Delfi-C3 and Delfi-n3Xt for every pass. These recordings present an incredible source of information and knowledge for both tuning as well as testing the new BPSK demodulator.

The second source is the analogue audio input port of the sound card found on most Personal Computers (PC) across the world. The audio input channels of these sound cards are often equipped with 24 bit ADCs with sample-rates of upto 192 kHz and currently represents the most easily accessible form of RF sampling to radio amateurs. To enlist the help of the radio amateurs, it was vital to provide the capability to utilize this source within the new telemetry client. However, as dedicated SDR front-ends (with far superior performance) are becoming cheaper and easier to acquire, the need for this analogue audio input source is diminishing. Fortunately, the modular nature of the telemetry client means that any module that becomes outdated or redundant can be simply removed without affecting the remaining modules. The stereo channel capability of sound-cards enables the sampling of both in-phase and quadrature signals using the left and right audio bands.

The final source module implements an interface to the External IO (ExtIO) standard. Historically, most SDR software were initially designed to interface to the sound card and without any provision for controlling external hardware. As the data-rate requirements increased, so did the necessity for higher sampling rates. To support such high sampling rates, other input sources, most notably the USB port, were employed. Of course it would have been quite impractical to code and to maintain a different version of the telemetry client for each and every different hardware to be supported. The solution devised was that of placing an intermediate layer of code between the telemetry client and the hardware. This intermediate layer is known as ExtIO and has become the de-facto standard for all commercial SDR hardware. The incorporation of this source within the new telemetry client has enabled access to hundreds of professional SDR equipment.

#### Demodulator

The second module is the demodulator. The task of this module is to use the I/Q sample pairs produced by the source module to demodulate the signal and produce a stream of demodulated binary bits for the following modules. Due to the standardized interfaces to and from this module, it can easily be replaced by other demodulators (for various modulation schemes) without altering the other modules. Currently, the only demodulator module developed for the telemetry client is the new BPSK demodulator. For implementing a BPSK demodulator, various customizable building blocks were also implemented. These blocks include: IIR and FIR filters, NCOs, PID controllers, etc. These blocks can also be re-used to implement other demodulators (for instance QPSK, (G)MSK, etc.) within a much shorter development period.

#### Decoder

The bit stream produced by the demodulator must now be decoded by the decoder module. The decoding process is highly application specific. For instance, the combination of packet length, packet header, packet structure, bit-stuffing, checksum algorithm and line coding is unique for most satellites. As such it is very difficult to implement a generalized decoder without having to include tens if not hundreds of settings and parameters. Hence, the best solution was deemed to make the decoding process satellite specific. The decoder module is then tasked with decoding the bit stream

using knowledge of the above parameters. The output of this module is completed and verified (through checksum) packets.

#### **Sink**

The sink module is the final destination along the signal path. This module receives the decoded packets from the decoder module and uses it for various objectives. The first sink module is a Graphical User Interface (GUI) to view the packet data to the user. A graphical representation of the RF spectrum is also provided both in the form of a spectrum view as well as waterfall view. This GUI (as depicted in Figure 3.12) also enables the user to set the various parameters of all modules. The second sink module provides a secure and authenticated access to the ground station database, to upload decoded packets for archival and further analysis.

### 3.4. TELEMETRY CLIENT

The screenshot displays the DEXTER Telemetry Client interface, which is used for receiving and analyzing telemetry data. The interface is divided into several sections:

- Demodulator Settings:** Located at the top left, it includes fields for Modulation (BPSK), Search Mode (Manual), Data Rate (2400 bps), AGC K\_P (0.60), CDR K\_P (0.05), Costas K\_F (2.00), Costas K\_I (8.00), Packet Format (AX25), Line Code (NRZI), and Packet Length (1792 bits). The Demodulator Status is currently "Searching...".
- Source Settings:** Located at the bottom left, it shows the Source as "C:/Users/Ehan/Documents/MEGA/Thesis/Delft-m3xt", LO Frequency as "145868000.00 Hz", Sample Rate as "50000", Sample Size as "24", and Channels as "Channel 2 (I) | Channel 1 (Q)".
- Packet List:** A table in the center-left shows a list of received packets with columns for Packet #, Date and Time, and Raw Packet. The raw packet data is displayed in hexadecimal.
- Spectrum Plot:** On the right side, there is a "Waterfall" plot showing frequency over time and a "Spectrum" plot showing the current frequency spectrum. The spectrum plot has a peak at approximately 145868000 Hz.
- Source Control:** At the bottom right, there are playback controls including a play button, a stop button, a 2x zoom button, and a time display showing "00:09:52/00:44:04".

Figure 3.12: The newly developed telemetry client

### 3.4.2 Real-time Performance

As stated in Chapter 1, the primary objective of the new demodulator was to achieve the best performance excluding real-time constraints. This was done in order to obtain a reference figure for what is possible. Some of the steps taken to achieve this objective came at the cost of increased computational complexity. However, in order to meet the requirements of a functional telemetry client, real-time demodulation capability is highly sought after. If real-time demodulation is not possible, the telemetry client must record the raw RF signals for every pass and then play back the recorded files at slower speeds for demodulation. Although this technique can be used, it brings its own set of problems. Some of these challenges are disk utilization and record/play-back scheduling. As such, an effort was made to improve the performance of the telemetry client and reduce its resource consumption as much as possible. To this end an innovative approach was taken. To harness the multi-core architecture of today's processors, an event-based interface between the modules was developed.

The source module receives I/Q samples from its respective source and stores it in a local buffer. Once the buffer is full, it will signal the demodulator to process the samples stored in the buffer. Similarly, the demodulator module, stores the raw bit stream within a local buffer and signals the decoder every time this buffer is filled. Finally, the decoder module signals the remaining modules in the chain once a full packet is processed. Since every module is completely decoupled and only activates when enough data has been processed, the Operating System (OS) can automatically execute each module within its own thread. This ensures that computer resources are used as efficiently as possible.

Even though the performance of the demodulator is highly dependant on the underlying hardware and processor speed, some analysis was performed in order to assess the suitability of the new demodulator for real-time demodulation. Using a Core i7 dual-core mobile processor running at 2.6 GHz, the new telemetry client was able demodulate 2400 and 4800 bps signal in real-time when the sampling rate was 48000 Hz and lower. This means that the new demodulator can directly replace DUDe for the current missions even when real-time demodulation is required.

A 9600 bps could also be demodulated in real-time when sample interpolation (see Section 2.3) is disabled. This comes at the cost of reduce BER performance. Real-time demodulation could not be achieved when higher sampling rates were used. Utilizing more powerful desktop processors could potentially enable real-time demodulation under higher sample-rates. However, with further optimization of the implemented algorithms, the real-time demodulation envelope of this telemetry client can be further expanded to include higher sampling rates and features.

## Chapter 4

# Conclusions

The software-defined telemetry decoding software, Delft Universal Data Extractor (DUDe) has served the role of the BPSK demodulator for the university's previous CubeSat missions. This SDR approach was required to provide adaptability to future mission requirements and to reduce hardware requirements for radio amateurs that would form a distributed ground control station network. An analysis of the performance of this demodulator revealed that its performance is not optimum and lacking behind what is theoretically possible. For instance, it was shown that the BER of this demodulator is twice as high as the theoretical value at low SNRs. The BER became 75 times higher than the predicted value at a SNR of 10 dB. Comparing these results to the stated performance of hardware demodulators as well as other SDR demodulators found in the literature, one can see an alarming discrepancy. Furthermore, the telemetry requirements for the future CubeSat missions such as the upcoming DelFFi mission have become much more stringent and are beyond the capabilities of the current demodulator.

A literature study was conducted to find suitable alternative SDR solutions for satellite communications. The study showed that recent advances of the enabling technologies such as the DSPs, GPPs and FPGAs, have paved the way for traditional communications systems to be completely software defined. However, it also showed that the research is almost entirely focused on simplifying the design and improving the performance, cost, reliability and power consumption of SDRs for terrestrial applications, with little focus on satellite communications.

This gap in knowledge presented an opportunity to deliver significant contributions to the growing field of SDR communications, while simultaneously realizing the more practical goal of producing an improved telemetry client for the upcoming DelFFi mission. To close this gap, a research proposal was prepared. The aim of the research was to design and implement a high performance software-defined BPSK demodulator, specifically for satellite communications, that minimizes the BER when computation time is abundant. Particular attention was given to the BER as well as initial signal acquisition optimizations based on the mission and orbital parameters.

Among the various carrier recovery techniques, the Costas loop was selected based on its excellent noise immunity and fast loop settling times. Furthermore, Costas loops are particularly well suited to a software-defined implementation. Similarly, the Gardner's algorithm was determined to provide the highest performance for low to mid data-rate applications and was employed for the new demodulator. To differentiate the new demodulator from all the other terrestrial SDR BPSK demodulators and further improve the performance, a number of additional techniques were employed.

A new systematic method was derived to optimally tune the various demodulator parameters. The method relies on the generation of a simulated RF signal based on the orbital characteristics of the mission. The resulting tuning parameters performed well when using actual recorded RF signals. However improved performance was obtained when the parameters were manually tweaked. As such,

---

the produced tuning parameters (based on the orbital simulations) are best suited to be used as a good approximation of the optimum parameters.

The two-step variable gain approach, used during the initial signal acquisition and signal tracking phases, operated as intended and successfully reduced the blind and assisted acquisition times without sacrificing BER performance. The packet synchronization showed increased link reliability and packet reception rate in simulations. In comparison, no statistically significant improvements in the packet reception rate was observed when using real-world signals. This is largely due to the fact the packet interval of one second (as used by the Delfi-n3Xt) doesn't take full advantage of the benefits of packet synchronization. Lastly, it was shown that signal up-sampling (interpolation) can reduce the BER by half at a data-rate of 9600 bps, but has no effect at lower data-rates. This improvement came at the cost of increased computational complexity.

The results of the initial signal acquisition, BER and packet reception rate analysis shows that the combination of the above improvements and techniques has significantly improved the performance of the new demodulator as a whole. Using simulations it was shown that the new demodulator can reliably lock onto signals with a SNR as low as -3 dB, a 4 dB improvement over the previous demodulator. This can have important positive consequences if forward error-correcting techniques are used for future missions. Furthermore, it was shown that the BER of the newly developed demodulator approaches that of an ideal demodulator. The BER performance was measured to be within 1 dB of the theoretical value under all SNR conditions and data-rates. This is an improvement of 2 to 40 times (depending on the SNR) compared to the previous demodulator.

Recorded telemetry signals of the Delfi-n3Xt were used to verify the improved performance of the new demodulator observed using the simulations. It was shown that for all 5 studied passes, the new demodulator out-performed the previous implementation in all aspects. The first and last contact was made approximately a full minute sooner and later. In one case, successful packet reception occurred when the satellite was less than  $5^\circ$  above the horizon. Furthermore, the number of successfully received packets was on average 3 time more and in some cases increased by a factor of 6. The new telemetry client software designed to incorporate the new demodulator also performed as expected and uses a flexible and modular framework that facilitates future upgrades and modifications. Incorporating new SDR equipment, modulation schemes and forward error-correcting techniques is now trivial and require little to no modification to the core modules of the software. Even though the new telemetry client was designed for maximum BER performance rather than code simplicity, it was shown that even on modest hardware, real-time demodulation and decoding was achievable for sampling rates under 48000 kHz.

In conclusion, the developed demodulator has shown excellent performance characteristics approaching the theoretical limit. When used for the current missions, it can more than double the amount of collected telemetry data. However, when the new telemetry client is distributed to the participating radio amateurs, the improved packet reception rate can lead to a huge increase in the number of collected packets. Furthermore, it was established that the new demodulator is capable of operating at a data-rate of 9600 bps and is fully qualified for the upcoming DelFFi mission. With this, all of the primary objectives of the study were successfully achieved.

Furthermore, this study establishes a new baseline for performance of SDR-based BPSK demodulators in satellite communications, which allows future researchers to have a reference to quantify their improvements, optimizations and advancements. The results and methodology used to obtain them were compiled into a conference paper that has already been accepted into the Small Satellites, Systems and Services (4S) conference. This will hopefully accelerate the level of research conducted in the area of high performance demodulators for space communications and direct the path of future research. This paper can be view in Appendix B.

Apart from the scientific significance of this study, the newly developed BPSK demodulator will enable hundreds of radio amateurs around the world to listen to the DelFFi and other satellites (employing BPSK modulation scheme) using cheap SDR and antenna tracking equipment as well as low gain antennas and will ultimately help attract more individuals towards the scientific and

---

engineering fields.

## Chapter 5

# Discussion and Recommendations

As shown in Chapter 4, the performance of the newly developed demodulator closely approaches the theoretical limit. With only a fraction of dB of improvement still to be gained, the point of diminishing returns has been reached when it comes to the demodulator performance. At this point, it is far more worthwhile to pursue other paths for improving the link quality. As the research into improving the BER of the demodulator was under way, a number of parallel avenues for improving the reliability and performance of the telemetry link were identified.

One may wonder, why these new methods were not employed during this research and the development of the new telemetry client. As stated in Chapter 1, the current research was limited to the design of the demodulator and telemetry client. Therefore, the design of the satellite transmitter was out of the scope of this study. Since, the methods described in this chapter require some level of modification to the transmitter, they were not considered for the upcoming DelFFi mission and thus this study. However, they remain viable options for future missions with even higher link budget requirements.

One of the potential methods is the use of Error Correcting Codes (ECC). The second method is the use of pulse shaping. The aim of this chapter is to provide a brief insight into these concepts and show how their potential can be exploited for the future missions.

### 5.1 Error Correcting Codes

Forward error correction coding or ECC can significantly reduce the  $E_b/N_0$  requirement, which in turn reduces the required transmitter power and antenna size, or increases the link margin. The concept of ECC is very simple. Extra bits, called parity bits, are inserted into the data stream at the transmitter. These bits enable the receiver to detect and correct for a limited number of bit errors which might occur in transmission because of noise or interference. While computationally complex, these techniques can be implemented at relatively low cost, using large scale integrated circuits with small size and low power consumption or alternatively implemented in software and executed on general purpose microprocessors. The use of ECC does come with its own set of disadvantages. Mainly, the extra error correction bits increase the required data-rate and hence the transmission bandwidth, often a scarce resource. Also, initial signal acquisition can still be very challenging at a low  $E_b/N_0$ , even if the BER is improved due to the use of ECC [26]. This is why particular attention was given to the initial signal acquisition performance of the new demodulator.

There is a value of  $E_b/N_0$  equal to -1.59 dB, known as the Shannon Limit, below which no error-free communication at any information rate can take place. This is derived from the Shannon-Hartley theorem, which states that the maximum theoretical data rate,  $R_{max}$  which can be transmitted over

a transmission channel with bandwidth,  $B$ , is:

$$R_{max} = B \cdot \log_2 \left( 1 + \frac{C}{N} \right) \quad (5.1)$$

Where,  $C/N$  is the average carrier-to-noise power ratio in the channel [21]. The Shannon limit cannot be reached in practice because the transmission bandwidth and coding complexity increases without bound as this limit is approached. The desire to inch ever closer to the Shannon Limit has resulted in numerous advancements in the field of ECC over the past 50 years and has significantly influenced the field of satellite communications, perhaps more than any other field.

### 5.1.1 Background Information

The use of ECC has a long history within the aerospace field. Prior to 1960s, nearly all satellites and spacecraft used uncoded communication channels. However, starting from 1968, the Mariner missions began employing convolutional codes and ReedMuller codes, thus ushering a new era of ECC in satellite communications [1]. Without coding, 26% of the images received from this spacecraft would contain errors, unacceptably poor quality for the nature of the mission. The particular code employed in the later Mariner missions was the Reed-Muller [32, 6, 16] binary code. Code words are 32 bits long and the minimum distance is 16, resulting in a 7-error correcting code which ultimately meant that only 0.01% of the transmitted images contained errors [5].

Later in 1977, the Voyager 1 and 2 missions, were required to transmit full color images as well as other high value scientific data of Jupiter and Saturn. This meant that a higher performance coding technique had to be implemented and thus the transmitted messages were coded by (optimally Viterbi-decoded) convolutional codes [11]. A rate-1/2 convolutional code was implemented by generating and transmitting two bits for each data bit. The data rate is therefore one half the transmitted bit rate (hence "rate-1/2"). As shown in Figure 5.1, this K=7 convolution code greatly reduces the  $E_b/N_0$  required to obtain a specified BER. For example, a BER of  $10^{-5}$  is achieved with an  $E_b/N_0$  of 4.4 dB. This represents an improvement, or coding gain, of 5.2 dB below the 9.6 dB required for uncoded BPSK. Over the years this error correction technique became so common that it was adopted as NASA/ESA Planetary Standard Code by the Consultative Committee on Space Data Systems (CCSDS) and has been wide spread utilization in various applications, including satellite communication and cellular telephony.

The Voyager 2 craft additionally supported an experimental implementation of a ReedSolomon code, the concatenated ReedSolomonViterbi (RSV) code which allowed for very powerful error correction and enabled the spacecraft's extended journey to Uranus and Neptune [27]. The experimental concatenated coding scheme was so successful that the subsequent Pioneer deep-space communication link used this technique to obtain the performance required to overcome the large space loss as a result of the 12 billion kilometer separation. As shown in Figure 5.1, the BER performance for this concatenated code is only 4.2 dB above the Shannon limit at a BER of  $10^{-5}$ .

These concatenated codes are also excellent at correcting burst errors. Various forms of concatenated ReedSolomon/Viterbi-decoded convolutional codes were and are used on the Mars Pathfinder, Galileo, Mars Exploration Rover and Cassini missions. These codes have enabled reliable communications to within approximately 1.5 dB of the ultimate limit imposed by the Shannon capacity [27]. Using the recently developed turbo coding and low-density parity-check (LDPC) methods, it is possible to achieve an error performance only a fraction of a decibel away from the Shannon limit. As a result of the incredible performance of turbo and LDPC codes, from 2004 concatenated codes are increasingly falling out of favour with space missions, and are replaced by these powerful error correction codes [22].

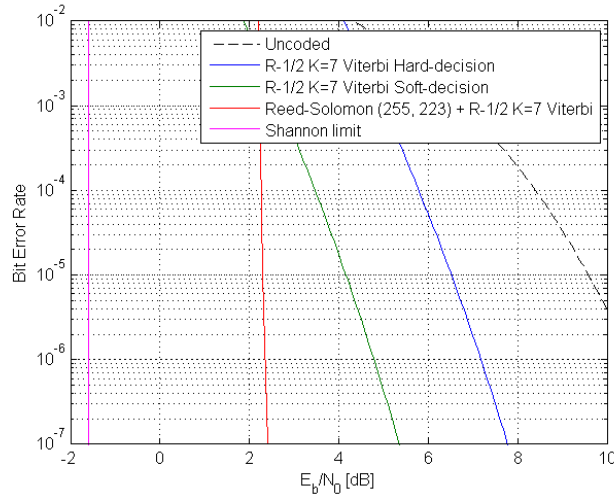


Figure 5.1: BER of various coding techniques

### 5.1.2 Analysis

With an overview of the available and space proven coding schemes at hand, it is possible to analyse the requirements and constraints of CubeSat missions in order to select a suitable ECC. At first glance it may appear beneficial to always employ the high performance turbo or LDPC codes regardless of the mission parameters. However, the vast difference between the kinds of deep space and orbital missions that are conducted suggest that trying to find a "one size fits all" error correction system will be an ongoing problem for some time to come. For example, the type and amount of data being transmitted plays an important role in the selection of the appropriate error correction code. Furthermore, for missions close to Earth, the nature of the channel noise is different from what a spacecraft on an interplanetary mission experiences. Additionally, as a spacecraft increases its distance from Earth, the problem of correcting for noise gets larger and as such a higher level of encoder/decoder complexity is tolerated.

In the case of power-limited systems, where power is scarce but bandwidth is available, coding makes sense. Most space systems today use some forward error correction coding to save transmitter power unless the data rate is greater than several hundred Mbps, in which case limits on both bandwidth and hardware speed become significant [26]. As is the case for most CubeSats (and other nano-satellites) the power budget is very limited and so reducing the transmission power is highly desirable. The primary transceivers aboard the twin DelFFi satellites are produced by ISIS Co. and operate at the 435 MHz band which is allocated as an international amateur satellite frequency by the Amateur Satellite Service [24]. The mission requires a bit rate of 9600 bps for the telemetry downlink. The bandwidth of the primary lobe of a BPSK modulated signal is given by Equation 2.3 and is equal to 19.2 kHz for a 9600 bps data-rate.

The university was given a 20 KHz channel for the Delfi-C3 and Delfi-n3Xt missions. This doesn't provide much room for the overhead of most of the aforementioned coding schemes. However, since the DelFFi transmitters operate at the 435 MHz band, a larger channel bandwidth could be available. Furthermore, there is another pressing constraint besides the regulatory restrictions on the bandwidth. As previously mentioned, one of the objectives of the mission is to involve radio amateurs to participate in collecting the telemetry data. To achieve this goal, a simple analogue front-end was designed which could be built cheaply from commercial off the shelf (COTS) parts. This front-end is designed to work in conjunction with a PC sound-card as the final ADC stage. According to the Nyquist theorem, in order to be able to fully reconstruct the original signal, the RF signal must be sampled at a rate equal to at least twice the highest frequency in the signal

spectrum. However, practical considerations, such as realizable filter limitations, suggest that the sampling frequency should be at least 2.2 times the maximum input frequency. This means that a common sound-card with a sample rate of 44.1 KHz can be used for signals with a bandwidth of up to approximately 20 KHz thus eliminating the potential to use ECC. However, with more and more demand for high-fidelity audio, sound-card manufactures are beginning to sell 96 KHz (and higher) sample rate sound-cards. Furthermore, dedicated SDR hardware are become cheaper and easier to acquire. This would enable the use of a rate-1/2 coding scheme for the future missions.

The next problem to tackle is the complexity of the encoder for the selected coding scheme. The transceivers aboard the satellites are equipped with low-power 16-bit microcontrollers with a computational performance of 20 DMIPS. These processors are already tasked with packaging the incoming data (from the onboard computers) into the standard AX.25 packet format and controlling various aspects of the transceivers. As such they would be incapable of encoding the telemetry data (at a rate of 9600 bps) for even the simplest coding scheme. Generally, Application Specific Integrated Circuits (ASIC) would accomplish this task. However, in absence of such device an FPGA would provide a good alternative. Due to the streaming nature of convolution codes, they represent the obvious choice for an FPGA implementation. Implementation of these encoders can be achieved using shift registers which are abundant on even the smallest FPGAs [13]. Block codes on the other hand require more memory and complex timing circuitry for cross clock-domain synchronization.

To summarize the results of the analysis, the DelFFi mission as well as future missions can benefit from a rate-1/2 convolution code. This coding scheme would consume a bandwidth 38.4 kHz (assuming a 9600 bps BPSK modulated link) which can be sampled with modern sound-cards. Furthermore, the streaming nature of convolution codes means that a small FPGA board can be used to interface the onboard computer with the transmitter at a relatively small cost (in terms of price, size, weight and power consumption). The Planetary Standard Code (rate-1/2, K=7) convolutional code adopted by NASA/ESA would be a good ECC for the these missions. Part of the regulations governing the use of international amateur satellite frequencies state that all communications protocols (thus also coding schemes) must be publicly available. The use of this standard code means that no separate coding specifications need to be published by the university. Furthermore, this code has been implemented by a large number of missions and has been thoroughly tested and characterized which should help in the design, development and testing stages.

The optimal Viterbi decoder would be implemented in software alongside the BPSK demodulator. Since, a software-defined based demodulator is used, the recovered baseband signal is available. The absolute value of the amplitude of this signal at the sampling instant (bit sampling) provides a measure of the reliability of the received bits. This provides the means to implement a soft-decision Viterbi decoding algorithm which leads to a better performance. When comparing hard and soft decision decoding (see Figure 5.1), the same bit error probability is typically achieved at a SNR of 2 to 3 dB lower.

As it can be seen in Figure 5.1, at a BER of  $10^{-6}$  a coding gain of 5.7 dB can be achieved in comparison to the uncoded BPSK channel. The BER of  $10^{-6}$  is used in this scenario as the maximum allowable BER for the mission. The coding gain means that the transmission power of the transmitter can be reduced by 5.7 dB. Considering the fact that most RF power amplifiers are only 40% to 50% efficient, the use of such an ECC can result in considerable power savings. Currently, the DelFFi satellites are designed to transmit data only during the day (when the solar panels can directly provide the required power) and disable their transmitters when they are passing through the Earths shadow. The reduced power consumption as a result of ECC could potentially allow us to use the onboard batteries for continuous telemetry downlink. This would increase the contact time by over 40% reducing the constraint on the storage and data handling subsystem as well as enabling new scientific goals for the mission.

In conclusion, although very shallow in depth, this preliminary study shows that the potential gains of using error correction codes for the DelFFi mission can be enormous and certainly justify extended research into this area.

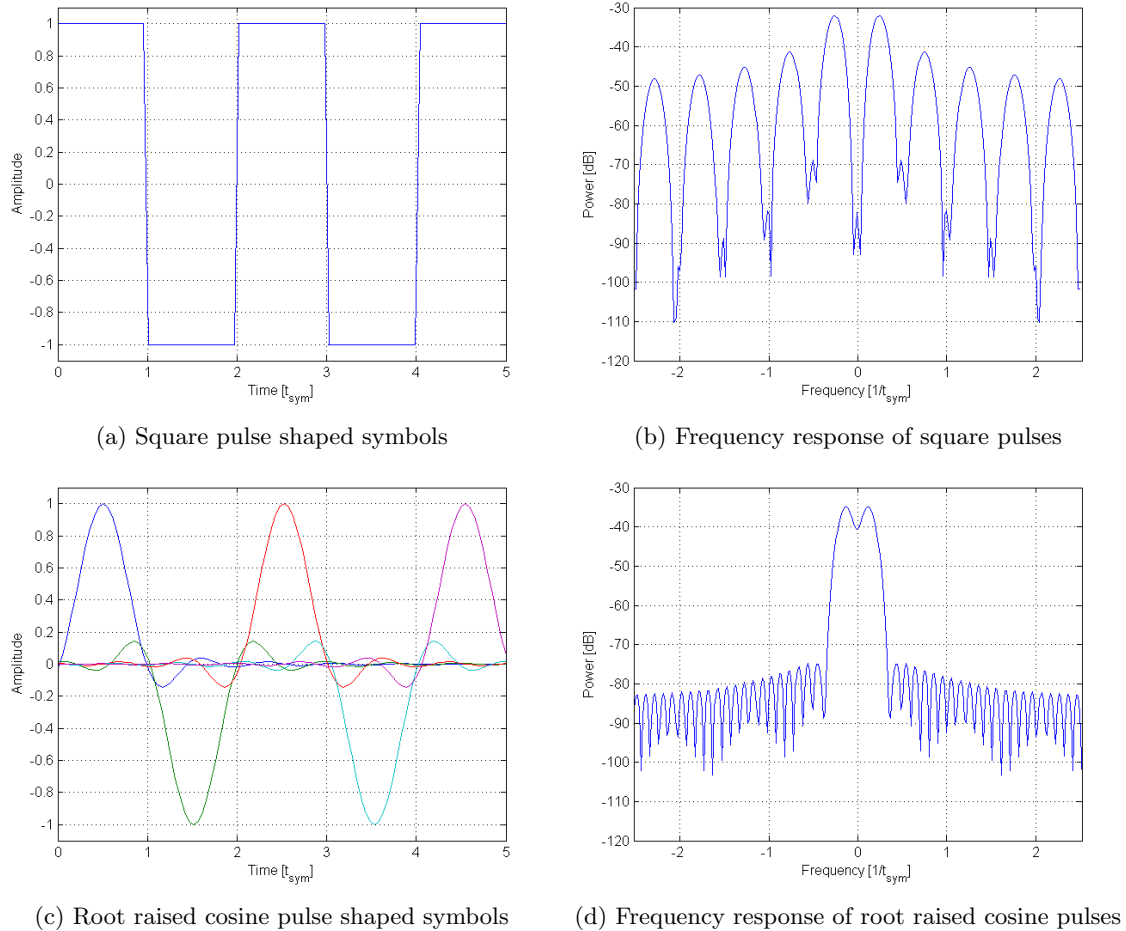


Figure 5.2: Pulse shaping

## 5.2 Pulse Shaping

Pulse shaping is another technique that can be used to improve the quality of the transmission link. The incorporation of a pulse shaping filter in a communications system (both transmitter and receiver) can lead to significantly improved bandwidth efficiency and BER performance as a result of reduction of ISI. On the transmitter, a pulse shaping filter is applied to the each symbol before transmission. The inverse operation is performed by the receiver to recover the transmitted message. The idea is that the shaped symbol waveform exhibits a number of advantageous characteristics when compared to a simple square pulse.

The root raised cosine pulse, shown in Figure 5.2c, is one example of a pulse shape that meets both of these requirements. Because of the windowing affect that it has on each symbol period of a modulated signal, it can utilize a smaller portion of the frequency domain. The frequency spectrum of the root raised cosine pulse along with frequency spectrum of a square pulse is shown in Figure 5.2.

### 5.2.1 Background Information

When no pulse shaping is used, sharp transitions occur when data bits change polarity. It is well known that the frequency spectrum of a rapidly rising or falling signal (as seen in a square signal),

contains a large number of higher order harmonics of the fundamental frequency. Figure 5.2b shows the frequency spectrum of the signal when no pulse shaping is used. As it can be seen, the figure shows significant channel power outside of the main lobes. In a satellite communication system, it is vital to limit all of the signal power to the information carrying main lobe. In doing so, the transmission power is not wasted on amplifying the redundant portions of spectrum. Perhaps more importantly, the reduced out-of-band transmissions can reduce adjacent channel interference or enable more channels to be allocated within a given amount of bandwidth.

In comparison, the root raised cosine pulse is periodic in nature and it has a maximum amplitude in the middle of the symbol period (meaning it does not interfere with neighbouring symbols). By applying a pulse-shaping filter to the modulated sinusoid, the sharp transitions are smoothed out and the resulting signal becomes limited to a specific frequency band. Figure 5.2c illustrates the 5 transmitted data symbols when using this pulse shaping technique. For illustration purposes, the 5 symbols are plotted individually with different colors. The transmitted baseband signal is the superposition (summation) of these signals and closely resembles a sinusoidal wave.

As previously mentioned, some forms of pulse shaping can also reduce ISI and thus increase the BER performance. To understand how this is accomplished, it is important to first discover the origin of ISI in satellite communications. As the transmitted signal travels across large distances and through various mediums, the symbols tend to spread beyond their original symbol period. This means that each symbol can also affect the following and preceding symbols. Pulse shaping can decrease ISI by ensuring that the effect of each symbol (after spreading) is zero at the ideal sampling instant of the neighbouring symbols. As it can be observed on Figure 5.2c, the root raised cosine pulses from subsequent symbols actually overlap on one another. However, because the peak of each pulse corresponds with the zero crossing point of the following raised cosine pulses, ISI is minimized. Another very important advantage of the root raised cosine pulse shape is the fact that it also serves as a matched filter.

### 5.2.2 Analysis

The root raised cosine filter is type of sinc filter designed to exhibit a unity gain response at low frequencies (near DC) and block all higher frequencies. This pulse shaping filter is commonly used in pairs, where the transmitter first applies a raised cosine filter to the transmitted message. Upon reception, the receiver passes the signal through another raised cosine filter (a matched filter) thus completing the root raised cosine filtering. The mathematical representation of the root raised cosine filter is:

$$h_{SRC}(t) = \frac{\frac{4\alpha}{\pi} \cos\left(\frac{(1+\alpha)\pi n}{R}\right) + (1+\alpha) \operatorname{sinc}\left(\frac{(1-\alpha)\pi n}{R}\right)}{\sqrt{R} \left[1 - \left(\frac{4\alpha n}{R}\right)^2\right]} \quad (5.2)$$

Where,  $\alpha$  is the roll-off factor, which determines the sharpness of the frequency response, and  $R$  is the number of samples per symbol. The result of the root raised cosine filter with a roll-off factor of  $\alpha = 0.5$  on the 9600 bps BPSK modulated signal can be viewed in Figure 5.3.

The figure clearly shows that the modulation harmonics of the BPSK signal are completely suppressed when pulse shaping is used. The vertical red lines indicate the frequency boundaries of the primary lobe. It can be seen that even the bandwidth requirements of the primary lobe has seen significant improvement. The primary lobe of the original signal occupies a 19.2 kHz bandwidth (as predicted by the Equation 2.3, while the root raised cosine filtered signal requires a bandwidth of approximately 15 kHz.

In conclusion, the usage of pulse shaping can have many beneficial consequences. It can greatly reduce ISI due to signal spreading, while simultaneously reducing bandwidth requirements and eliminating out of band transmissions. Even though reducing the occupied bandwidth doesn't improve

## 5.2. PULSE SHAPING

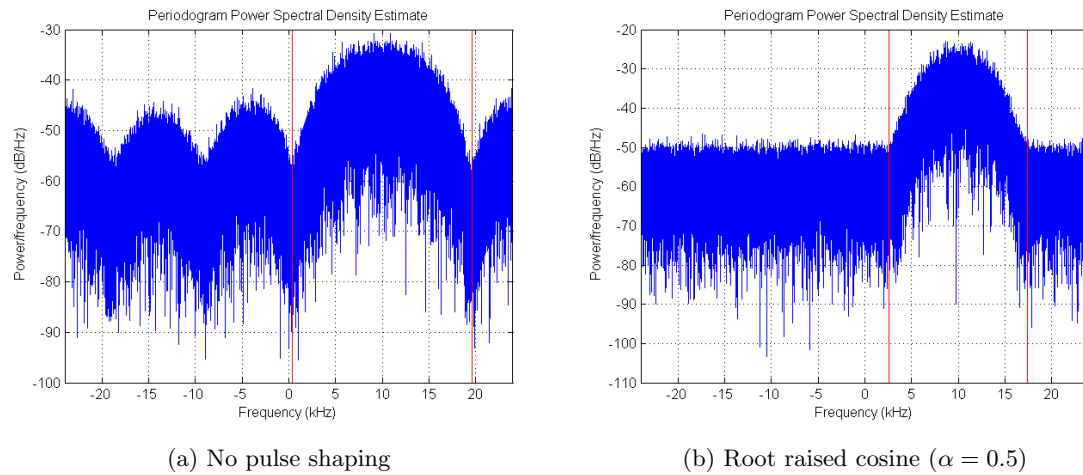


Figure 5.3: Frequency spectrum of a 9600 bps BPSK modulated signal at a carrier offset of 10 kHz

the BER performance of the communication link, it enables the use of forward error-correcting techniques by decreasing the bandwidth requirements.

The implementation of the the root raised cosine matched filter in the newly developed demodulator is trivial. In fact as outlined in Section 2.3, a simple matched filter (for a square pulse) is already being used in the current implementation. The only required modification is the replacement of the filter coefficients with those of a root raised cosine filter. The biggest challenge to implementing this technique is the requirement of a complete redesign of the transmitters for future missions.

# References

- [1] K. Andrews. The Development of Turbo and LDPC Codes for Deep-Space Applications. *Proceedings of the IEEE*, 95(11), 2007.
- [2] A. Asad. Direct Carrier Modulation Schemes. Master's thesis, University of Technology and Engineering Lahore, 2010.
- [3] V. S. Bagad. *Wireless Communication*. Technical Publications, 2009.
- [4] K. Borre. *A Software-Defined GPS and Galileo Receiver: A Single-Frequency Approach*. Applied and Numerical Harmonic Analysis. Birkhuser Basel, 2007.
- [5] W. Cherowitzo. Combinatorics in Space, the Mariner 9 telemetry system. *Proceedings of the IEEE*. URL <http://www-math.ucdenver.edu/~wcherowi/courses/m7409/mariner9talk.pdf>.
- [6] L. Doyle. *Essentials of Cognitive Radio*. Cambridge University Press, 2009.
- [7] J. Feigin. Practical Costas loop design. Technical report, Mobile Dev Design, 2002.
- [8] T. Flohrer. Assessment and Categorization of TLE Orbit Errors for the US SSN Catalogue. *Aboa Space Research Oy (ASRO) at Space Debris Office*, 2008.
- [9] F. M. Gardner. *Phaselock techniques*. A Wiley-Interscience Publication. Wiley, 1979.
- [10] H. A. Haldren. Studies in Software-Defined Radio System Implementation. Senior Honors Theses. Paper 420, 2014.
- [11] W. William Cary Huffman. *Fundamentals of Error-Correcting Codes*. 2003.
- [12] P. K. Jain, S. Pal, and V. M. Pandharipande. Regenerate Coherent Carriers From PSK Signals. Technical report, Microwaves and RF, 2004.
- [13] M. Javeed and B. Swapna. High speed convolution encoding and Viterbi decoding using dynamic shift register. *IEEE*, 7(5), 2014.
- [14] T. S. Kelso. Two-Line Element Set Format. *Satellite Times*, 4(5), 1998.
- [15] B. P. Lathi. *Modern Digital and Analog Communications Systems*. Oxford University Press, 1983.
- [16] M. R. Maheshwarappa, M. Bowyer, and C. P. Bridges. Software Defined Radio (SDR) architecture to support multi-satellite communications. pages 1–10, 2015.
- [17] J. Mevada, J. Samuel, S. Bhadane, A. K. Gulati, and R. D. Koilpillai. Design and Implementation of a Robust Downlink Communication System for Nanosatellites.
- [18] K. H. Mueller and M. Muller. Timing Recovery in Digital Synchronous Data Receivers. *IEEE Transactions on Communications*, 25(5):516–530, 1976.

## REFERENCES

---

- [19] John G. Proakis. *Digital Communications*. McGraw-Hill, 2007.
- [20] B. B. Purkayastha and K. K. Sarma. *A Digital Phase Locked Loop based Signal and Symbol Recovery System for Wireless Channel*. Springer, 2015.
- [21] C. E. Shannon. Communication in the Presence of Noise. *Proceedings of the Institute of Radio Engineers*, 37(1), 1949.
- [22] A. Shokrollahi. *LDPC Codes: An Introduction*. Digital Fountain Inc., 2003.
- [23] T. Ulversoy. Software Defined Radio: Challenges and Opportunities. 12(4):531–550, 2010.
- [24] International Amateur Radio Union. *Spectrum requirements for the Amateur and Amateur-Satellite Services*, 2013. URL [http://www.iaru.org/uploads/1/3/0/7/13073366/spectrum\\_requirements\\_rev2\\_nov\\_2014.pdf](http://www.iaru.org/uploads/1/3/0/7/13073366/spectrum_requirements_rev2_nov_2014.pdf).
- [25] A. Vaneli-Corali, G. E. Corazza, G. K. Karagiannidist, P. T. Mathiopoulosl, D. S. Michalopoulost, C. Mosquera, S. Papaharalabost, and S. Scalise. Satellite Communications: Research Trends and Open Issues. pages 71–75, 2007.
- [26] J. R. Wertz, D. F. Everett, and J. J. Puschell. *Space Mission Engineering: The New SMAD*. Microcosm Press, 2011.
- [27] S. B. Wicker and V. K. Bhargava. *Reed-Solomon Codes and Their Applications*. 1999.

## Appendix A

# DUDe BER Analysis

The Delft Universal Data extractor (DUDe) is the software fulfilling the task of telemetry data client for the current missions. It is designed to be used by the ground control station operators as well as radio amateurs for demodulating, processing of raw data and providing a graphical representation of the processed data. The collected packets are then sent to a central database for further processing and archival. This system allows telemetry data to be received from various amateur and professional ground stations all over the world thus effectively increasing the per orbit downlink budget. The hierarchy of this system is illustrated in Figure 1.1.

More importantly for this study, the demodulator as used by the DUDe client is depicted in Figure 1.2. From this figure it is quite clear that a standard Costas loop is being used to recovery the carrier. The clock and data recovery uses a counter to sample the demodulated signal which is converted into a binary bit string.

In principle, this architecture should provide a similar performance as predicted by the theory. In order to validate the performance, a MATLAB script was developed to produce a SSBSC-BPSK modulated signal identical to what the satellite transmits. Known amounts of Gaussian noise is then injected into the signal and the result is fed into the DUDe client. To simplify the experiment, no attempt was made to simulate the Doppler shift and the signal was modulated using the precise frequency that the receiver was tuned to. The received and demodulated packets were then compared to the transmitted sequence of binary data. The calculation of the BER is accomplished using:

$$\text{BER} = \frac{\text{Number of bit errors}}{\text{Total number of transmitted bits}} \quad (1.1)$$

The results of this experiment for various signal-to-noise ratios (SNR) are provided in Figure 1.3. It may be hard to observe in the logarithmic graph, however, the calculated BER is twice as high as the theoretical BER for a SNR of 1dB. This difference grows to a factor of 75 for a SNR of 10dB.

Throughout the experiments a number of other issues were discovered. For example, the carrier recovery loop would consistently lose synchronization at signal-to-noise ratios of 2dB and below. Only 1 in a 100 transmitted packets were received due to this issue. Below a signal-to-noise ratio of 1dB, Costas loop lock was never achieved. Furthermore, the clock and data recovery component also presented signs of trouble. When data transitions are absent for a number of consecutive bits, the clock and data recovery algorithm of DUDe failed to sample the demodulated signal at the correct instant. A clear sign of this problem is when the received binary data becomes inverted at a certain point in the packet (see Table 1.1). It is important to note that the first 8 bits of the illustrated bit string is the standard AX.25 packet header which contains 6 consecutive high bits and is enough to cause a loss of bit-synchronization at low signal-to-noise ratios. The AX.25 protocol is currently used by the Delfi-n3Xt satellite.

Lastly, the current demodulator is designed to be complaint with the requirements of the Delfi-n3Xt mission. The transmitter aboard this satellite transmits with a data-rate of 2400bps. As a part of the QB50 mission, the DelFFi satellites need to transmit large amounts of science data to the ground stations. For this reason a data-rate of 9600bps was deemed necessary.

The required bandwidth for a 9600bps SSBSC-BPSK modulated signal is given by Equation 1.2 and is equal to 19.2 [kHz].

<b>Transmitted</b>	01111110101110100100000
<b>Received</b>	01111110010001011011111

Table 1.1: Loss of bit-synchronization

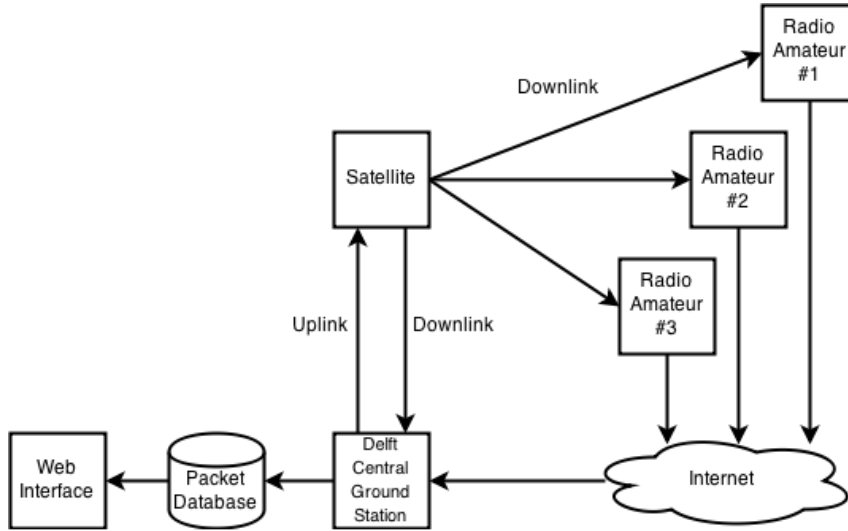


Figure 1.1: Hierarchical view of the DUDe telemetry system

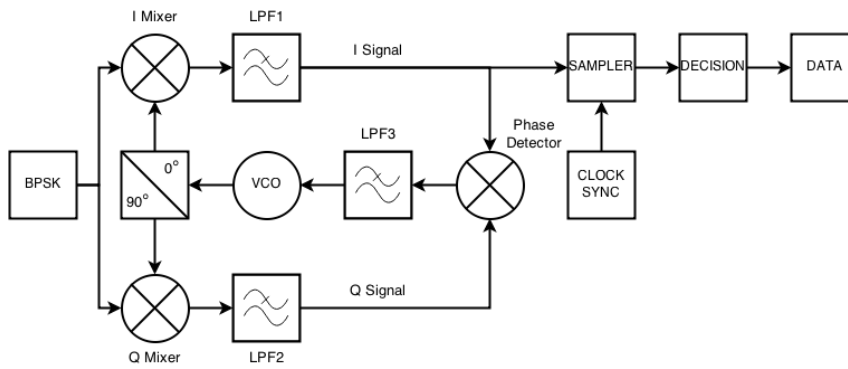


Figure 1.2: Block diagram of the DUDe demodulator

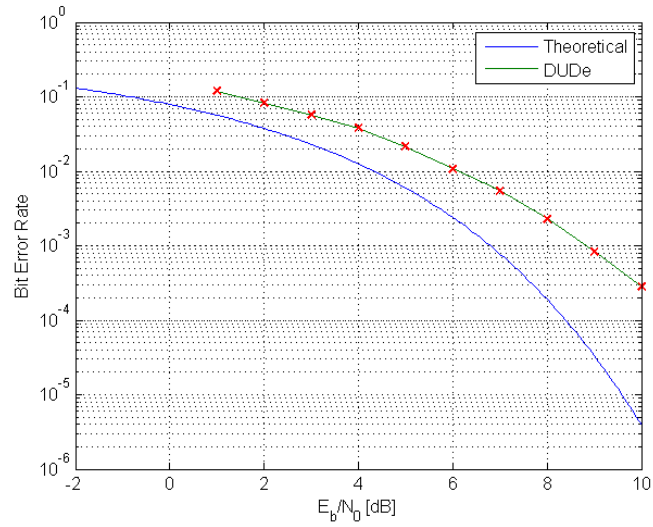


Figure 1.3: Bit error rate (BER) curve of the DUDe demodulator

$$f_w = \frac{2}{T} = 2 \cdot \text{bit-rate} \quad (1.2)$$

According to the Nyquist theorem to fully capture the contents of a signal with bandwidth  $f_b$ , a sampling rate of  $2f_b$  is required. In order to reduce the hardware and equipment requirements for the radio amateurs, the DUDe client was designed to operate from samples obtained from a sound card. The sample rate of common sound cards is limited to 44.1 kHz. This sample rate is just above the Nyquist rate for capturing the DelFFi telemetry signal.

**Appendix B**

**Conference Paper**

4S Symposium 2016

# Design and Implementation of a High Performance BPSK Demodulator for Satellite Communications

Ehsan Tofigh\*, Jasper Bouwmeester†

February 25, 2016

## Abstract

The Delfi program is a development line of small satellites comprising the successful Delfi-C3 and Delfi-n3Xt CubeSat missions. As part of an effort to involve radio amateurs from all over the world, a telemetry client is designed which allows radio amateurs to demodulate, decode and display telemetry data. This software was designed for an RF front end connected to a soundcard acting as low-end baseband sampling device. It has been discovered that there was a significant gap of 5 dB between the required Signal-to-Noise Ratio (SNR) for the software demodulator and the theoretical required link margin. This paper presents an approach which decreases this gap while upgrading the demodulator for future use, taking advantage of emerging capabilities of Software Defined Radio (SDR) technology.

Today, SDRs have reached a high level of maturity and are slowly emerging in everyday communication systems. However, little information is available in literature on the real-world performance of SDRs for satellite communications. Furthermore, while many researchers have produced working software-defined demodulators, very little effort is spent on maximizing their performance. This gap in knowledge presents an opportunity to deliver significant contributions to the growing field of SDR communications, while simultaneously realizing the more practical goal of producing an improved telemetry client for the upcoming Delfi missions.

In this paper, we present an architectural overview and analysis of a high performance DSP-based implementation of Binary Phase Shift Keying (BPSK) demodulator. We give particular attention to the Bit-Error Rate (BER) optimization when there is no real-time demodulation constraint and computation time is abundant. The key to achieving this goal is identifying and tuning the critical factors that affect the performance of a BPSK demodulator. The proposed demodulator consists of a Costas loop for carrier recovery and Gardner algorithm for clock recovery. For low data rates, we have tested the scheme using a down converting analogue front-end and an ordinary sound-card as the radio frequency sampler. Demodulator performance was measured for simulated Additive White Gaussian Noise (AWGN) channels in MATLAB and validated experimentally using real satellite transmissions from the Delfi-n3Xt mission. The measured BER for data rates from 2.4 to 9.6 kbps is compared to the theoretical limit. It is shown that the new software demodulator lowers the required SNR by 5 dB as compared to the previously implemented telemetry client and is less than 1 dB from the theoretical limit.

\*Delft University of Technology, Netherlands, e.tofigh@student.tudelft.nl

†Delft University of Technology, Netherlands, jasper.bouwmeester@tudelft.nl

## Introduction

In this paper, we present an architectural overview and analysis of a high performance DSP-based implementation of a BPSK demodulator. We give particular attention to the BER performance when computational power is abundant as is the case for ground stations. The purpose of the new demodulator is to replace the current poorly performing demodulator for the upcoming DelFFi mission.

Over the past decade, Digital Signal Processor (DSP) based radios, often referred to as SDRs, have an increasingly prevalent role within wireless communication systems. Different than traditional hardware radios which implement radio protocols using static electrical circuits, SDRs implement significant aspects of physical radio protocols using software programs running on a DSP. Because they use software to implement most of the radio functionality, SDRs are much more easily modified, edited, and upgraded than their hardware-defined counterparts. Consequently, researchers and developers have been developing previously hardware-defined radio systems within software.

The migration from hardware-defined radios to SDRs corresponds with the move from analogue radio systems to digital radio system. This transition is the direct result of the rise of processing capabilities of microprocessors [1]. However, even using modern microprocessors, complex SDRs requiring dozens of digital DSP blocks are too computationally expensive to run in real-time. Most implemented SDRs have focused on simplifying the design to meet the computational constraints. There is little doubt that digital communication systems provide some key benefits over the existing analogue communication systems. Despite the advantages, however, SDRs still lag behind hardware radios in certain areas such as cost, reliability and power consumption [7]. As the primary driving force behind the recent advancements in the field of SDR, the consumer telecommunications industry has mainly focused on improving these deficiencies.

In satellite communications it is often beneficial to trade simplicity, low cost and low power with performance. This is specially true for the ground segment of satellite communication systems. In these systems, sufficient computational capability is available for real-time demodulation of low data-rate signals. Even when higher data-rates are re-

quired and when real-time demodulation is not essential, the received RF signal can be digitized and recorded onto storage mediums. The pre-recorded RF signal can then be processed "off-line" and as such computational complexity and time become irrelevant. This means that an SDR system for a ground station can focus on achieving the best possible performance at the cost increased computational complexity and power consumption.

The Delfi program is a development line of small satellites comprising the successful Delfi-C3 and Delfi-n3Xt CubeSat missions. As part of an effort to involve radio amateurs from all over the world, a telemetry client is designed which allows radio amateurs to demodulate, decode and display telemetry data. The SDR approach used for implementing the telemetry software provides the necessary flexibility to both the ground control operators as well as radio amateurs to adapt to future missions, with differing data-rates and modulation schemes, without costly equipment overhauls. This software was designed for an RF front end connected to a sound-card acting as low-end baseband sampling device. It has been discovered that there was a significant gap of 5 dB between the required SNR for the software demodulator and the theoretical required link margin. This paper presents an approach which decreases this gap while upgrading the demodulator for future use, taking advantage of emerging capabilities of Software Defined Radio (SDR) technology.

## Design of the distributed ground control station

In order to involve radio amateurs from all over the world, Delfi-C3 and Delfi-n3Xt have a downlink in the amateur satellite segment of the VHF amateur radio frequency band. Telemetry decoding software is available to participating radio amateurs which allows them to demodulate, decode and display telemetry data in real-time. Furthermore, the software allows for automatic transfer of all collected frames to the central Delfi database via the Internet. This SDR approach is key to providing the necessary flexibility to both the ground control operators, but more importantly the radio amateurs, to adapt to future missions, with dif-

fering data-rates and modulation schemes, without costly equipment overhauls.

This system allows telemetry data to be received from various amateur and professional ground stations all over the world thus effectively increasing the total downlink volume over time. The hierarchy of this system is illustrated in Figure 1. To reduce the hardware requirements for the radio amateurs, the new BPSK demodulator is designed to operate with the relatively low sampling rate of a PC soundcard.

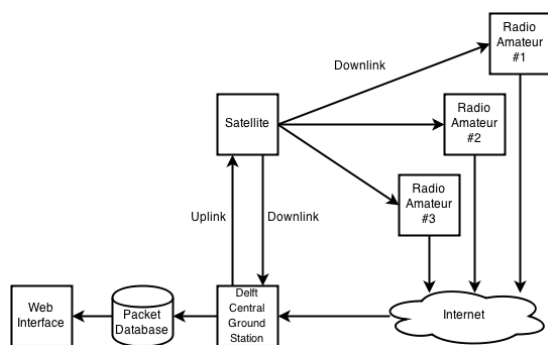


Figure 1: Hierarchical view of the distributed ground station system

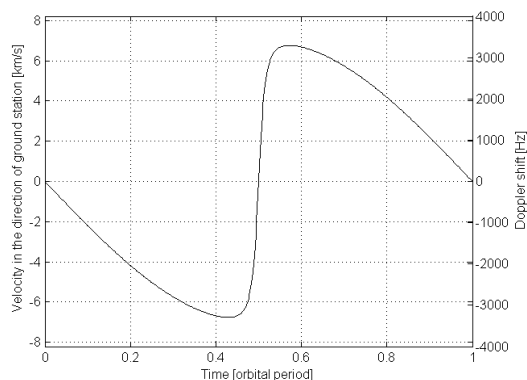
## Challenges

For a LEO satellite, the relative motion between satellite and ground station will be high and accelerated in nature. Due to the time-varying relative velocity, the Doppler shift keeps varying and the rate of change of Doppler shift will be at its peak at the highest elevation angle. In particular, for a satellite in a nearly circular LEO orbit with a mean altitude of about 700 km, the maximum Doppler offset on the VHF band would be about 8 kHz. The rate of change of Doppler offset, in this case around zenith point, would be about 35 Hz/s. Figure 2 shows the Doppler pattern (called S-pattern) observed over one pass for Delfi-n3Xt which is a CubeSat with a mean altitude of 712 km.

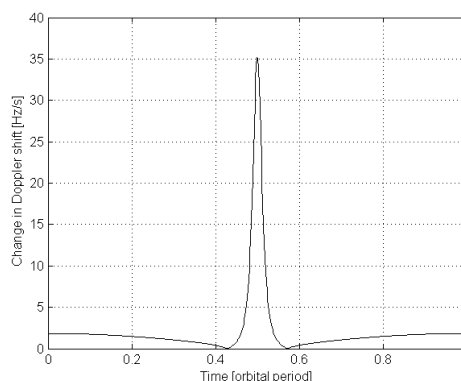
This frequency offset has to be corrected at the ground station accurately to achieve the best link performance. A rough estimate of this offset can be calculated using the Two Line Element (TLE) set which is made available on-line once the satellite is in its final orbit. This data is subsequently updated intermittently by NORAD. The Doppler

estimate from TLE gets increasingly inaccurate as the TLE data gets older. Hence there is a need for accurate Doppler frequency offset estimation and tracking which needs to be taken care of in the carrier recovery design of the proposed communication system [6].

Acquiring the satellite signal for the first time at low elevation angles is particularly challenging. Due to high slant range, the propagation loss will be at its peak which will result in lower SNR. Also at low elevation angles, the tropospheric fading effects will be considerable and ground reflection interference will be at its maximum [5].



(a) Doppler shift



(b) Rate of change of Doppler shift

Figure 2: The effect of Doppler shift

## Design of the BPSK demodulator

BPSK has excellent BER performance, strong anti-interference performance, fast transfer rates, low complexity, as well as other prominent features. These are some of the contributing factors that make BPSK one of the main modulation modes of satellite communication systems. The main disadvantage of this modulation scheme is its low spectral efficiency (compared to QPSK and MSK) and production of significant adjacent channel interference. Conventionally, digital modulation and demodulation are done using a dedicated chip. So its flexibility has been greatly restricted. With the rapid rise of processing capabilities of microprocessors and development of SDR technologies, it has become possible to realize the building blocks of BPSK demodulators in software and to achieve a fully software-defined BPSK demodulator.

### Carrier recovery

To achieve carrier synchronization, we have employed the tried and tested Costas loop. The Costas loop is a type of Phase Locked Loop (PLL) that is used for carrier synchronization in both analogue and digital receivers using BPSK modulation (and with slight modification for QPSK) [2]. This technique offers an inherent ability to derive a carrier from the received signal by self-correcting the phase (and frequency) of the locally generated carrier replica. Its main disadvantage is involvement of a loop settling time.

The mechanism of the Costas loop carrier recovery is to iterate its internally generated carrier, the VCO, into the correct phase and frequency based on the principle of coherency and orthogonality. The low-frequency product of a BPSK signal and its coherent carrier is the demodulated information.

The Costas loop in Figure 3 contains two multiplications. The first multiplication is the product between the input signal and the local carrier wave and the second multiplication is between a 90° phase-shifted carrier wave and the input signal. The goal of the Costas loop is to keep all energy in the *I* (in-phase) arm. To keep the energy in the *I* arm, some kind of feedback to the oscillator is needed. The multiplication in the *I* arm yields the

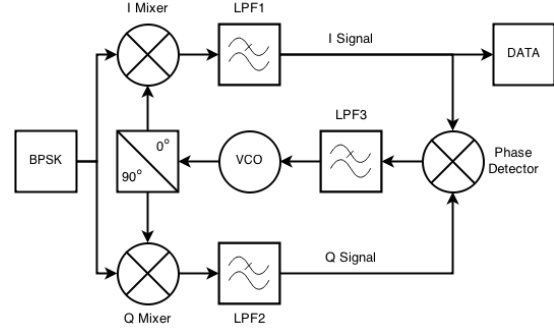


Figure 3: Block diagram of the Costas loop

following sum:

$$\begin{aligned} & DATA_N(t) \cdot \cos(2\pi f_c t) \cdot \cos(2\pi f_c t + \phi) \\ &= \frac{1}{2} DATA_N(t) \cdot \cos(\phi) \\ &+ \frac{1}{2} DATA_N(t) \cdot \cos(4\pi f_c t + \phi) \end{aligned} \quad (1)$$

Where  $\phi$  is the phase difference between the phase of the input signal and that of the local replica of the carrier phase. Similarly, the multiplication in the quadrature arm gives the following:

$$\begin{aligned} & DATA_N(t) \cdot \cos(2\pi f_c t) \cdot \sin(2\pi f_c t + \phi) \\ &= \frac{1}{2} DATA_N(t) \cdot \sin(\phi) \\ &+ \frac{1}{2} DATA_N(t) \cdot \sin(4\pi f_c t + \phi) \end{aligned} \quad (2)$$

If the two signals are low-pass filtered after the multiplication, the two terms with the double frequency are eliminated and the following two signals remain:

$$I_N = \frac{1}{2} DATA_N(t) \cdot \cos(\phi) \quad (3)$$

$$Q_N = \frac{1}{2} DATA_N(t) \cdot \sin(\phi) \quad (4)$$

The phase error of the local carrier replica can be found in Equation 5 and is used as the feedback term to the carrier oscillator.

$$\frac{I_N}{Q_N} = \frac{\frac{1}{2} DATA_N(t) \cdot \cos(\phi)}{\frac{1}{2} DATA_N(t) \cdot \sin(\phi)} = \tan(\phi) \quad (5)$$

$$\phi = \tan^{-1} \left( \frac{Q_N}{I_N} \right) \quad (6)$$

From Equation 6, it can be seen that the phase error is minimized when the correlation in the quadrature-phase arm is zero and the correlation value in the in-phase arm is maximum. The arctan phase detector (also referred to as discriminator) in Equation 6 is the most precise of the Costas discriminators. There are alternative discriminators that require substantially less processing power and computational time at the cost of reduced precision. These discriminators are described in Table 1 and are generally used for real-time demodulation applications.

Figure 4 shows the responses corresponding to the different discriminators. The phase discriminator outputs in this figure are computed using expressions in Table 1 for all possible phase errors.

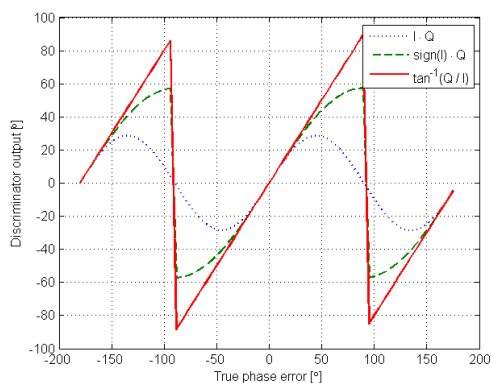


Figure 4: Comparison of common Costas loop discriminator responses

### *Clock and symbol recovery*

In a digital communication system, the output of the demodulator must be sampled periodically at the symbol rate, at the precise sampling time instants  $t_m = mT + \tau$ , where  $T$  is the symbol interval and  $\tau$  is a nominal time delay that accounts for the propagation time of the signal from the transmitter to the receiver. To perform this periodic sampling, a clock signal is required at the receiver. The process of extracting such a clock signal at the receiver is usually called symbol synchronization or clock recovery.

Clock recovery is one of the most critical functions that is performed at the receiver of a syn-

chronous digital communication system. It should be noted that the receiver must know not only the frequency ( $1/T$ ) at which the outputs of the demodulators are sampled, but also where to take the samples within each symbol interval. Clock recovery is further complicated by the fact that the oscillator that generates the clock signal for data recovery at the receiver is generally not synchronous in phase with that at the transmitter. Furthermore, the two oscillators may be drifting slowly with time, perhaps in different directions. The choice of sampling instant within the symbol interval of duration  $T$  is called the timing phase.

The clock signal can be extracted from the received data signal. There are a number of different methods that can be used at the receiver to achieve self-synchronization. In this study, we employed the widely used Gardner's algorithm. The Gardner timing recovery algorithm requires two samples per symbol and knowledge of the previous symbol timing to estimate the timing error for current symbol as shown in Figure 5. Timing error is computed as follows [4]:

$$e = \{y[nT] - y[(n-1)T]\} y[nT - T/2] \quad (7)$$

The Gardner's algorithm exhibits a number of beneficial characteristics that makes it a suitable choice for a high performance demodulator. Firstly, it is highly sensitive to carrier offsets. As such, the timing loop can lock first, therefore simplifying the task of carrier recovery. Secondly, it requires only two samples per symbol. Thus, it can be used for low sampling rate systems with medium to high data rates. The other two commonly used clock and symbol recovery techniques are early-late gate and Mueller and Muller methods. These methods have their own advantages and disadvantages compared to the Gardner's algorithm. However, the robustness of the Gardner's algorithm to carrier offsets was the determining factor in selecting this particular method for our BPSK demodulator.

### *Loop parameter optimization*

As it can be seen from Figure 3, the in-phase and quadrature arm filters (LPF1 and LPF2) are low-pass filters used to eliminate the double frequency component generated by the multiplier. Knowing

Discriminator	Description
$D = \text{sign}(I_N) \cdot Q_N$	The discriminator output is proportional to $\sin(\phi)$
$D = I_N \cdot Q_N$	The discriminator output is proportional to $\sin(2\phi)$
$D = \tan^{-1}\left(\frac{Q_N}{I_N}\right)$	The discriminator output is the phase error

Table 1: Various types of Costas discriminators

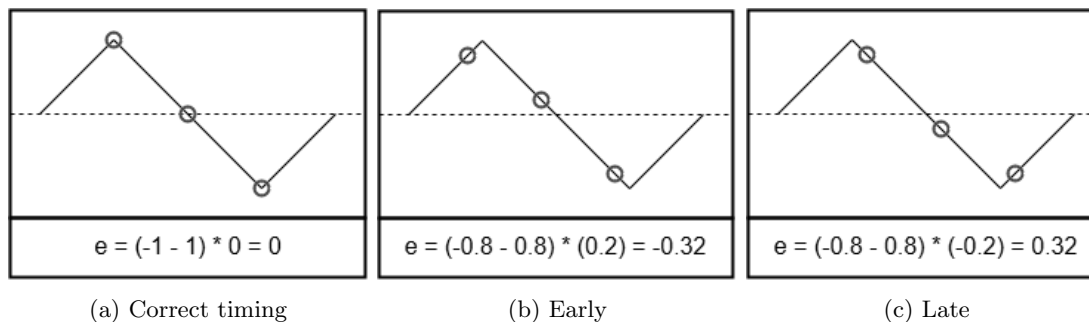


Figure 5: Gardner clock recovery

that no filter is ideal, a residual of the sum term always exists, but generally it's sufficiently attenuated. Both arm filters must be completely identical in terms of characteristics. As a result of component variations and manufacturing tolerances, creating identical analogue filters is extremely difficult if not impossible. For this reason, Costas loop implementations are much more prevalent in digital receivers where realizing identical filter responses is a trivial task.

Because the bandpass filter, incorporated into the analogue front-end, removes a great deal of unwanted noise, the arm filter requirements can be relaxed. The low pass filters in each arm must be wide enough to pass the data modulation without distortion. While the perfect demodulator requires that the filter exhibit no Inter-Symbol Interference (ISI), the practical design may use filters that trade cost, complexity, and size for some degree of SNR degradation. An optimization of the arm filter means that its bandwidth must be wide enough to minimize ISI, while narrow enough to minimize noise.

The output of the loop filter (depicted as LPF3 in Figure 3), is used to adjust the phase and frequency of the of the local carrier generated by the VCO (or NCO in a digital system). In our implementation,

this task is performed by a Proportional-Integral (PI) controller. The proportional and integral gains of this controller, in combination with the arm filters, determine the loop bandwidth of the Costas loop. The loop bandwidth in turn, largely determines the performance of the Costas loop in tracking the carrier signal. If the bandwidth is too small, the loop will be unable keep pace with the phase and frequency drift and carrier lock is lost or never achieved. However, if the bandwidth is too large, the loop becomes highly susceptible to noise which degrades the performance.

It is clearly evident that the highest BER performance is achieved when the loop bandwidth is as small as possible while still satisfying the minimum required bandwidth. In this paper, we propose to select the Costas loop bandwidth based on the worst case frequency shift rate. The primary contributor to the frequency shift is the Doppler shift. Figure 2b shows that the maximum measured rate of change of Doppler shift is limited to less than 35 Hz/s.

This value is the key factor in selecting the loop bandwidth that maximises the BER performance. As long as, the loop bandwidth is large enough to allow the loop to reliably track frequency shifts of 35 Hz/s, the highest noise rejection and thus best

BER performance is achieved. It is important to note that such an approach for finding the best gain is not suitable for all applications. For instance, a very low loop bandwidth also reduces the responsiveness of the loop and increases the time required to reach a steady state. For instance, when using the BER optimized loop bandwidth, the Costas loop takes tens of seconds to lock onto a signal with a 200 Hz initial offset. If no a priori knowledge of the satellite's orbit is known, then the receiver has to search the entire range of possible frequency shifts (also known as search space). This is sometimes referred to as the unaided acquisition time and can be approximated as:

$$t_{Acquire} = \frac{\Delta f}{f_{bw}} \cdot t_{lock} \quad (8)$$

Where,  $\Delta f$  is the range of possible Doppler shifts (as seen in Figure 2a),  $f_{bw}$  is the Costas loop bandwidth and  $t_{lock}$  is the lock time.

Thus, when using the optimum loop bandwidth (in terms of BER performance), the receiver could spend more than 5 minutes searching for a signal. Since, the contact time for LEO satellites is typically between 5 and 15 minutes, such a long acquisition time becomes problematic. It is important to note that the acquisition time can also be significantly improved with the aid of orbital parameters and orbital propagation algorithms to estimate the current Doppler shift of the satellite. Since orbital prediction software is already required for antenna tracking, this method is almost always employed in most ground stations. The rough estimate of this offset is generally calculated using the TLE sets which are made available on-line once the satellite is in its final orbit. This data is subsequently updated intermittently by NORAD. Unfortunately, the TLE sets are not always very accurate.

The accuracy of the TLE sets is dependent upon a large number of factors. Some of these factors include: the type of sensors used for measuring the TLEs, the number of observations, the orbital parameters as well as the conditions of the space environment. Sadly, all of these factors differ for each element set so the accuracy of the TLEs have to be determined on a case by case basis. To overcome these challenges, NORAD has been experimenting with various methods for incorporating TLE quality figures into the TLE sets themselves. Unfortunately, these methods have not been very successful

and the figures are rarely available.

Instead of assessing the accuracy of the TLE sets, their consistency can be evaluated. By analysing the degree to which a TLE set agrees with the prior and subsequent sets, an estimate of the consistency can be obtained. Assuming that the errors in each TLE set is statistically unbiased (random), the average difference (in magnitude) between the TLE sets can provide a good estimate of the general accuracy of the data.

A study performed by the European Space Agency (ESA) on the TLE orbit errors of a large number of satellites can be found in [3]. This study assessed and categorized the estimated uncertainty of these objects. Figure 6 illustrates these values for Low Earth Orbiting (LEO) satellites. As it can be seen, the magnitude of the position error for most LEO objects is in the order of 1 km at epoch. The accuracy of the predicted position is also high dependent on the age of the TLE set. NORAD typically updates the TLE sets based on an as-needed basis rather than according to pre-determined schedule. Some of the determining factors in the update frequency of the TLE sets are: the orbital parameters (specially the orbital altitude) and the manoeuvring capabilities of the satellite.

An examination of the TLE sets for the Delfi-n3Xt reveals that on average a new set was made available every 30 hours. The study also showed that the positional error grows at a rate of 1 to 2 km per day [3]. This means that the Delfi-n3Xt's positional error can be in the order of  $\pm 3$  km right before the TLE sets are updated. Figure 7 shows the Doppler shift error as a result of a 3 km positional error. It can be seen that with the aid of orbital prediction software, the search space can be reduced to a 32 Hz window. This is referred to as aided signal acquisition and can greatly reduce acquisition time.

However, the loop bandwidth that leads to the best BER performance is still too narrow to cover this frequency range. To overcome this challenge, a two step variable loop bandwidth is used. During the acquisition phase, the receiver would use a larger loop bandwidth to allow locking onto the signal from a larger initial offset. Once carrier lock is achieved, the optimum loop bandwidth is used to improve tracking performance and reduce the BER.

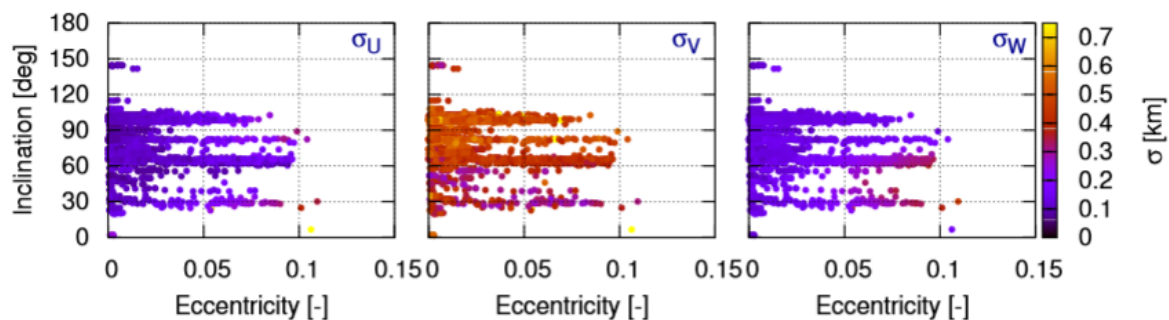


Figure 6: Estimated uncertainties of all objects in LEO in radial (U), along-track (V) and out-of-plane (W) directions [3]

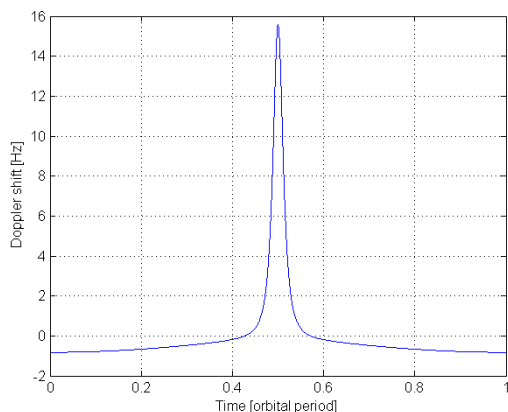


Figure 7: Doppler shift error due to TLE inaccuracies

## Methodology and Analysis

In order to assess the performance of the new demodulator, we developed a MATLAB script to produce an exact replica of the BPSK signal as it would be received on the ground station if it were transmitted by the Delfi-n3Xt satellite. The demodulated signal is compared to the transmitted signal to evaluate the BER. To further validate our results, pre-recorded Delfi-n3Xt signals (at baseband) were processed by the demodulator to analyse its performance under real-world conditions. Since the exact transmitted binary sequence is unknown, for the latter experiment, a packet success rate analysis was performed instead. To determine if received packets contain single or multi bit-errors, the Cyclic

Redundancy Check (CRC) field of the frame is examined. The details of the simulation and experimental set-up as well as the results are described below.

### *BER analysis*

The developed script simulates the effects of AWGN interference on a BPSK modulated signal. What separates our approach with others in the field, is the fact that the effects of Doppler shift are also fully modelled. Figure 8 shows the structure of the simulation. The orbital model determines the carrier frequency as well as the symbol clock of the transmitter. Once the randomly generated binary string is modulated, the simulation adds white noise using a sum block to simulate the AWGN channel. BER is measured after filtering and demodulating the received signal in the receiver. A sampling rate of 44100 Hz is used through out the experiments.

Figure 9a shows the simulation results of BER versus SNR for different data-rates. The results show that at a data-rate of 2400 bps, the BER performance of the new demodulator is only a fraction of a decibel worse than the theoretical limit. For instance at a BER of  $10^{-5}$ , the required SNR is only 0.3 dB above the theoretical value. The BER performance is only marginally affected when increasing the data-rate to 4800 bps.

The BER performance at a data-rate of 9600 bps suffers from a larger gap with respect to the theoretical value. This is attributed to the use of a low sampling rate that approaches the 38400 Hz

Nyquist frequency. The performance of the new demodulator, operating at a data-rate of 9600 bps, is on average 1 dB worse than the predicted value. It is also quite clear that under all conditions, the new demodulator can greatly outperform the old demodulator used for the current Delfi-C3 and Delfi-n3Xt missions.

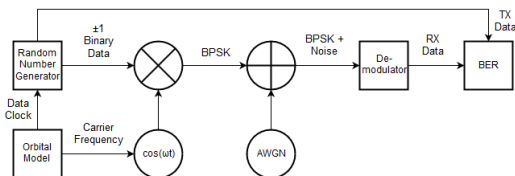


Figure 8: Simulation structure

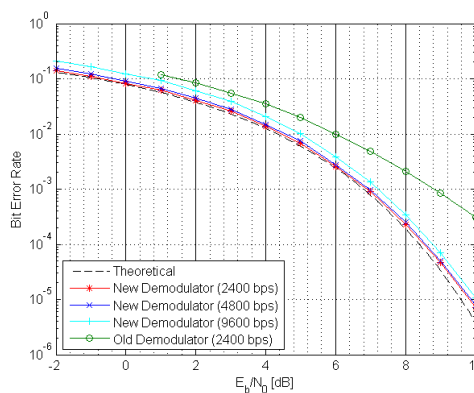
### Packet Success Rate Analysis

To validate the results of the simulation, pre-recorded baseband signal during the Delfi-n3Xt pass on 17-01-2014 was analysed. During this pass the closest approach occurred at an elevation angle of  $84.9^\circ$  and a slant range of 738 km. The measured SNR during this pass is shown in Figure 10. The shaded areas indicate time periods where packets were successfully received. From this figure, it is evident that whenever the SNR peaked above 10 dB, successful packet reception was nearly guaranteed. In fact, 618 packets were transmitted (1 second packet transmission interval) when the measured SNR was above 10 dB, from which only 16 packets were corrupted as a result of bit-errors. This shows that the packet reception rate of the new demodulator is approximately 97%.

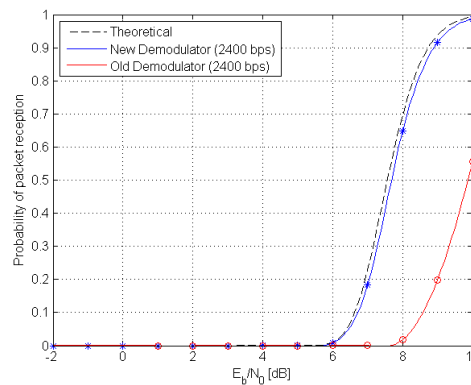
To correlate the packet reception rate to the BER the following equation can be used:

$$P_{\text{Packet Reception Rate}} = (1 - \text{BER})^{\text{PacketLength}} \quad (9)$$

In the case of the Delfi-n3Xt, the packet length is 1792 bits and the resulting packet reception rate is illustrated in Figure 9b. In comparison, the theoretical maximum and the predicted (based on BER analysis) packet reception rates, at a SNR of 10 dB, are 99.2% and 98.6% respectively. The old demodulator demonstrated a similar packet reception rate at a SNR of 15 dB. We have thus reduced the required SNR for a (nearly) uninterrupted transmission link, by approximately 5 dB.



(a) bit error rate



(b) packet reception rate

Figure 9: BER and packet reception rate versus SNR

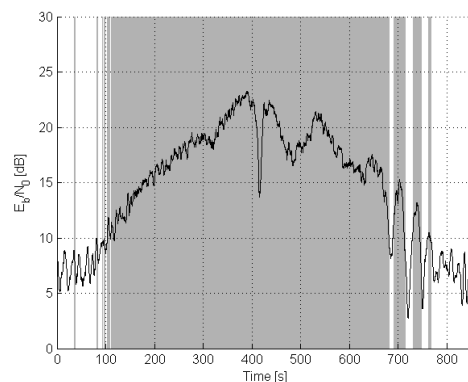


Figure 10: Measured SNR during the Delfi-n3Xt pass on 17-01-2014

## Conclusions

In this paper, we presented an architectural overview and analysis of a high performance DSP-based BPSK demodulator. We gave particular attention to lowering the BER when operating near the Nyquist rate. The minimum achievable BER was determined to be within 1 dB from the theoretical limit across all examined data-rates. Finally, we showed that under real-world conditions, the link margin for successful packet transmission was improved by upto 5 dB. When used for the current missions, the new demodulator can more than double the amount of collected telemetry data. However, when distributed to the participating radio amateurs, the improved packet reception rate will result in a much larger increase in the number of collected packets.

## References

- [1] S. Archa and S. Dhanya. Software defined radio. *International Journal of Science and Research*, 5(1):1152–1155, 2016.
- [2] J. P. Costas. Synchronous communications. *Proceedings of the IRE*, 44(12):1713–1718, 1956.
- [3] T. Flohrer. Assessment and Categorization of TLE Orbit Errors for the US SSN Catalogue. *Aboa Space Research Oy (ASRO) at Space Debris Office*, 2008.
- [4] F. M. Gardner. A BPSK/QPSK timing-error detector for sampled receivers. *IEEE Transactions on Communications*, 34(5):423–429, 1986.
- [5] J. C. Kim. On the improvement of low elevation angle satellite communications impaired by tropospheric fading effects. pages 603–607, 1999.
- [6] J. Mevada, J. Samuel, S. Bhadane, A. K. Gulati, and R. D. Koilpillai. Design and implementation of a robust downlink communication system for nanosatellites.
- [7] T. Ulversoy. Software defined radio: Challenges and opportunities. *IEEE Communications Surveys and Tutorials*, 12(4):531–550, 2010.